



# **UNIVERSITÀ DEGLI STUDI DI TRIESTE**

## **XXIX CICLO DEL DOTTORATO DI RICERCA IN NANOTECNOLOGIE**

### **Development of an integrated nanotechnology-based platform for the early diagnosis of cancer: assessment of circulating biomarkers in Her2-positive breast cancer and role of novel binders in biomarkers detection**

Settore scientifico-disciplinare: FIS/03

**DOTTORANDO / A**  
**Elena Ambrosetti**



**COORDINATORE**  
**Prof. Lucia Pasquato**

**SUPERVISORE DI TESI**  
**Dr. Loredana Casalis**

**ANNO ACCADEMICO 2015 / 2016**

## TABLE OF CONTENTS

✚ Abstract.....	5
✚ Introduction.....	7
1. Breast cancer.....	7
1.1 Classification of breast cancer subtypes .....	7
1.2 Breast cancer screening: drawbacks of standard molecular tests and the increasing importance of “liquid biopsy” .....	10
1.3 Breast cancer circulating biomarkers: “new generation” biomarkers.....	10
2. Human Epidermal Growth Factor Receptor 2 (Her2).....	12
2.1 Biological role and signal transduction pathways.....	12
2.2 Structure and mechanism of activation.....	13
2.3 Extracellular domain (ECD)-Her2: role and prognostic significance.....	15
2.4 Her2-targeted therapy in clinic.....	16
2.5 Her2 detection in breast tumor: state of the art and pitfalls.....	17
2.6 Challenges in clinical utility of ECD-Her2: correlation of tumor tissue Her2 status and serum ECD-Her2 .....	18
2.7 Membrane lipid microdomains: a crucial role in the regulation of Her2 activation and Her2-containing exosomes release .....	20
3. Nanotechnology in cancer medicine.....	22
3.1 Nanotechnology-based diagnostics: state of the art.....	22
3.2 Emerging surface and interface protein analysis techniques.....	23
3.3 Atomic Force Microscopy (AFM): a nanotechnology tool for surface- based biomolecular recognition.....	25
3.3.1 AFM mode of operation.....	27
3.3.2 Self-Assembled Monolayers (SAMs) .....	28
3.3.3 AFM nanolithography: nanografting.....	31
3.3.4 DNA-Directed Immobilization (DDI): a powerful strategy to develop nano-immuno protein assays.....	33
3.3.5 Nanoscale protein arrays: conventional and novel binders.....	35
4. The potential of nanoscale tools in a multi-integrated approach for cancer assessment.....	39

 <b>Results</b> .....	41
5. Nanoarrays development and optimization.....	41
5.1 Mouse antibody-functionalized nanoarrays.....	41
5.1.1 Ab-DNA conjugates production and characterization.....	41
5.1.2 ECD-Her2 detection: calibration curve and sensitivity.....	44
5.1.3 Comparison with Trastuzumab-functionalized nanoarray detection.....	49
5.2 Camelid nanobody-funtionalized nanoarrays.....	50
5.2.1 VHH-DNA conjugates production and characterization...	50
5.2.2 ECD-Her2 detection: calibration curve and sensitivity.....	51
5.3 Regeneration of the nanoarray.....	54
5.4 ECD-Her2 detection in standardized human serum.....	55
5.5 Multiplexed detection.....	57
5.6 Fluorescence experiments.....	59
5.6.1 Validation of Nanoarray topographic measurements .....	59
5.6.2 “Epitope mapping” studies.....	60
6. Aptamers: a preliminary study to assess its feasibility as innovative nanoarray binders.....	63
6.1 Preliminary affinity characterization of the DNA-aptamer construct.....	64
6.2 AFM mechanical sensing on nanostructured assays.....	66
7. Study of the potential value of released ECD-Her2 as indicator of tumor progression.....	68
7.1 Localization and quantification of Her2 on cell membranes.....	69
7.2 Co-localization of intracellular domain (ICD)-Her2 and ADAM10 on SKBR3 cell membranes.....	71
7.3 Correlation between ECD-Her2 levels in cell medium and Her2 tumor status.....	72
8. Study of Her2 status in exosome-driven tumor cell communication.....	73
8.1 Co-localization of Her2 and rafts components in cell membranes.....	74
8.2 Exosomes spreading by Her2-positive cells: a multi-integrated approach for the characterization and for the correlation of Her2 status in cell membranes and released ECD-Her2 levels.....	76
  <b>Discussion</b> .....	 80

✚ <b>Materials and Methods</b> .....	84
✚ <b>Appendix: other AFM-based nanoarrays applications</b> .....	94
✚ <b>Bibliography</b> .....	105



## ABSTRACT

Early detection of cancer plays a crucial role in determining disease prognosis. The major challenge consists in the ability of identifying the disease through the quantification of a set of specific biomarkers in tissues and/or, more interestingly, released in the bloodstream. Non-invasiveness, sensitivity, parallelization, low cost, are some of the most relevant keywords in this field. Hence the development of miniaturized devices for the early detection of cancer is at the core of nanodiagnostics, requiring the recognition and quantification of low amounts of specific disease biomarkers, through the development of sensitive diagnostic tools. In this context, we have developed a nanodiagnostic platform for the non-invasive quantification of cancer biomarkers circulating in the bloodstream. The assay, that relies on Atomic Force Microscopy (AFM), is based on molecular manipulation to create density-optimized functional spots of surface-immobilized binders and differential AFM topography. It is label-free, allows the parallel detection of different cancer biomarkers, entails a single binder per antigen and when implemented with fluorescence labelling/readout can be used for epitope mapping. The possibility to exploit DNA nanografting and subsequent immobilization of binders through DNA-directed immobilization confers robustness to the assay. We explored the feasibility of novel binders as camelid nanobodies and aptamers, to improve the quality of the functionalization, and therefore device sensitivity, with the added advantage of binders easy engineering. In this study we focused on a prospective, clinically-relevant circulating cancer biomarker, the extra-cellular domain (ECD) of Human Epidermal Growth Factor Receptor (Her2), whose shedding and release in the blood is related to the progression of Her2-positive tumors and response to anticancer therapies. By employing robust, easily engineered camelid nanobodies as binders, we measured ECD-Her2 concentrations in the range of the actual clinical cutoff value for Her2-positive breast cancer. The specificity for Her2 detection was preserved when measured in complex matrices as standardized human serum, and in parallel with other potential biomarkers, demonstrating the intended implementation of multiplexing analysis, strongly required to define the biological tumor subtype and to univocally refer specific molecular levels to tumor status and progression.

A better understanding of the Her2 receptor biology, overexpression in tumor cell membranes and release of the ECD to the bloodstream is however required to interpret the measured levels of ECD-Her2 at best. At present, there are controversial studies and conflicting results about the correlation between the protein levels in serum and the attested Her2 status in tumor tissue, which make the clinical significance of circulating ECD-Her2 still

uncertain. Therefore we developed a multi-integrated approach in order to elucidate Her2 overexpression, dimerization and ECD shedding mechanism and to fully validate its prognostic value; moreover we preliminarily studied some fundamental aspects of the relationship between rafts-mediated exosomes formation and Her2 integration on them in order to clarify its possible role in metastasis occurrence. This approach relies on different multi-scale techniques and enables to correlate information coming from advanced optical microscopies (membrane proteins localization), nanotechnology-based diagnostic tools (detection of protein and vesicle biomarkers) and novel super resolution fluorescence microscopies (quantification and co-localization of different biomarkers). This innovative platform will be instrumental in identifying and quantifying clinically useful biomarkers and to translate basic science results into the clinics to impact cancer diagnosis, prognosis, and therapy.

# INTRODUCTION

## 1. BREAST CANCER

Breast cancer is the most common cancer in women worldwide, accounting for nearly one in three cancers diagnosed among women in the United States, and the second leading cause of cancer death around the world [1,2].

It is the most frequently diagnosed tumor type in 140 out of 184 countries worldwide [2].

Breast cancer is not a single disease but it is an ensemble of many biologically different diseases that are characterized by different genetic variations, gene expression profiles pathological features and clinical implications [3,4].

Despite advances in cancer treatment, many patients still fail therapy, mainly because of intrinsic inter-tumoral and intra-tumoral heterogeneity, facing disease progression, recurrence, and reduced overall survival [5].

### 1.1 CLASSIFICATION OF BREAST CANCER SUBTYPES

Breast cancer refers to several types of neoplasm arising from breast tissue, the most common being adenocarcinoma of the cells lining the terminal duct lobular unit. The cancer cells are similar in phenotype to the normal basal or luminal cells, the two distinct types of epithelial cell found in the ductal structure [6] (Fig. 1).

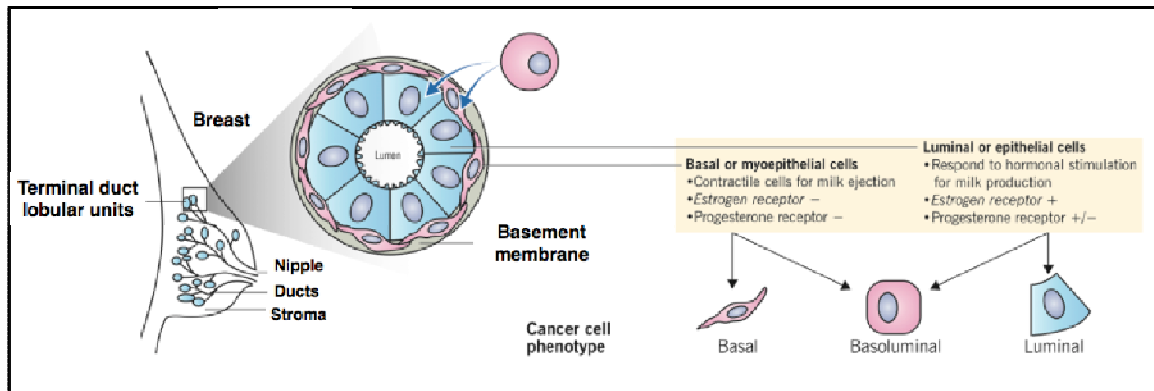


**Fig. 1** Breast cancer pathogenesis and cross-section view of mammary terminal duct lobular unit; breast cancer pathogenesis and histologic subtypes. *Adapted from McMaster Pathophysiology Review - <http://www.pathophys.org/breast-cancer/>*

Due to the intrinsic heterogeneity of breast cancer a classification system has been developed; this classification has been improved and modified over many decades, following the progresses obtained in cancer research [7]. The traditional histological and anatomic-pathological evaluation has been superseded by the precise molecular characterization carried

out by gene profile analysis [7,8]. This approach allows a new paradigm of breast cancer patients stratification which provides an increased accuracy of disease prognosis and therapeutic strategy [8].

The pioneer studies conducted by Sørlie *et al.* identified five intrinsic, distinct subtypes: luminal A, luminal B, Her2-enriched, basal and normal-like breast tumors [9].

Except for normal-like tumors which are characterized by a normal breast tissue profiling [10], each of the five subtypes is accurately described by a molecular profile, immunoistochemical and clinic-pathological features; the main criteria of the characterization is the presence/overexpression of specific protein receptors. A portrait of these four subfamilies is summarized in Fig. 2.

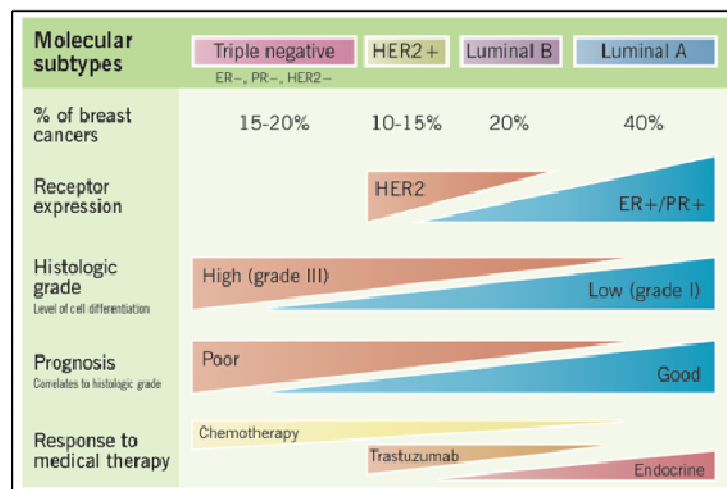


**Fig. 2** Breast cancer molecular subtypes. *Adapted from McMaster Pathophysiology Review - <http://www.pathophys.org/breast-cancer/>*

### Luminal cancer

Luminal tumors are the most common subtypes among breast cancer, with luminal A being the majority (50% of breast cancer patients). The luminal-like tumors express the hormone receptors Estrogen Receptor (ER) and/or Progesterone Receptor (PR) [10]. It is possible to distinguish two subtypes of luminal-like tumors, luminal A and luminal B. They represent the ER+, PR+, Her2- (ER or PR positivity and Her2 negativity) and ER+, PR+, Her2+ (ER or PR positivity and Her2 positivity) subtype, respectively [10]. **Luminal A** tumors have higher expression of ER-related genes and lower expression of proliferative genes than luminal B cancers [9]. **Luminal B** tumors tend to be of higher grade than luminal A tumors. The luminal subtypes carry a good prognosis, and luminal B tumors have a significantly worse prognosis than the luminal A subtype. Luminal tumors respond well to hormone therapy but poorly to conventional chemotherapy, although luminal B tumors which are more

proliferative may benefit more from a combined chemotherapy and hormonal treatment strategy [8].

### **Her2-enriched cancer**

The Her2 overexpression tumors, which represents at least 15-20% of all breast cancers, exhibit abnormal high quantities of **Human Epidermal Growth Factor Receptor 2 (Her2)**: a Her2-positive cancer cell has approximately 2 million Her2 proteins on its surface, around 100 times more than a normal cell [11]. Her2-positive tumor tends to be more aggressive, to spread more quickly and to have worse survival outcome than other types of breast cancers [8,9]. Their poor prognosis derives from a higher risk of early relapse and metastasis occurrence and relative resistance to hormonal agents [8]. The use of molecularly targeted agents such as the monoclonal antibodies **Trastuzumab** and **Pertuzumab** is at present the preferential strategy for Her2-positive cancer treatment.

### **Basal-like cancer**

The basal subtype represents 10-20% of all breast carcinomas and is also named “**triple negative**” due to the expression profile ER-, PR-, Her2- [8], lacking or low expression of hormone receptors and Her2, and high expression of basal markers (cytokeratins CK5/6, CK14, and CK17) [10,12]. These tumors are of particular aggressiveness and currently lack any form of standard targeted systemic therapy, leaving chemotherapy be the only clinical approach. They are associated with a lower disease-specific survival and a higher risk of local and regional relapse [8]. Metaplastic breast cancer is a type of triple negative breast cancer that grows and spreads more quickly: it describes a cancer that begins in one type of cell, such as glandular epithelial cells, and changes into another type of cell, such as nonglandular cells [13]. □ Triple negative breast cancer often associated to the presence of mutations in two genes called BRCA1 and BRCA2. The genes code for a DNA repair pathway that is important for protecting against mutations. The loss of either gene confers a high risk of breast cancer, as well as other cancers. Hence this kind of breast cancer is hereditary, meaning that there is a known genetic mutation causing increased cancer risk in the patient’s family [14].

The “ER- and PR-” signature of Her2-positive and triple negative subtypes make the diagnosis and prognosis of such kinds of tumor critical. Since at present immunohistochemistry (ICH) is the key methodology to define them, standard techniques

employed in pathology laboratories are essential for identifying these subtypes to avoid false positive and negative results and hence to improve the efficacy of diagnosis.

## **1.2 BREAST CANCER SCREENING: DRAWBACKS OF STANDARD MOLECULAR TESTS AND THE INCREASING IMPORTANCE OF “LIQUID BIOPSY”**

The landscape of breast cancer diagnosis and treatment is commonly investigated by means of molecular techniques used in current clinical practice. Immunohistochemistry is the primary routine detection tool: by means of stained monoclonal or polyclonal Abs it allows to detect specific receptor overexpression in tissue sections [15,16]. In combination with this standard technique there are other two US Food and Drug Administration (FDA)–approved assays used for the molecular profile of breast cancer, **in situ hybridization (ISH)** and **fluorescence in situ hybridization (FISH)** that are capable to detect gene amplification of the target. Furthermore, the **Next Generation Sequencing (NGS)** approach recently allowed to obtain “gene panel testing”, covering a large number of screened genes on a single platform [15,16].

All these diagnostic tests, from the simple IHC to the more complex FISH and NSG, have different levels of experimental procedure complexity and cost, but the common requirement of a tissue sample as starting test material, obtained through surgical tissue biopsy. This aspect is becoming a huge limitation in terms of efficacy of clinical outcome: tumor tissue is not always available for molecular analysis, since some human body regions involved in the metastatic disease could have a poor accessibility and due to the fact that the surgical tissue resection of multi-metastasis could be strongly invasive. Moreover intra-tumor heterogeneity and the capability of cancer genome to evolve with time, particularly as resistance develops in response to treatment [17], make the tissue biopsy an unsuitable tool for a relevant and significant molecular profiling. Thus, to fully enable personalized medicine it is important to have an easily accessible, minimally invasive procedure to recognize and follow the molecular markers of a patient’s tumor. One viable route is the **liquid biopsy**, by which the genetic/proteic portrait of the tumor can be assessed through specific biomarkers released in biofluid samples. Liquid biopsies have the potential to monitor early primary or recurrent disease and to evaluate the response to treatment and to estimate risk and mortality [17,18].

## **1.3 BREAST CANCER CIRCULATING BIOMARKERS: “NEW GENERATION” BIOMARKERS**

Both healthy and diseased cells transmit information on their state to the bloodstream, either through the release of biomolecules or as cell signalling intermediates (microvesicles, metabolites). In principle, all of them can be exploited as suitable “new generation” biomarkers for the liquid biopsy. The most common are:

- **circulating cell-free DNA (cfDNA)**. Elevated levels of cfDNA, derived partially from reduced DNase activity, are seen in breast cancer, but sometimes also in some benign breast disease; therefore, levels of cfDNA are not tumor-specific markers. However, it is possible to distinguish between patients with breast cancer and healthy female controls by comparing cfDNA profiles and studying specific patterns of cfDNA modification (i.e. mutations, loss of heterozygosity (LOH) and hypermethylation) [17,19];
- **circulating microRNAs (miRNA)**. miRNAs, as regulators of gene expression can modulate the expression of the protein-coding genes and hence they are involved in the regulation of many cellular functions in several diseases. miRNA profiles can classify human cancers, including breast cancers and potentially determine the tissue of origin for cancers of unknown primary origin [17];
- **circulating tumor cells (CTCs)**. Tumor cells capable to disseminate from the primary tumor to distant organs through the peripheral bloodstream are named CTCs. Many studies have shown that CTCs are of prognostic significance in various metastatic carcinomas including breast cancer and are associated with decreased progression-free survival. CTCs are also potential source of both cfDNA and miRNA [17,20];
- **exosomes**. They are small extracellular vesicles (EVs) ensuring transport of molecules between cells and throughout the body. EVs contain specific signatures (RNA, DNA and protein) and, functioning as inter-cellular messengers, have been shown to strongly impact on the fate of recipient cells [21,22]. Exosomes have been proposed to play an important pro-tumorigenic role, stimulating tumor cells growth, suppressing the immune response and even being part of the cancer progression and the metastatic process. It has been shown that breast cancer cells secrete exosomes with specific protein signatures, as crucial factor for metastasis occurrence [23]. In particular, among the different subtypes of breast cancer, Her2-enriched tumor spreading seems to be highly regulated by huge secretion of Her2-containing exosomes [24].

Moreover, together with all the mentioned above innovative biomarkers, Her2-positive breast cancer exhibits another category of biomolecule that is released into the bloodstream: the protein **extracellular domain (ECD)** of the transmembrane receptor Her2. Therefore, although the precise correlation between Her2 tissue status and ECD-Her2 serum level is still

debated and deeply investigated, Her2 testing in liquid biopsy is becoming complementary in a more and more relevant way to IHC/FISH tests, aiding in identifying Her2-positive patients [25].

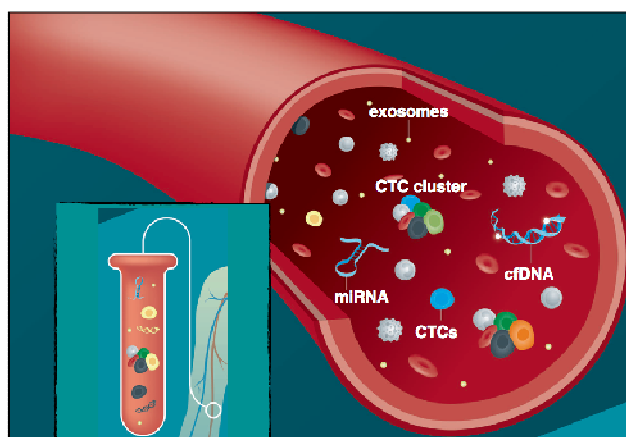


**Fig. 3** Blood circulating cancer biomarkers. *Adapted from "Liquid biopsy in the clinic"*  
<http://www.nature.com/nrclinonc/posters/liquidbiopsies/index.html>

## 2. HUMAN EPIDERMAL GROWTH FACTOR RECEPTOR 2 (Her2)

The human Her2/*neu* proto-gene, mapped to chromosome 17q21, encodes for a Her2 receptor that has a structure consistent with a growth factor receptor. Her2 is a 1255 amino acid, 185 kDa transmembrane glycoprotein receptor that belongs to the Her family, which also includes Her1, Her3 and Her4. It plays a key role in the Her family, cooperating with other Her receptors through a complex signaling network [26,27,28].

Normal tissues have a low amount of Her2 membrane protein. Her2 gene amplification causes the overexpression of the receptor and the alteration of its normal control of cell mechanisms, leading to malignancy and tumor occurrence [27,28]. Her2 overexpression/amplification has been observed in 20% to 30% of breast cancer and it is associated with a worse biological behavior and poor prognosis [28], reduced overall survival and time to relapse [29].

Breast cancers can exhibit up to 25–50 copies of the Her2 gene, and up to 40–100 fold increase in Her2 protein resulting in 2 million receptors expressed at the tumor cell surface [29]. This status is maintained during progression to invasive disease and to metastasis onset.

### 2.1 BIOLOGICAL ROLE AND SIGNAL TRANSDUCTION PATHWAYS

Her2 plays an important role in human development (nervous system, developing bone,



muscle, skin, heart, lungs and intestinal epithelium). It is involved in many biological processes related to normal breast growth and development, such as myelination, regulation of cell adhesion, signal transduction, regulation of transcription, differentiation and survival [27].

Her2 has the strongest catalytic kinase activity among family members; as other tyrosine kinase receptors, Her2 proteins undergo dimerization and transphosphorylation of their intracellular domains and then activate multiple downstream pro-proliferation signalling pathways. Considering the Her2 multiple interactions with the different members of the receptor family, Her2 signalling is a very complex network with a variety of pathways. The two main transduction routes are the mitogenic Ras/Raf/ Mitogen-activated protein kinase (MAPK) cascade that promotes positive regulation of cell growth and proliferation, and the pro-survival Phosphoinositide 3-kinase (PI3K)/Akt cascade that inhibit apoptosis processes.

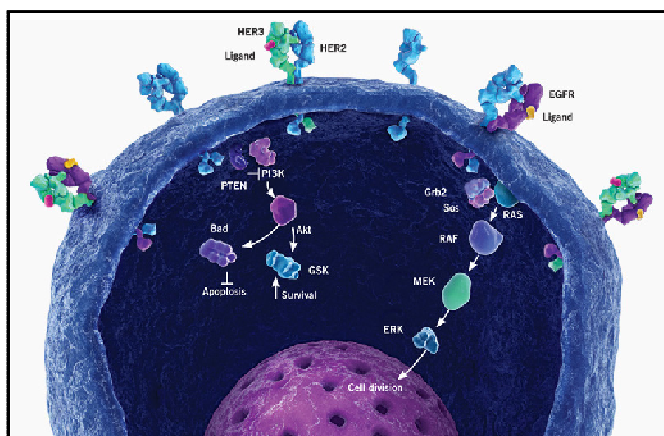


**Fig. 4** The Her2 pathway promotes cell growth and division when it is functioning normally: the binding of EGF to Her is required to activate the MAP Kinase pathway as well as the PI3 Kinase/AKT pathway, which in turn activates the NF- $\kappa$ B pathway. Signaling compounds called mitogens (specifically EGF in this case) arrive at the cell membrane, and bind to the extracellular domain of the Her family of receptors. Those bound proteins then dimerize, activating the receptor. Her2 sends a signal from its intracellular domain, activating several different biochemical pathways. These include the PI3K/Akt pathway and the MAPK pathway. Signals on these pathways promote cell proliferation and the growth of blood vessels to nourish the tumor (angiogenesis).

## 2.2 STRUCTURE AND MECHANISM OF ACTIVATION

As the other members of the family, Her2 is composed by three main regions: the extracellular domain, with two leucine-rich domains responsible for ligand binding, and two cysteine-rich domains with disulfide bond connectivities, responsible for receptor dimerization; the lipophilic transmembrane segment; the amino- and carboxyl-terminal lobes of the kinase domain and the carboxyl-terminal tail [27,30].

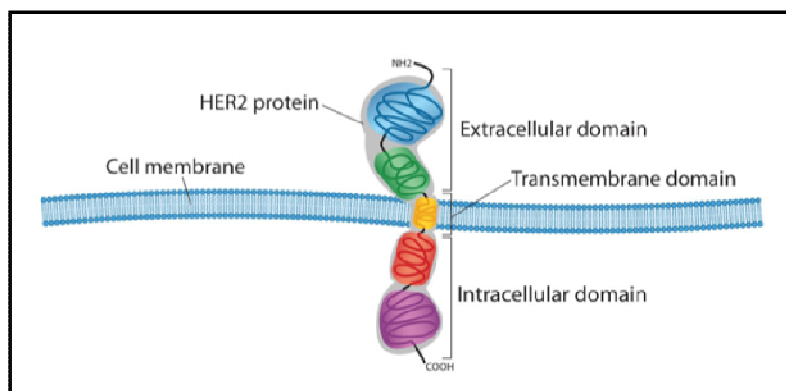


**Fig. 5** Structure of the Her2 receptor

The Her receptors exist as monomers on the cell surface and after ligands binding to their extracellular domains, they undergo **dimerization** and **transphosphorylation** of their intracellular domains, initiating a variety of signaling pathways. Unlike other Her receptors, Her2 has no known direct activating ligand; it may constitutively be in an activated state or can heterodimerize with other family members such as Her1 and Her3 [29]. Due to a strong interaction between the two leucine-rich domains, Her2 always adopts a conformation which is similar to that of ligand-bound receptors, in which the dimerization arms remain constitutively extended and free to homo- or heterodimerize [30]. Her2 heterodimers are more potent than the corresponding homodimers, due to a particularly high-affinity and slow-rate dissociation ligand binding: overexpression of Her2 promotes an abundant heterodimerization, enhancing the preferential binding of ligands to Her2 low-affinity arm. This process is crucial in the oncogenic model [27]. The most active signaling complex is formed between the kinase-deficient receptor Her3 and the ligand-less receptor Her2.

Due to the fact that Her2-Her3 combination is the most potent stimulator of downstream pathways and has the greatest mitogenic potential, it's considered the most relevant Her heterodimers in tumor growth [29]: the unregulated co-expression of these two receptors in cells significantly increases their transforming activity promoting human cancer occurrence.

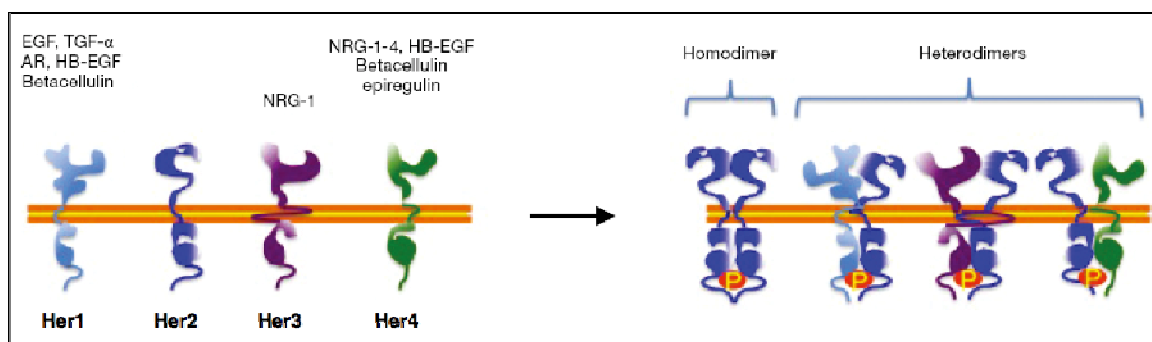


**Fig. 6** The Her receptors can form homodimers or heterodimers according to ligand availability. (A) EGF, TGF-, HB-EGF, amphiregulin (AR) and betacellulin bind to the

EGFR leading to its homodimerization. In presence of Her2, EGF drives the formation of EGFR/Her2 dimer, betacellulin and HB-EGF bind to Her4 leading the formation of homodimers. In presence of Her2, betacellulin triggers the activation of Her2/Her4 heterodimers. The four NRG ligands (NRG1-4) bind to Her3 and to Her4. NRG4 and HB-EGF bind to Her4 dimers only. NRG1-3, betacellulin and, to a lesser extent, epiregulin drive the heterodimerization of Her2 with Her3 and Her4. *Adapted from doi: 10.3978/j.issn.2224-4778.2015.06.01*

### **2.3 EXTRACELLULAR DOMAIN (ECD)-Her2: ROLE AND PROGNOSTIC SIGNIFICANCE**

The Her2 dimer formation determines the proteolytic cleavage (shedding) of its extracellular domain (ECD), a soluble fragment of approximately 105–110 kDa, which can diffuse through tissue and enter the circulation [30,31,32,33]. The ECD is organized in four regions: two leucine-rich domains (I/L1, III/L2), responsible for ligand binding, and two cysteine-rich domains (II/CR1, IV/CR2) connected by disulfide bonds and involved in receptor dimerization [30].

The Her2 cleavage position has been located in the juxtamembrane region: the primary cleavage site has been located at amino acid position 647–648 and a minor cleavage site has been located at amino acid position 644–645 [33]. **Her2 shedding** has been associated with cleavage by matrix metalloproteinases (MMPs) and in particularly **ADAM** disintegrins. Proteolytic release of ECD-Her2 results in two effects: it acts as ligand, modifying the activity of other unrelated receptors; most importantly, creates a constitutively active N-terminally truncated receptor (p95Her2) which increases Her2 tyrosine kinase activity, delivering growth and survival signals to cancer cells and rising the oncogenic potential [30].

Many studies have measured the concentration level of serum ECD-Her2 in breast cancer patients, finding an increased level of the shedded portion of the receptor that is also correlated with the presence of Her2 overexpression in tumor tissue [34]. Elevated amount of ECD-Her2 has been detected in 30% to 70% of patients with metastatic breast cancer (MBC); moreover rising serum Her2 concentrations have been associated with progressive metastatic disease and a poor response to chemotherapy [35].

The most used **cutoff value of circulating ECD-Her2** is the one established from the Immune One – Bayer ELISA kit (as better explained in the paragraph 2.5) and corresponds to 15 ng/mL. According to this test, healthy individuals typically exhibit ECD-Her2 levels of 2 to 15 ng/ml while breast cancer patients levels as high as 15 to 75 ng/ml [34,36]. Therefore these studies demonstrated that the released ECD-Her2 might be used as a useful biomarker

and that diagnostic tools measuring ECD-Her2 levels in serum may provide useful information for monitoring early disease relapse, cancer progression or response to therapy [37].

## 2.4 Her2-TARGETED THERAPY IN CLINIC

Since Her2 is often amplified/overexpressed in cancer cells, it has been regarded as a tumor-specific target in molecular therapies. The main therapeutic approaches to target Her2-positive cancer rely on two different strategies: inhibition of Her2 dimerization and inhibition of Her2 protein tyrosine kinase activity.

The first approach is based on the use of **Humanized Monoclonal Antibodies** (MAbs) directed against the extracellular domain of Her2 that, once bound, block the dimerization of the receptor and hence the downstream signaling pathways. Nowadays two Mabs have been approved by FDA for their clinical use in Her2-positive cancer treatment:

- Trastuzumab (Herceptin), that binds to domain IV of the extracellular segment of the Her2 receptor. Although the mechanisms by which it exerts its antitumor effect are not yet completely understood, the most likely hypothesis is that, after binding the ECD, it blocks not only the dimerization but also the ECD cleavage and so prevents the production of an active truncated Her2 fragment that is associated to a more aggressive behavior in breast cancer [38]. Some evidences demonstrated that Trastuzumab seems to have its greatest effects in tumors with increased number of Her2 homodimers [39] and that elevated ECD-Her2 has a biological relevance in the susceptibility to Trastuzumab-based therapy. On the other hand patients treated with Trastuzumab show a decrease in concentrations of serum ECD-Her2 [48] and individuals who did not achieve a significant decline (>20%) in serum Her2 levels have decreased benefit from Trastuzumab-based therapy [40].

The approval of this agent was based on evidence of a significant prolongation in disease-free survival in women receiving Trastuzumab and chemotherapy compared to those receiving chemotherapy alone [29].

- Pertuzumab, that binds Her2 near the junction of domain I, II and III and blocks the activation of the Her2 receptor by hindering dimerization and association with its partner receptors. Pertuzumab elicits action at a different ligand binding site from Trastuzumab; Pertuzumab binding mediates the same antibody-dependent cytotoxic effects as Trastuzumab binding, although it does not block Her2 shedding as Trastuzumab does [41].

Also Pertuzumab has completed clinical trials in combination with Trastuzumab and chemotherapy on metastatic breast cancer [29].

The second approach is based on the use of **small molecule drugs** that inhibit the tyrosine kinase activity of the intracellular domain of Her2 (ICD-Her2) interrupting signaling molecular cascades. Lapatinib is the most used inhibitor in patients whose tumors are Trastuzumab-resistant; when combined with some chemotherapy drugs in patients with metastatic disease, it increases the patient benefit [29].

## **2.5 Her2 DETECTION IN BREAST TUMOR: STATE OF ART AND PITFALLS**

An accurate determination of Her2 status is of crucial importance in disease diagnosis, guiding therapy and increasing drug responses.

The FDA has approved some of Her2 diagnostic tests. Currently, the most commonly used Her2 diagnostic tests include both tissue-based methods (IHC and ISH) and serum-based methods (ELISA) [35,36].

At present, the tissue-based Her2 tests are the most frequently used initial tests to detect the Her2 status: according to the most recent guidelines published by the American Society of Clinical Oncology only patients with a uniform intense membrane staining of more than 30% of invasive tumor cells on IHC, and a Her2/*neu*-to-chromosome 17 centromere (CEP17) ratio of greater than 2.2 on FISH are considered Her2-positive and are eligible for Trastuzumab treatment [42]. ICH and FISH are highly accurate but, as discussed before, suffer from the limitations of the impracticality and invasive nature of continuously taking biopsies for disease-monitoring purposes.

Moreover variation in the procedures adopted by different labs to assess in the distribution of Her2 in tumor tissues determines inconsistent reporting of IHC or FISH; in many cases there is also a significant discordance between the IHC and the FISH results. The inherent heterogeneity complicates the scenario: tumor cells are prone to switch their clinical Her2 status as a result of growing of subclones overlooked in primary tumors under selective pressure. This could determine discordance in a meta-analysis addressing Her2 status assessed by IHC and FISH on tumor tissues from primary tumors and corresponding relapse.

In the recent years all these concerns about whether IHC and FISH suffice for Her2 testing raise the interest towards the serum Her2 immunoassay (ELISA) as potential dynamic, real-time and non-invasive test to measure soluble Her2 quantitatively and to supplement existing Her2 testing [34,35]. It is important to underline that currently the serum Her2 assay is not used for screening purposes and is not a substitute for tissue testing, but is intended for the follow-up and monitoring of patients with metastatic breast cancer whose initial serum Her2 value is above 15 ng/ml [43].

Although the great potentiality and utility the serum immunoassay has some issues mainly related to the experimental procedure: serum interference might cause unexpected elevated levels of protein and hence a false positive result. Due to the kinetic nature of serum ECD-Her2 levels, it is highly possible that a patient could have both abnormal and normal serum ECD-Her2 levels depending on the time of serum collection.

The antibodies used in the immunoassay are another important aspect to be evaluated for the significance of the test: some antibodies show incompatibility if the serum samples are from patients who are treated with Trastuzumab, due to their competitive binding with the target [40]. In addition false results can be caused by the heterophilic human anti-animal immunoglobulin antibodies (HAIA), especially the human anti-mouse antibodies (HAMA), that bind to animal antibodies by cross reactivity [44,45]. These antibodies are easily acquired through blood transfusions, vaccinations, treatment with mouse monoclonal antibodies, or from handling animals and are known to bind to mouse antibodies commonly used in serum cancer biomarker tests, including serum ECD-Her2 [34], reducing the significance of the measurement and pushing for enhanced selectivity in serum immune-test.

But the crucial point that has to be investigated to definitely endorse the clinical relevance of ECD-Her2 and hence to validate circulating ECD-Her2 serum assays is the correlation between the protein level in serum and the attested Her2 status in tumor tissue.

## **2.6 CHALLENGES IN CLINICAL UTILITY OF ECD-Her2: CORRELATION OF TUMOR TISSUE Her2 STATUS AND SERUM ECD-Her2**

Many recent *in vitro* studies have evaluated the correlation between abnormal ECD-Her2 in serum and Her2 positivity in tissue, generating conflicting results [30,46]: some have shown that the protein level (detected with quantitative immunofluorescence in patients tissue microarrays) is high even in the absence of gene amplification; on the contrary some others have demonstrated that when Her2 gene amplification occurs, the high protein expression level might decrease the cells ability to cleave or process the Her2 protein, decreasing the amount of released ECD-Her2 [46]; other studies have shown that Her2-negative primary tumors may have Her2-positive paired distant metastases or that Her2 overexpression may be lost during metastatic progression.

The discrepancy between serum ECD-Her2 levels and tissue status might become an obstacle for the clinical utility of the baseline ECD-Her2. Possible explanations accounting for this discrepancy are discussed below.

Alternative splice variants of Her2 exist, including the two soluble forms of Her2, also known

as p100 and Herstatin. p100 is composed of the first 633 amino acids and contains the ECD subdomains I–IV then Herstatin includes the first 340 amino acids of Her2 with two ECD subdomains (I and II) and ends with a unique carboxyl tail sequence by which it binds to ECD-Her2 subdomain II similarly to Pertuzumab, interfering with Her2 dimerization. The products of this alternative splicing can escape into the circulation because they are soluble [30]. Whereas the full length p185 Her2 is associated with pro-oncogenic receptor activity, the two soluble forms of Her2 (p100 and Herstatin) may have an anti-oncogenic function by inhibiting receptor dimerization and tumor cell proliferation. The current FDA-approved serum Her2 immunoassay seems to not distinguish between these different variants possibly altering the correlation between serum ECD-Her2 and tissue Her2 [33]. In this direction the discovery of binders that recognize “neoepitope” on ECD-Her2 could help to discriminate these variants [33].

The high concordance in Her2 status and serum ECD level may be affected also by the lack of ECD-Her2 expression, as one of the mechanisms of resistance to Trastuzumab therapy [46,47].

In addition some studies reported discordant ICD-high/ECD-low expression that can be explained considering the well known mechanisms of ECD cleavage or the expression of a truncated Her2 protein that lacks the ECD. However these findings suggest that the ability to predict Her2 gene amplification is strongly affected by the different protein domain specificity exhibited by IHC antibodies [46]. At present, it remains unclear whether patients with elevated serum ECD also express correspondingly high levels of cell membrane-bound activated ICD-Her2 in either Her2-overexpressing primary breast cancer or MBC patients [48].

In general, few studies attempt to compare tissue and serum data, and to precisely correlate dimerization with ECD shedding at different level of tumor progression and in response to therapy. Knowing whether the level of shedded ECD-Her2 helps predicting tissue Her2 status, would validate ECD-Her2 screening in the serum as complement determination of tissue testing and would help to define Her2 status with greater accuracy, both in early breast cancer and in metastatic disease.

## 2.7 MEMBRANE LIPID MICRODOMAINS: A CRUCIAL ROLE IN THE REGULATION OF Her2 ACTIVATION AND Her2-CONTAINING EXOSOMES RELEASE

With the proof of dynamic protein distribution in the cell membrane, the **fluid mosaic model** was introduced and has become the most accepted model until now. The fluid mosaic model highlights that: i) both lipids and proteins are dynamic and diffuse randomly in the homogeneous lipid bilayer and ii) proteins are asymmetrically distributed in the cell membrane. In recent years however many experimental findings went in conflict with this classical model and indicated that cell membranes also contain various nano/micro-sized domains. In particular **lipid rafts** are membrane domains enriched in sphingolipids (i.e. ganglioside GM), cholesterol and GPI-anchored proteins. They are small, heterogeneous, highly dynamic and play an important role in membrane trafficking and signal transduction. In particular these microdomains cluster together with proteins involved in the regulation of crucial cellular processes, many of which are altered in pathological disease, as cancer [49,50,51].

Quantitative fluorescence microscopy studies have demonstrated that clusters of Her2 colocalize with lipid rafts on Her2 overexpressing breast cancer cells [52,53]. Both gangliosides GM1 and GM3 are thought to modulate Her2 dimerization activity by retaining Her2 within the lipid raft, thereby modulating the local density of Her proteins and increasing the probability of dimerization and activation [54]. It has been observed that Her2 dimerization in breast cancer cells takes place in a particular sub-family of rafts, called **caveolae**, that are non-clathrin invaginations of the plasma membrane enriched in the family of integral membrane proteins known as **caveolins** [49,53].

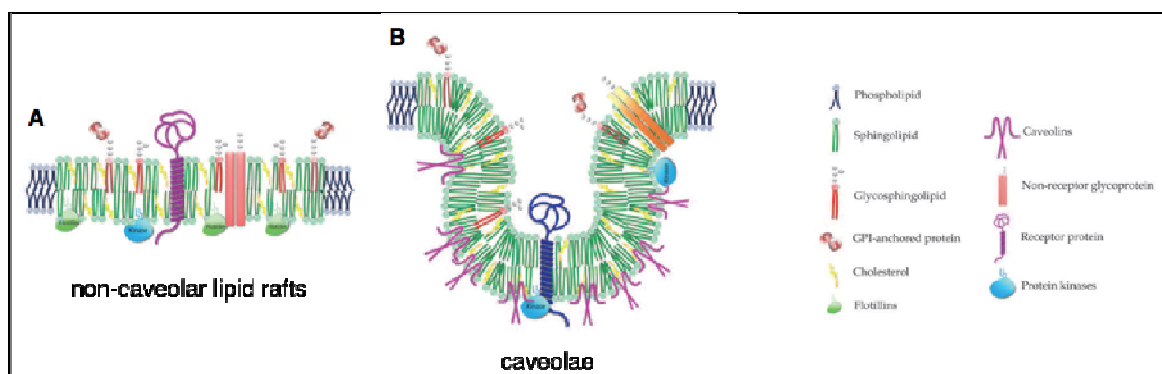


**Fig. 7** Lipid and protein components of (A) non-caveolar lipid rafts and (B) caveolae. *Adapted from doi: 10.5772/21324*



From different studies, it has then been proposed that lipid rafts influence the association properties and the biological function of Her2 and that the dissociation of the rafts decreased Her2 dimerization. [49,52]. The presence of rafts and the membrane rigidity could be also responsible of the lateral mobility of the ADAM metalloproteases and their protein substrate, affecting the shedding process and the serum ECD-Her2 release [30]. Moreover, recent studies demonstrated how the substrate selectivity of ADAMs and consequently their shedding activity is strictly connected to their localization into distinct lipid rafts. For this reason, high levels of endogenous fatty acids should promote kinetically favorable interactions between Her2 and ADAM proteases in lipid rafts microdomains, enhancing Her2 shedding [30].

The evidence that lipid rafts play a fundamental role in providing a microenvironment favoring Her2 dimerization which in turn drives tumor transformation and progression opens the possibility to target lipid rafts for cancer treatments and hence interfering with Her2-driven proliferation of breast cancer cells [52].

The preferential Her2 localization and functional interaction in caveolae open another interesting scenario; caveolae are known to regulate important processes such as signal transduction within the cell, vesicular transport, cell migration and cell cycle, since they are the preferential regions for the inward budding of the plasma required for vesicles-mediated transport machinery. By means of caveolae-driven vesicles formation, signalling molecules could be compartmentalized and properly released from cells and spread in distant tissue. This mechanism has important implications in numerous human pathological conditions, such as tumorigenesis and metastatic spread. Recent experimental evidences [55] grew the interest on the understanding the precise role of caveolae in cancer regulation. The main protein component of caveolae is Caveolin-1 (Cav1), an integral membrane 21–22 kDa scaffolding protein that coats 50–100 nm plasma membrane invaginations. It has been observed that Cav1 is commonly up-regulated in several advanced epithelial tumors including breast carcinomas.

Some studies demonstrated that even if an initial loss of Cav-1 is observed in breast cancer, re-expression of Cav-1 at later stages might correlate with more malignant characteristics [55]. Moreover high expression of Cav1 positively correlates with increased invasion and migration, and this seems to be strictly related to the overexpression of Cav1 in secreted tumor exosomes [56,57]. For this reason a prominent role in Her2-enhanced cancer progression and spreading seems to be attributed to **Her2-positive exosomes**. Additionally, Her2-positive exosomes have been shown to confer the phenotypic traits of their originating

cells to recipient cells [58] and are enriched in proteins involved in metabolic pathways related to cancer progression [59].

However further investigations are still necessary to understand the role of Cav1 in exosome biology and in particular the relationship between rafts-mediated nano-vesicles formation and transport (transcytosis, endocytosis) and Her2 integration on them. Highlighting the molecular mechanisms through which Her2 receptor is segregated and processed in the exosomes would be instrumental to understand the significance of Her2-exosome recognition for a complete and comprehensive Her2-status evaluation.

### **3. NANOTECHNOLOGY IN CANCER MEDICINE**

#### **3.1 NANOTECHNOLOGY-BASED DIAGNOSTICS: STATE OF THE ART**

The last decade has witnessed how nanotechnology, or the engineering and controlling matter at the molecular scale, has been able to create structures/devices with novel chemical, physical and biological properties. Nanomedicine in particular bears the potential to radically change the way to make diagnosis and treat diseases. **Cancer nanotechnology** is a novel interdisciplinary area of comprehensive research that combines the basic sciences, which includes biology, physics and chemistry, with engineering and medicine, with a broad spectrum of applications in cancer treatment, spanning from therapeutics, diagnostics and prognostics [60]. Noteworthy recent improvements in cancer research have expanded our understanding of cancer as a disease at the genetic, molecular, and cellular levels, opening venues for research for the development of newer approaches and technologies.

The power of nanotechnology in cancer treatment is expected to be manifold: concerning the diagnostic field, nanotechnology is expected to encompass current limitations as insufficient sensitivity and specificity in detecting tumor conditions or early-stage cancer, inability to determine tumor stage, to perform predictive and accurate screening with low cost procedures [61]; concerning therapy, nanotechnologies are expected to develop new approaches to increase the specificity of anticancer drugs, the delivery of suitable drug concentrations to the target site, reducing toxicity effects, increase the ability to track and control site-specific therapeutic responses and adverse effects, and mitigate development of drug resistance [62].

Among new nanotechnology methods in anti-cancer therapies, nanoparticles constitute at present the most promising and investigated tool. These particles, that range between 1 and 100 nm in size, are developed as potential delivery systems for cancer therapies: with their unique structure and dimension they exhibit enhanced permeability and retention effect;

moreover they preferentially accumulate in tumors, resulting in higher drug concentrations at targeted sites. Therefore they provide an opportunity to change the pharmacokinetic outline of drugs, lowering toxicity for surrounding normal tissue, and enhance the therapeutic markers. Today, nanoparticle-based drug delivery platforms are made mainly by liposomes, polymeric nanoparticles and metal nanoparticles, depending on the material in which the payload is encapsulated [63,64].

On the diagnostics side, keywords are high sensitivity, non-invasivity and fast detection of disease-related biomolecules [1,25,27]. In this assorted framework, nanotechnologies provide evidence to bring major breakthroughs in terms of **integration and miniaturization** of the various bioassays [25]. Notable examples are miniaturized electrochemical and surface plasmon resonance (SPR)-based sensors, functional nanoparticles and protein/DNA nanoarrays which can offer enhanced precision and significantly faster measurements than what achievable with highly spread, FDA-approved technologies [38,39,41,47]. Miniaturized, integrated and multiplexing strategies are particularly urging when moving into the direction of non-invasive “liquid biopsy”, i.e. the detection of reliable biomarkers (proteins, nucleic acids, circulating cells) directly in the bloodstream of patients to monitor early-stage tumor occurrence as well as its evolution during systemic treatments.

In spite of the readout technique (optical, mechanical and electrical) employed, all micro- and nano-biosensing systems rely on biological molecular recognition that ensures the high affinity capture of the target biomarker [65].

### **3.2 EMERGING SURFACE AND INTERFACE PROTEIN ANALYSIS TECHNIQUES**

Surface and interface protein analysis techniques are widely explored in the field of molecular biorecognition. The immobilization of the receptor on a solid support allows for the easy spatial separation of bound from unbound molecules, overcoming the difficulty to discriminate between them in solution and possibly the need of molecule labeling. Another advantage of surface immobilization, compared to solution, is the possibility to tune the parameters of the immobilization process, and to control the localization and the stability of the molecules.

One of the most exploited miniaturized device for protein detection is the microarray. A **protein microarray** is a solid surface on which different proteins (i.e. antigens, antibodies, enzymes, substrates) are immobilized in discrete spatial locations, forming a high density protein dot matrix [66,67].

Protein microarrays can be classified into three types: analytical, functional and reverse phase protein arrays. Analytical protein microarrays are usually composed of biomolecules with specific binding activities, such as antibodies, to determine whether a sample contains a specific protein of interest or to analyze the components of complex biological samples. They have been used for protein expression profiling, biomarker identification, determination of cell surface marker, glycosylation profiles and clinical diagnosis [67]. On the other hand, functional protein microarrays are constructed by printing a large number of individually purified proteins, and are mainly used to comprehensively query biochemistry properties and to study protein–protein, protein–DNA, protein–RNA, protein– phospholipid and protein–small molecule interactions [66,67]. Reverse-phase microarrays (RPPA) is a method that allows for the analysis of many samples obtained at different states by directly spotting cell lysate, specifically identifying certain proteins by means of many different probes [68]. The potency of this methodology relies on the multiplexing capability, that allow to detect simultaneously a great number of different antigens. However the immobilization on the surface of the proteins as recognition elements is a crucial step, due in particular to the damage and/or denaturation that may occur during the immobilization.

Another, and probably most used, label-based solid-phase approach is the **Enzyme-Linked ImmunoSorbent Assay** (ELISA). This test is usually performed in a sandwich configuration: protein binder molecules, generally antibodies, are immobilized on a surface. The bound protein is detected through a second, enzyme-linked antibody. After the addition of the enzyme's substrate, a reaction gives colorimetric signal used to quantify the analyte. Compared to other immunoassay methods, ELISA tests are considered highly sensitive and strongly specific. On the other side this assay has several disadvantages: large sample volumes are required (low-volume assay formats often requires automated and expensive equipment), cross-reactivity might occur with the secondary antibody, resulting in nonspecific signal, and, mainly, readout based on labeled- or colorimetric-molecules often determine false positive/negative results.

Moreover, one of the main drawbacks of label-dependent detection is that manipulating structure of a probe or a specific antibody can affect their binding capability. Therefore, label-free detection methods have also been investigated for protein microarrays. **Mass spectrometry** has been used for detecting ligands bound to individual proteins printed on protein microarrays, with approaches as MALDI (matrix-assisted laser desorption ionization)-MS (mass spectrometry), SELDI (Surface-enhanced laser desorption/ionization)-TOF (time of flight)-MS, and MALDI-TOF-MS used for this purpose. Another powerful label-free

technology is **Surface Plasmon resonance** (SPR): it allows to analyze biomolecular interactions in real-time, and has been adapted to protein microarray signal detection. It is based on the principle that incident light can resonate with free electrons oscillations on a metal surface in total internal reflection, and that the resonance signals will change when ligands bind to (and/or dissociate from) ligands on the array surface. Binding event can thus be monitored and the kinetic parameters calculated in real-time. [66].

One advantage of this technique is that is label-free; on the contrary probe immobilization may cause the heterogeneity of surface binding.

**Atomic Force Microscopy** (AFM) offers the possibility to control density and orientation of protein layers on gold surfaces for optimal biorecognition through nanolithography techniques, and simultaneously the measurement of binding interactions in a label-free way.

### **3.3 ATOMIC FORCE MICROSCOPY (AFM): A NANOTECHNOLOGY TOOL FOR SURFACE-BASED BIOMOLECULAR RECOGNITION**

Scanning Probe Microscopy (SPM) is a family of powerful techniques that allow to investigate the local properties of a solid surface with high spatial resolution, reaching the nanometric and subnanometric scale. Two are the main types of SPM microscopes: Scanning Tunneling Microscopes (STMs) and Atomic Force Microscopes (AFMs) [69]. In both cases a nano-sized scanning probe is brought in close proximity of a surface (nanometers or fractions), till a specific probe-surface interaction is measured. Also, the probe is mounted on a piezoelectric motor, which allows a scanning over a plane parallel to the surface, measuring point by point the interaction with the surface. An electronic feedback system keeps the tip-sample distance or interaction constant during scanning. In the case of STM, the first SPM to be developed, the probe is a sharp metallic tip, and the measured interaction is the tunneling current flowing between the tip and the substrate, which then has to be conductive or semi-conductive; there is an exponential connection between the tip to sample distance and the current flow, that confers the unique atomic resolution [69]. An STM map of a surface is reflecting the distribution of the electronic states on the surface, and therefore the position of individual atoms. Unfortunately, few biological surfaces are conductive enough to be measured by STM. To overcome this limit, AFM has been introduced. In this case, interaction forces between the tip and the sample surface are measured: at atomic distances, van der Waals forces are in fact always in place, regardless of the conductive nature of the materials [70]. To measure such forces AFM employs special nanometer probes formed by an elastic cantilever with a sharp tip (radius of curvature between 1 and 10 nm) at the end (Fig. 8). The force applied to

the tip by the surface (or viceversa), results in a measurable bending of the cantilever [70,71]. Another advantage of AFM over STM for studying biological samples is the measuring environment: STM requires ultra-high vacuum or dry air conditions; AFM is usually operated in air or in liquid, including physiological conditions.

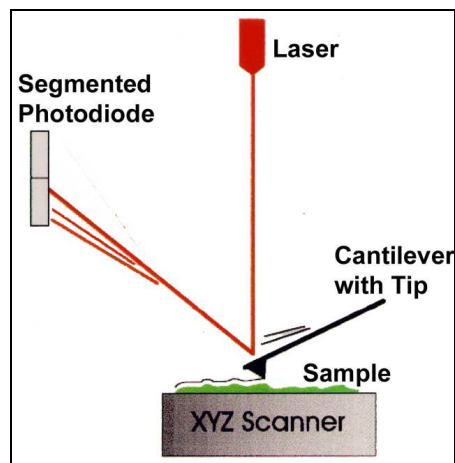


**Fig. 8** Schematic representation of an Atomic force Microscope. A laser beam is focused on top of the free end of a cantilever and reflected on a four elements detector, sensitive to the laser shifts during the scanning of the sample.

The tip is typically made of silicon–oxide and has a radius of curvature of 10 nm for standard probes. The soft micro-sized cantilever has a spring constant that may vary according to the sample and the application (from few tens of pN/nm to few tens of nN/nm) that is function of the elastic constant of the material and of cantilever dimension. Measuring the cantilever deflection, it is possible to evaluate the tip–surface interaction force [70,71].

Cantilever deflection is measured by a laser beam focused on the top of the free end of the cantilever and reflected on a four-elements position-sensitive photodiode. Knowing the stiffness of the cantilever, in first approximation, the Hooke's law gives the linearly relationship between the force required to deflect the cantilever and its deformation:

$$F = -kz$$

where  $F$  is the force,  $k$  is the stiffness of the cantilever, and  $z$  is the amount the lever is bent.

A piezoelectric actuator moves accurately the AFM probe and the sample in the X-Y plane in a raster manner. The number of lines scanned in a surface unit contributes to the resolution of the image. A Z-actuator, composed by piezoelectric material as well, controls the vertical movement of the tip [70,71]. In the case of AFM, a typical surface map is the constant force contour of the surface, which in turn reflects the chemical/morphological properties of it.

### 3.3.1 AFM modes of operation

The main interaction forces measured by AFM are the van der Waals forces: the interaction potential between two atoms, on the tip and on the sample, respectively, located at a distance  $r$  from each other, can be approximated by the Lennard-Jones potential function (Fig. 9).

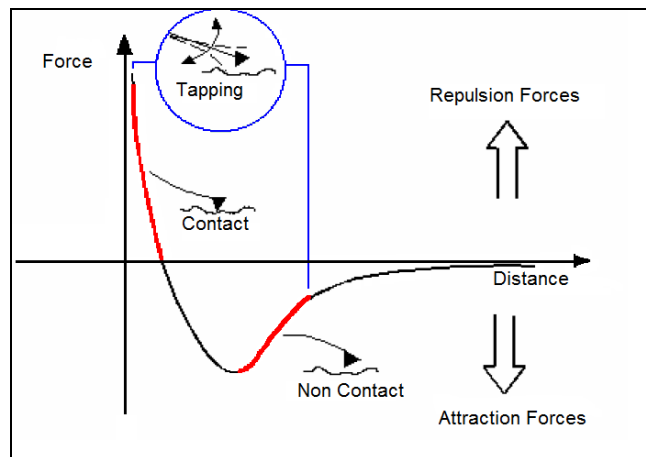


**Fig. 9** AFM force-distance curve. From this curve, it is possible to understand the role of the different interactions depending on the distance between the tip and the sample. The tip, approaching the surface, starts to feel attractive long range forces (non-contact AFM region) until tip and surface electron orbitals are so close to start exerting repulsive forces (contact mode AFM region). Between these two regimes lies the intermittent-contact (or tapping mode) region.

The AFM surface imaging capability can be explored in different modalities: depending on the tip-sample distance AFM operates in repulsive or attractive regime. When the tip starts approaching the surface, long-range, attractive van der Waals interaction predominates (depending on the nature of tip and sample, also electrostatic and/or magnetic forces can be present); when the tip is near (some Angstroms) to the surface, short-range repulsive forces dominate. When repulsive forces predominate (steeper part of the potential), AFM operates in static mode (or **contact mode**), in which the probe is maintained in constant gentle contact with the sample (low load); differently when attractive forces predominates AFM is operated in dynamic mode (**non-contact and intermittent mode**) with an oscillating probe [71,72].

The **contact mode AFM (CM-AFM)**, as already said, is usually considered the static operation mode. As the name suggests, the tip is in constant, gentle contact with the surface of the sample. From the measure of the cantilever deflection, it is possible to calculate the force of interaction between the probe and the surface. In this mode, the

deflection of the cantilever is used as input to a feedback circuit that moves the scanner up and down in z, responding to the topography by keeping the cantilever deflection constant. With the cantilever deflection held constant, the total force applied to the sample is constant. In this mode, the topographic image is generated from the scanner's z-motion recorded in each point of the sample. The scanning speed is thus limited by the response time of the feedback circuit [71,72].

In **Non Contact-AFM (NC-AFM)** the tip is positioned at a certain constant distance from the surface (within few nanometres) where attractive forces (electrostatic, magnetic, attractive van der Waals forces) predominate. Then the tip is made scanning at a given amplitude and frequency (generally closed to the cantilever resonance frequency). Variations in the resonance frequency, amplitude and phase of the oscillation are linked to the characteristics of the surface and to the tip-sample interactions. All these parameters are monitored in order to reconstruct the topography of the sample [71,72].

In the case of **Intermittent Contact Mode (or Tapping Mode)**, the amplitude of the oscillation, influenced by long-range forces, controls the feedback system and the error signal (difference between the setpoint and the amplitude) is the input for the feedback system. The output, as in CM-AFM, controls the Z-actuator and the tip movement. Moreover, during the scanning it is possible to record the variation of the oscillation phase. This signal is particularly useful in the case of a heterogeneous material because gives information about the chemical properties of the sample. Since the tip touches intermittently the surface, the damage of the sample is significantly reduced. Despite the difficulties of operating in tapping mode in liquid environment due to the significant dumping of oscillation frequencies by the viscosity of the aqueous medium, this operational mode is widely applied in biological field for the study of living cells, lipid membranes and DNA molecules [71,72].

Besides the topography information of the sample another important parameter determined by the AFM imaging is the roughness. It is calculated as the root mean square average of height deviation taken from the mean image data plane and indicates the homogeneity of the sample.

### **3.3.2 Self-Assembled Monolayers (SAMs)**

Self-assembly, in a general sense, might be defined as the spontaneous formation of complex hierarchical structures from pre-designed building blocks, typically involving multiple energy scales and multiple degrees of freedom. The molecular self-assembly



often proceeds through several consecutive stages and thermodynamically toward the state of lower entropy [73].

Self-Assembled Monolayers (SAMs) are organic assemblies formed by the adsorption of molecular constituents from solution onto the surface of solids. One of the most widely studied SAM is alkanethiols on gold. Gold is chosen as metal solid surface because of its many advantages: it is easy to obtain and is a reasonably inert metal exceptionally easy to pattern by a combination of lithographic tools; moreover gold binds thiols with a high affinity (30 kcal/mol) and stability and it does not undergo any unusual reactions with them. Alkanethiols ( $\text{CH}_3(\text{CH}_2)_{n-1}\text{SH}$ , or  $\text{C}_n$ ) are powerful molecules for this application: the thiol head group acts as an anchor group, quasi-covalently bound to the gold, while the carbon chain is referred as the 'backbone' which stabilizes the SAM due to van der Waals interactions between adjacent chains. The end group in the simplest case consists of a methyl-group. However, a lot of other functionalized end groups have been so far synthesized, with the added value of tuning the chemical properties of the SAM film for further applications [73].

The most common protocol for preparing a well-ordered SAM of alkanethiols on gold is by immersion of a freshly prepared or clean substrate into a dilute ethanolic solution of thiols for 12-18 h at room temperature. Dense coverage of adsorbates are obtained quickly from millimolar solutions (milliseconds to minutes), but a slow reorganization process requires times on the order of hours to maximize the density of molecules and minimize the defects in the SAM. Indeed self-assembly is characterized by two distinct phases: a first one in which molecules initially attach to gold with the chains parallel to the surface. This ordered phase is called lying-down phase or stripe phase, with the chain parallel to the surface. In this phase, alkanethiol molecules bind to the Au substrate through the S head by losing the mercaptan H atom (two alkanethiol molecules need to react simultaneously with the Au surface, in order to release their H in the  $\text{H}_2$  form), turning in alkanethiolates (Fig. 10).

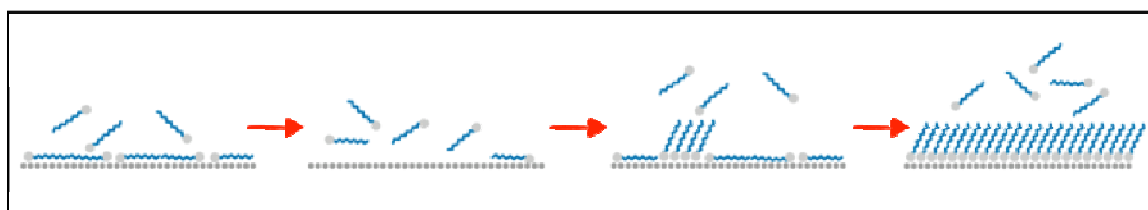


**Fig. 10** Schematic representation of the different phases of spontaneous unconstrained self-assembly. *Adapted from doi: 10.1146/annurev.physchem.58.032806.104542*

As the reaction proceeds, the increase in surface coverage results in the nucleation of

ordered domains of stand-up thiols, which eventually form a complete layer, as result of collision and lateral pressure. The molecules stand with their longitudinal axis tilted of 30° with respect to the surface, forming a compact layer well oriented with respect to the Au (111) surface, as the result of lateral van der Waals interactions between the chains and the S-Au chemical interaction [73,74].

SAMs of alkanethiols are very much employed in micro and nanotechnology, to produce patterns of different chemical properties on a surface. The simplest strategy consists in the physical transfer of the molecular components of a SAM to the substrate in an imposed pattern. For that two main strategies have been employed: **Microcontact Printing** ( $\mu$ CP) and the scanning probe lithography [75]. In the  $\mu$ CP an elastomer, casted and cured from a master structure generated by “soft-lithography” methods, is inked by immersion with a molecular precursor of a self-assembled monolayer, and printed to a substrates (with planar or even non-planar topographies) to transfer molecules through the contact points and generate a SAM into the substrate, with the only requirement to hold some affinity for binding the head groups [76] (Fig. 11).

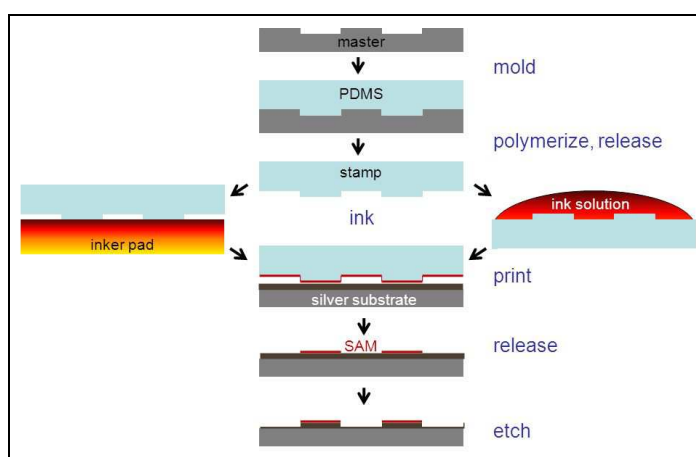


**Fig. 11** Schematic representation of the basic steps of microcontact printing is shown in figure 1 at the right. A PDMS stamp is created curing the elastomer onto a surface which has the features one wants to reproduce. After curing, the stamp is peeled off the master, and can then be "inked" with the molecules to be stamped. Stamping is achieved by simple placing the inked stamp on a surface. The ink molecules transfer to the surface with the pattern of the stamp. *Adapted from doi: 10.1021/ja980770z*

Another method employed to generate SAM patterns on a surface is the **Dip-pen nano-lithography**: it consists on a tip of an AFM “inked” into a solution of alkanethiol, and then used to scan, for instance, a gold surface. During scanning in air, a water meniscus forms, through which the molecules are released to the surface. This technique can write

lines of molecules as small as the tip dimension (few nm), and can be thermally activated [75].

Also DNA can self-assemble on gold surfaces, when is modified at one end with an alkanethiol (typically C<sub>6</sub>). DNA SAMs on gold have been intensively studied and exploited for DNA-based microarray applications.

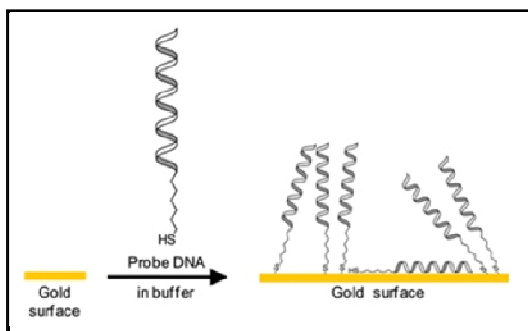


**Fig. 12** Cartoon of DNA-SAM on gold surface. DNA is a thiol-modified DNA and it adsorbs on the surface via specific and nonspecific bonds. The former are S-Au bonds at higher energy than the latter N-Au bonds (that means a link between nitrogenous bases and gold surface).

The main difference between DNA and alkanethiols is that DNA is negatively charged. So, in order to screen the negative charge of DNA backbones, extra charges are needed: a saline solution (buffer) is added as a consequence. In fact positive ions of saline solution shield the DNA chains electrostatic repulsion and allow the SAM to form. Furthermore, the dimension of DNA strand with respect of alkanethiol introduces steric effects which define the structure of the monolayer: DNA SAM would not have the same packed structure on gold and it would be more disorganized [77,78].

SAM density on the substrate increased with the increasing of the incubation time and of the concentration of DNA molecules in solution. Moreover the greater is the roughness of the substrate higher is the density of the SAM because it increases the number of active sites for anchoring the DNA. It has also been demonstrated that lower ionic strength solutions (measured as the electric field intensity generated by the ions in that solution) correspond to less probe adsorption (due to the electrostatic repulsion between DNA strands that are less screened) and, simultaneously, higher ionic strength solutions are associated to higher probe coverage [79].

### 3.3.3 AFM nanolithography: nanografting

**Nanografting** is a lithographic AFM mediated technique, developed by Liu *et al* in 1997 [74]. This method employs an AFM tip to locally exchange the molecules that belong to a pre-existing SAM layer in a selected area with other thiolated molecules present in solution, obtaining confined nanostructures of the grafted molecules surrounded by a SAM carpet of other molecules. The experimental procedure starts with the growth on an ultra-flat gold surface of a SAM of alkanethiols, typically oligo-ethylene glycole terminated.

This layer will be used as reference carpet for topographic measurement of the surface and, due to its biorepellent properties, will prevent the non-specific adsorption of molecules on the surface [80]. Scanning of the tip at high force (around 100 nN) determines the local displacement of the reference molecules and the replacement by thiolated molecules of interest dissolved at high concentration in the liquid medium, forming the so called Nanografting Assembled Monolayers (NAMs).

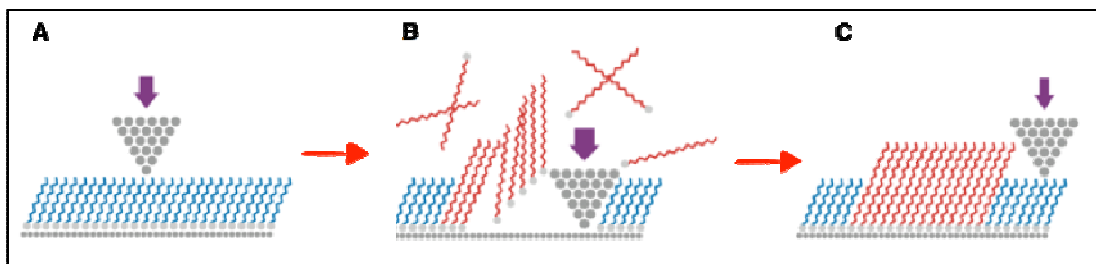


**Fig. 13** Schematic representation of nanografting procedure. The scanning of AFM tip at high force displaces the molecules of a reference SAM of thiols promoting the replacement with the thiolated molecules of interest dissolved in solution. *Adapted from doi: 10.1146/annurev.physchem.58.032806.104542*

There are many advantages that make nanografting a powerful tool in surface functionalization: it allows controlling the molecular packing of the nanostructure both in terms of conformation and molecular density. Moreover, the spatial confinement during the NAM formation (which is an exchange process, see Fig. 13B) enables directly the standing up configuration on the gold surface made free by the AFM tip. Finally, under identical reaction conditions, self-assembly occurs much faster in NAMs than in unconstrained SAM. In this way, it is possible to create nanostructures of large molecules and even biological molecules, as metal nanoparticles, DNA, ligands and proteins, in a well-oriented manner, with high control and precision.

To compare DNA-nanopatches of different sizes and to learn about the density of DNA as a function of the number of times any given area is nanografted over, it has been introduced the line density parameter “ $S/A$ ” where  $S$  is the scanned area and  $A$  is the actual area of the final patch.  $S/A = R \cdot N/L$  in which  $R$  is the width of the tip at the point of contact with the surface, and  $N/L$  is the number of scan lines (in the slow scan direction) divided by the length of the patch  $L$  (in the same direction) [81]. It has been demonstrated that with increased  $S/A$  numbers the height of the nanopatch increases, to indicate that more DNA molecules are grafted into the same area (Fig. 14).

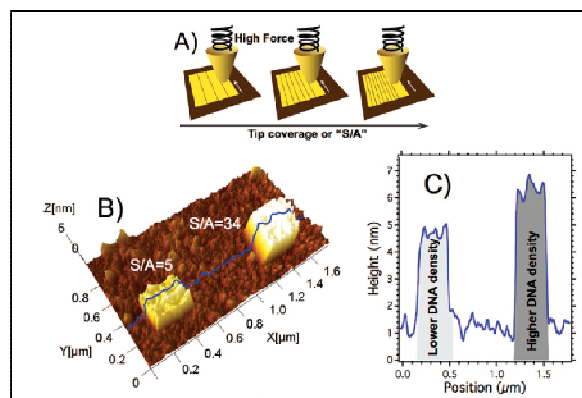


**Fig. 14** (A) Schematic representation of the definition of the nanografted line density  $S/A$  parameter. (B) AFM topographic image of two single-stranded DNA (ssDNA) nanopatches obtained with  $S/A = 5$  (left) and  $S/A = 34$  (right). (C) A profile of the NAM in B (blue line).  
 From doi:10.1021/nl802722k

Moreover the  $S/A$  density parameter affects the hybridization with the complementary sequence. In the low  $S/A$  regime, after hybridization, the height of the DNA-nanopatches increases significantly, due to the much higher stiffness of double-stranded DNA (dsDNA) with respect to ssDNA. Instead in the high  $S/A$  regime, in which the height of the nanopatches has already reached saturation, minimal change in height can be detected; compressibility measurements proved that hybridization also occurs in the high  $S/A$  regime, even with low efficiency due to steric hindrance reasons [81].

### 3.3.4 DNA-Directed Immobilization (DDI): a powerful strategy to develop nano-immuno protein assays

Surface-bound DNA molecules have generated huge interest because of their potential applications in biosensing and biorecognition, resulting in the rapid development DNA microarray-based techniques [82,83]. Controlled nanoscale DNA patterning has been exploited to increase the sensitivity of DNA/RNA detection, and is at the core of next generation sequencing, gene expression profiling, comparative genomic hybridization, oligonucleotides mismatches detection, alternative splicing identification or microRNA (miRNA) detection [82,84].

Moreover, in the post-genome era, technology has been driven to develop multiplexed assays that allow studying large numbers of proteins and protein interactions in complex biological systems. Multiplexed assays are used for example for drug discovery to look at thousands of proteins in a sample [85]. Interestingly, for clinical and diagnostic purposes,

measuring the level of only few proteins along with controls is sufficient to monitor a specific disease. In both cases, however, specificity, sensitivity, reagent costs, and straightforwardness of the experimental procedure are the major criteria for selecting a technology and the relative protocols.

Beside DNA hybridization studies, surface-bound ssDNA can also be exploited as a powerful strategy for reversible site-specific immobilization of biomolecules (such as proteins and antibodies) to build receptor arrays and parallel ligand-binding assays. Exploiting AFM-based nanolithography (nanografting) and the exceptionally high physicochemical stability of DNA oligomers one can create ssDNA nanoarrays on gold surfaces by successive attachment or spatially separated synthetic thiolated oligonucleotides [86,87]. These in turn can be used as a template for the attachment of protein binders chemically “barcoded” with the respective complementary strands [88,89]. One of the major advantages of DNA-driven antigen-binder immobilization with respect to direct immobilization of the binder itself, is in the robustness of DNA: DNA nanoarrays can be stored in inert atmosphere for months, without losing their biorecognition capability, and be transformed at the needed moment into a more delicate nanoarray platform for protein studies.

This strategy for multiplexing probe immobilization is called **DDI (DNA-directed immobilization)**, a technique introduced by Christof Niemeyer in 1994 [86,87]. Different DNA-conjugated antibodies/proteins targeting different antigens are immobilized via Watson-Crick base pairing on surface-tethered complementary DNA sequences. As well as the multiplexed capability another great advantage of DDI is that the proteins preserve their biological activity since they are attached to the surface through the DNA linker rather than being directly fixed to the surface through multiple covalent or non-covalent bounds which may limit their conformational freedom and might affect their functionality [90,91].

To effectively facilitate DNA-directed immobilization, biomolecules of interest need to be coupled with a ssDNA moiety, providing a specific recognition site for complementary nucleic acids, and thus a molecular handle for selective immobilization on DNA nanoarrays [86]. The generation of semisynthetic DNA–protein conjugates allows the unique structure-directing properties of DNA to be combined with an almost unlimited variety of protein functionality. The chemical covalent or non-covalent coupling of DNA oligomers with proteins can be obtained through various methods [90].

### 3.3.5 Nanoscale protein arrays: conventional and novel binders

Protein microarrays are a collection of capture binders fixed on a solid surface for the purpose of detecting antigens. These arrays are developed for the detection of proteins expression from cell lysates in general research and special biomarkers from serum or urine for diagnostic applications, allowing the identification of biomarkers or drug compounds. Arrays are used for protein expression profiling, screening, and to discriminate between normal, diseased or treated samples. More specifically the applications to cancer research include profiling proteins to identify candidate biomarkers, characterizing signaling pathways, and measurement of changes in modification or expression level of cancer-related proteins.

The most common molecules used as capture agent covalently bound to the microarray surface consist in **monoclonal antibodies**, proteins produced by immune system and synthesized in pure form by a single clone population of cells. These antibodies, also generically termed immunoglobulins (Ig), can be made in large quantities and have a specific affinity for certain target molecules called antigens.

Antibodies are large, roughly Y-shaped molecules having a molecular weight of approximately 150 kDa and consisting of paired heavy (H) and light (L) polypeptide chains. The two heavy chains are linked to each other by disulfide bonds and each heavy chain is linked to a light chain by another disulfide bond. Since the two heavy chains and the two light chains are identical, an antibody molecule has two identical antigen-binding sites and thus the ability to bind simultaneously to two identical structures. Each of the four chains has a variable region at its amino terminus, which contributes to the antigen-binding site, and a constant region, which determines the isotype [92].

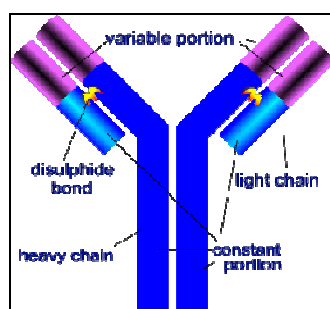


**Fig. 15** Structure of a human antibody: the light and heavy chains are linked together by means of disulfide bound. Both of them exhibit a constant and variable region.

The intrinsic properties that make antibodies (Abs) molecules suitable for recognition in microarrays are the relative high affinity for the specific antigen: the dissociation constant  $K_D$  values span from low micromolar ( $10^{-6}$  M) to nanomolar ( $10^{-7}$  to  $10^{-9}$  M) range. High affinity antibodies show a  $K_D$  in the low nanomolar range - high

picomolar ( $10^{-12}$  M) range. Moreover Abs are very robust molecules that can lead to high reproducibility and throughput in biorecognition performance.

Although conventional monoclonal antibodies are still indispensable reagents in basic research and diagnostics there are some disadvantages that limit their use and their efficiency in microarray applications: elevated costs and long time necessary for their production. Furthermore their dimensions could make Abs inappropriate for some applications. The total number of biological receptor molecules immobilized on a given sensor surface area has in fact an impact on the biosensor sensitivity limit: a higher density of functional recognition molecules will facilitate the sensitive detection of low analyte concentrations. In the case of Abs, surface coverage could be limited by interference between adjacent receptor-analyte complexes. It becomes then clear that small-sized receptor molecules might be an asset to generate the highest possible 'active' probe densities. Therefore, much effort was put by researchers in finding the smallest fragment harbouring the intact antigen-binding capacity of antibodies [93].

In this context, **single-domain camelid immunoglobulins**, termed **VHHs** or **nanobodies (Nb)**, have seen increasing attention in biotechnology, pharmaceutical applications and structure/function research. A single-domain antibody is a peptide chain of about 110 amino acids long, comprising one variable domain (VH) of a heavy-chain antibody, or of a common IgG.

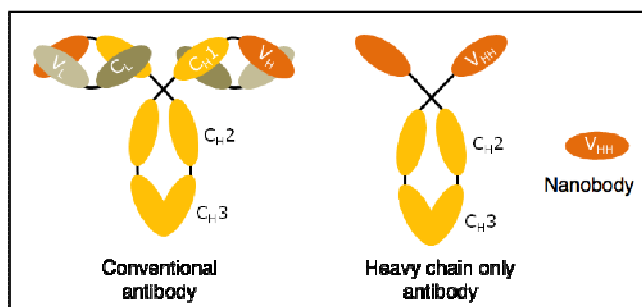


**Fig. 16** Comparison of the structure of conventional antibody with the single-domain antibody VHH.

The great potentiality of nanobodies comes from different unique features that provide access to new epitopes in concave and hinge regions and stabilize them. The original procedure to generate nanobodies comprised as first step the animal immunization; the advent of naïve libraries facilitated and accelerated the whole process [94]. Nowadays nanobody generation is generally initiated through immunization of a llama or a dromedary. Then samples of blood are collected, and lymphocytes are purified. The total RNA from the peripheral blood lymphocytes is extracted and used as a template first for strand cDNA synthesis. Using this cDNA, VHH encoding sequences are amplified by PCR and cloned into the phage-display phagemid vector, leading to a nanobody. Three



consecutive rounds of phage-display and panning (the affinity selection technique which selects for proteins that bind to a given target) are performed on solid-phase coated protein. Each round of panning results in the enrichment for antigen-specific phages within the pools. Tens of individual colonies are randomly selected and analyzed by ELISA for the presence of antigen-specific nanobodies in their periplasmic extracts. Alternatively, immunization can be avoided when using a naïve library. Naïve libraries are generated by collecting the blood of several non-immunized animals. The library is then obtained by the same procedure as described above [94].

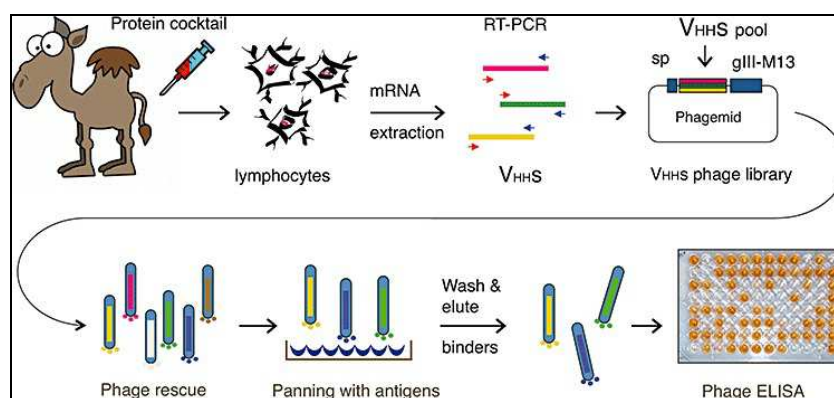


**Fig. 17** Sequential steps of the nanobody generation and selection.

The antigen specificity and affinity of nanobodies from immune libraries are of good quality: equilibrium dissociation constant so that low nanomolar or even picomolar are routinely obtained and can be further improved by molecular evolution after the selection procedure.

With respect to antibodies, nanobodies are more stable, robust under stringent conditions, resistant to chemical and thermal denaturation and can be easily engineered with specific tags and fusion partners to meet diagnostics needs, contributing to the overall reduction of device costs [93,95]. Concerning the development of sensitive and selective biosensors they can be easily modified to avoid chemically reactive groups (primarily amines from lysines) in the vicinity of the paratope and the inclusion of such groups at the opposite end of the domain that permit their directional immobilization on the sensor surface for the maximal capturing capacity of the antigen [96].

Moreover, nanobodies can be selected to avoid cross-reaction with the human anti-mouse antibodies (HAMA), which are present in human serum and could limit the efficacy of antigen quantification. In fact one persistent problem that affects serum biomarker tests is the false results caused by the heterophilic human anti-animal immunoglobulin antibodies (HAIA), including HAMA, that bind by cross reactivity to animal antibodies, such those

commonly used in serum biomarker assays (including Her2 ELISA test), reducing the significance of the measurement [34].

Another valid alternative to antibodies is represented by **nucleic acid aptamers**. Aptamers are oligosequences selected *in vitro* to bind a target with high affinity. In particular they show highly specific binding activity resulting in dissociation constants in the picomolar range, as result of aptamer-target interaction based on three-dimensional folding patterns: depending on their sequence, temperature, pH and the presence of certain ions they fold into defined 3D structures and are able to bind other target molecules with high affinity and specificity [97].

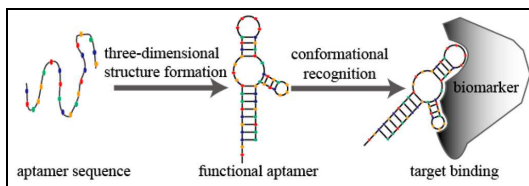


**Fig. 18** Aptamer 3D structure formation promoted for the target binding.

Aptamers are generally selected from a biopanning method known as SELEX (Systematic Evolution of Ligands by Exponential enrichment). The method starts with a random sequence library of ssDNA or ssRNA that spans 20–100 nucleotides in length. Near each random sequence region there is a constant sequences required for capture or priming. The initial diverse pool of aptamers is then exposed to a target molecule, with the expectation that a portion of the aptamers can fold in such a way that they will specifically bind to the target molecule. Non-binding aptamers are then washed away, while candidate aptamers with high target binding affinity are enriched at each selection round by PCR amplification (DNA aptamers) or RT-PCR followed by *in vitro* transcription (RNA aptamers). The enriched pool of aptamers is then exposed to the target again, and the process repeats; finally, they are tested for target binding affinity and specificity [98].

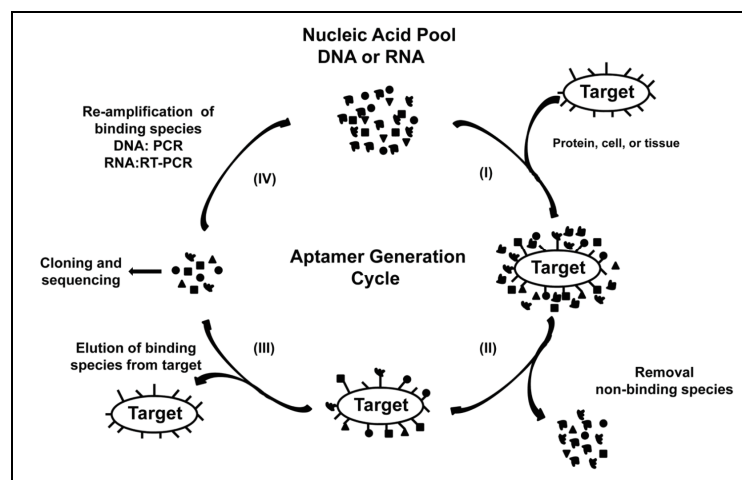


**Fig. 19** Generation of aptamers by SELEX. I) Aptamer pools are incubated with target for binding. II) Targets are thoroughly washed to remove non-binding species. III) Target-bound

aptamers are eluted from the target. IV) Amplification of candidate aptamers by PCR (DNA) or RT-PCR and transcription (RNA). Steps I-IV is repeated for multiple rounds to deplete non-binders and enrich for target-binders. Following the final round of selection, binding nucleotides are cloned and sequenced to determine the specific nucleotide composition.

Due to this specific procedure of selection, based on multiple rounds of target selection and enrichment, aptamer pools show high binding affinity for the target of interest.

In addition aptamers, if compared to standard proteins, show higher stability, and ease of chemical modification. Aptamers production is fully automated, highly reproducible and low cost. Moreover, aptamers are naturally integrable in the context of DDI: DNA aptamer constructs are produced simply by adding a surface binding sequence to the aptamer during oligo-synthesis.

#### **4. THE POTENTIAL OF NANOSCALE TOOLS IN A MULTI-INTEGRATED APPROACH FOR CANCER ASSESSMENT**

Tumors are complex and heterogeneous systems where different subclonal tumor populations and a variety of non-tumor cells coexist in a constantly evolving manner. The interactions between molecules and between cells and between molecules and cells that arise as a result of these alterations are even more complex [99]. Due to the complexities of cancer phenotypes and genotypes the characterization of specific molecular and biochemical details of cancer cells would be instrumental in evaluating tumors and in better driving diagnosis, prognosis, and therapy.

However the clinical significance and the precise role of many receptors remains uncertain and not fully proved: it is a general opinion that this issue deserves further studies in large prospective trials, together with *in vitro* studies to elucidate fundamental aspects of receptor-mediated signaling involved in cancer progression and occurrence.

In this direction a systematic, integrated, multi-disciplinary approach to elucidate and correlate some molecular aspects of cancer development could be a powerful strategy towards more effective cancer detection and enduring therapies. The employment of a combination of methods and integrated analyses can lead not only to the understanding and modelling of the expression/activity of cancer cells receptors but also to the correlation of receptors interactions with their predictive value as cancer biomarkers.

In particular we aim at assessing the correlation between overexpression, dimerization and activation of cancer-involved receptors and the release of receptor domains to the

bloodstream, in normal and cancer cells, to determine the significance of quantifiable, easily detectable molecular signal for tumor analysis. Such complex molecular interactions need to be analyzed in a wide range of length scale (from few nm to hundred microns) and call for merging information from advanced high-resolution and super-resolution microscopies (membrane protein localization, quantification and co-localization of different biomarkers) and nanotechnology-based diagnostic tools (high sensitivity detection of protein and vesicle biomarkers).

Addressing the complexity and variability of individual tumors by means of this kind of innovative platforms and identifying clinically useful biomarkers will be fundamental to pave the way to the development of new diagnostic strategies, to help defining personalized therapies and produce responses of enduring efficacy [100].

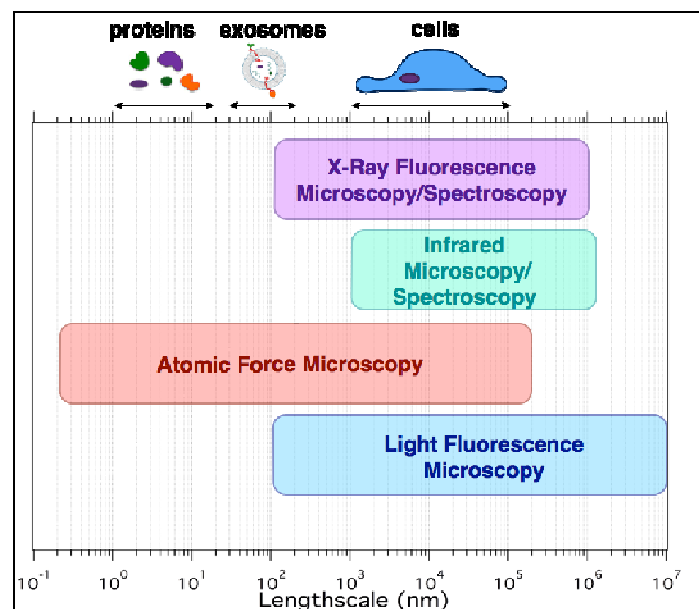


**Fig. 20** Example of a multi-integrated approach: exploring a wide range of length scale (from few nm to hundred microns) and exploiting different advanced microscopies it is possible to study specific characteristics of cells and their nearby microenvironment and to merge information coming from different analysis.

## RESULTS

### 5. NANOARRAYS DEVELOPMENT AND OPTIMIZATION <sup>1</sup>

In this work we propose an atomic force microscopy (AFM)-based miniaturized bioaffinity test for the quantification of the circulating Human Epidermal Growth Factor Receptor 2 (Her2). This approach capitalizes on other studies performed in our group [101,102,103], in which the full potentiality of innovative nanoarray platforms has been exploited for diseases biomarkers detection based on the precise confinement of high affinity antigen-binding molecules on a surface by means of AFM nanografting.

To move towards clinical applications we studied here the feasibility of different binders with different affinity/recognition epitope. In particular, we used two different mouse IgG monoclonal antibodies (Abs) selected for their high binding affinity to regions outside the epitope recognized by Trastuzumab, suitable therefore for monitoring the disease during therapeutic drug treatment. Then, we explored alternative binders such as high affinity single-domain nanobodies (VHH) (12-15 kDa) selected to bind epitopes in the Her2 hinge region.

#### 5.1 MOUSE ANTIBODY-FUNCTIONALIZED NANOARRAYS

We used two mouse monoclonal antibodies, MGR2 and MGR3, for the setup and validation of the nanoarray. Both antibodies recognize with high efficiency the ECD-Her2 fragment and have been thoroughly characterized in immunoprecipitation experiments and by immunohistochemistry using Her2 overexpressing cell lines [104,105]. Epitope binning experiments demonstrated that MGR2 and MGR3 bind to independent epitopes on the protein surface, both of which not overlapping with the epitope bound by Trastuzumab [105].

##### 5.1.1 Ab-DNA conjugates production and characterization

Towards the realization of the nanoassay, we first conjugated the two antibodies with ssDNA by means of a commercial click chemistry kit that exploits amine groups available on the Ab protein surface for covalently anchoring the DNA sequences (Fig. 21). Such bioconjugation is a three steps procedure in which first both protein and DNA are

---

<sup>1</sup> “Boosting sensitivity of clinically-relevant circulating biomarker detection: a delicate balance of miniaturization, robustness and proper binder choice for readout optimization” **E. Ambrosetti**, P. Paoletti, A. Bosco, P. Parrisè, D. Scaini, E. Tagliabue, A. de Marco, L. Casalis. *Submitted to ACS Omega*

modified with specific chemical groups, then the two modified biomolecules are made reacting, resulting in the formation of a stable protein-DNA bond.

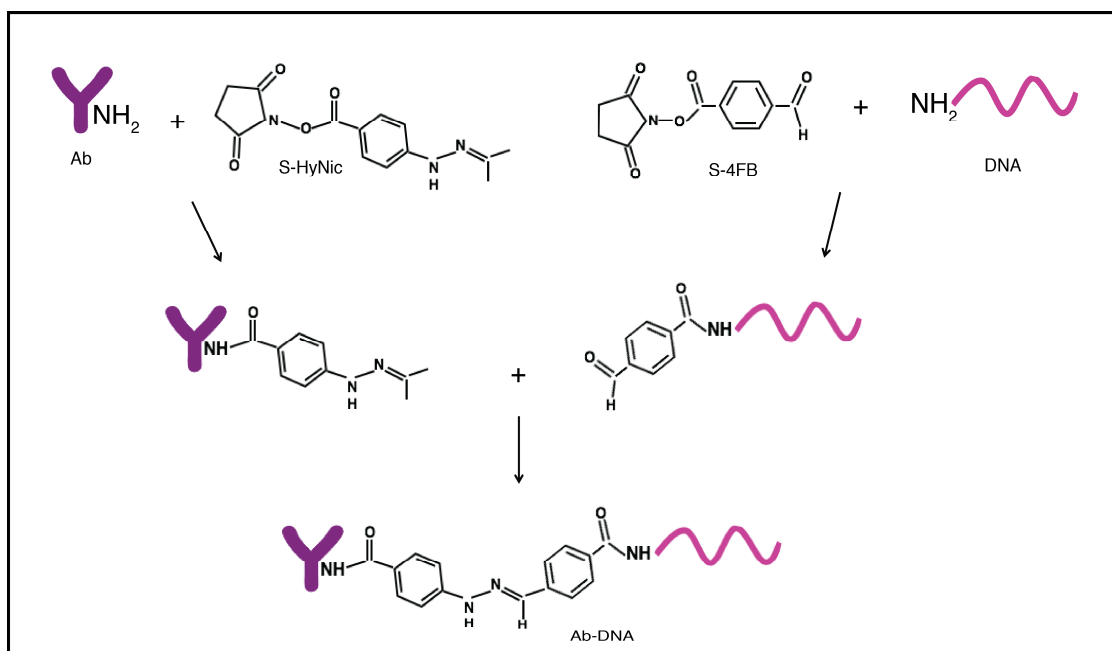


**Fig. 21** Schematic representation of antibody-DNA conjugation reaction: first the Ab is functionalized with S-HyNic group and DNA is linked to S-4FB group. Then these two groups react to provide a covalent Ab-DNA conjugate.

This method shows many advantages: it is a highly efficient (>80% of the protein is conjugated) and high yielding reaction. The produced conjugate is extremely stable and the reaction conditions are mild avoiding protein denaturation and no metals, oxidation or reducing reagents are needed. Moreover the modifications made both on the protein and on the oligonucleotide are quantifiable using colorimetric assays. This helps in facilitating the reproducibility of the reaction by accurate characterization of all components. Finally the total degree of DNA-protein functionalization is quantifiable by UV spectrophotometry, since the bis-arylhydrazone group formed in the DNA-protein anchoring points adsorbs at a specific wavelength (354 nm). In this way, calculating the ratio between the determined concentration of bis-arylhydrazone groups and the relative concentration of protein it is possible to simply obtain a quite accurate estimation of the number of conjugated DNA sequences per antibody. It has to be underlined that all conjugation reactions result in a mixture of reaction products consisting of the desired conjugate along with some un-conjugated modified oligo. For this reason, the conjugation reactions are purified using size exclusion chromatographic methods.

To avoid multiple strands attached to a single Ab, sterically limiting the binding affinity to

the target, we optimized the original conjugation protocol obtaining on average two-three strands per protein, and in any case never more than four. This low degree of DNA functionalization is desirable in order to have a lower impact on Ab binding capability: all primarily amines from lysines exposed on protein surface are potentially available for the modification. Decreasing the number of DNA sequences conjugated per protein reduces the probability to have one DNA attached to the lysine residues in the vicinity of the paratope, potentially affecting the antigen recognition [106].

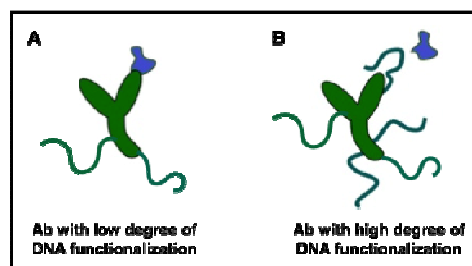


**Fig. 22** Schematic representation of Ab functionalization by means of DNA sequences. The low number of DNA tails anchored to the Ab (A) has a lower influence on its interaction with the specific target with respect to an Ab functionalized with a high number of DNA sequences (B).

After conjugation, SPR experiments have been performed to understand how the functionalization affects the Ab affinity for the specific antigen.

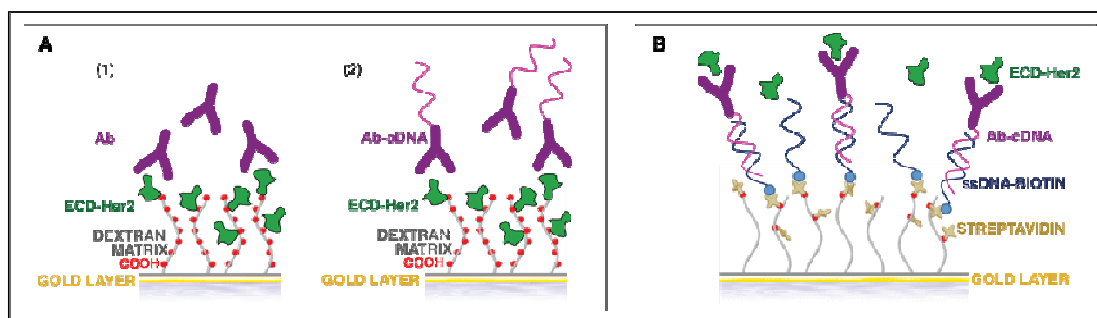


**Fig. 23** Schematic representation of the different SPR experimental approaches. In the first assay configuration (A) ECD-Her2 is the ligand covalently immobilized on CM5 surface and Ab (1) or Ab-cDNA conjugate (2) are the analyte run over the surface. In the second assay configuration (B) the ssDNA is attached on streptavidine (SA) surface through streptavidin-biotin bond; then the ligand Ab-cDNA conjugate is immobilized by hybridization and the ECD-Her2 is run as analyte over the surface.

In the first SPR experimental design (Fig. 23A), ECD-Her2 was immobilized by amine coupling reaction to the dextran matrix on the chip and the apparent binding affinities of

Abs and Ab-conjugates used as analytes were assessed. We have to point out that in the specific experimental configuration the ECD-Her2 amine groups involved in the interaction with the dextran matrix are randomly explored. Due to this immobilization process some antigen molecules could have the region of binding with the Ab partially or totally not available, causing an underestimation of the affinity determined in such measurement. However these experiments have a comparative, qualitative meaning. The  $K_D$  values found and summarized in Table 1 indicated that the DNA functionalization significantly affected the binding capability of the MGR2 and MGR3 binders, lowering their binding affinity 10 and 6.5 times respectively, probably due to the steric hindrance of DNA moieties.

	Biacore (Experimental approach A)	Biacore (Experimental approach B)
<b>MGR2</b>	$38 \pm 2$	
<b>MGR2-cDNA</b>	$367 \pm 33$	$17.1 \pm 1.1$
<b>MGR3</b>	$91 \pm 3$	
<b>MGR3-cDNA</b>	$590 \pm 32$	$30.4 \pm 2.3$

**Table 1** Summary of binding affinity constant ( $K_D$  - nM) of monoclonal Antibodies (alone or conjugated) for ECD-Her2, measured by SPR technique.

To better mimic the working conditions of our nanoarray, we performed SPR measurements using an alternative configuration (Fig. 23B). First the biotinilated-ssDNA was attached to the chip through biotin-streptavidin coupling (using a dextran matrix functionalized with streptavidin); then it was hybridized with the Ab conjugated with the complementary ssDNA strand. ECD-Her2 was used as analyte. This approach showed an easier interaction between antigen and antibodies and a  $K_D$  in the low nanomolar range (MGR2  $17.1 \pm 1.1$  nM; MGR3  $30.4 \pm 2.3$ ) ensuring that efficient antigen recognition is enabled in the nanoarray configuration. All the SPR results are reported in Table 1.

### 5.1.2 ECD-Her2 detection: calibration curve and sensitivity

For nanoscale functionalization, we combined DNA nanografting, fine-tuning the process to optimize the density of patterned biomolecules [102], and the semisynthetic Abs-DNA conjugates immobilization through DDI with high efficiency, site-selectivity and reversibility [86,107] (Fig. 24).



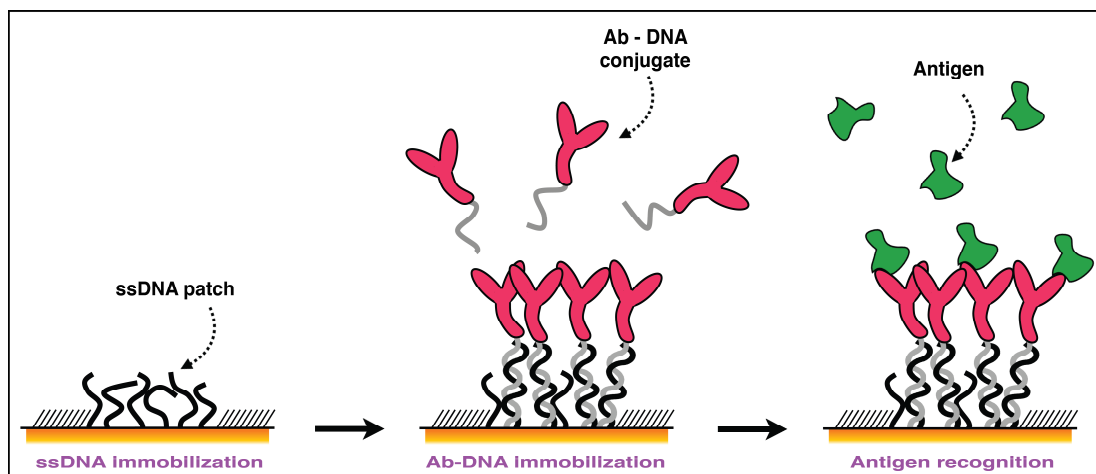


**Fig. 24** Schematic representation of the DDI strategy to immobilize antibodies on the micro-sized DNA-based biosensor.

We then capitalized on AFM topographic imaging to visualize any change in the nanopatches surface topography occurring upon interaction with the antigen, with sub-nanometric resolution, and to quantify the number of biorecognition events, as successfully demonstrated in previous works published by our group [86,101,102,107,108]. Topographic height variations of the nanopatches have been measured with AFM in gentle contact mode in liquid using a softer AFM tip (see Materials and Methods); applying during measurement a force at the minimum stable value ( $\approx 0.1$  nN) guarantees the minimum perturbation and hence the precision of the molecular height detected [102]. It is worth to point out that gentle contact imaging, while not suitable for single biomolecules on surfaces, is appropriate to image laterally packed 2D DNA NAMs/SAMs, and that provides higher resolution with respect to NC or tapping imaging modes (as from the Lennard-Jones potential of Fig. 9).

The height of the patch is measured as the average of all the values recorded in the entire patch area, at each step of the assay fabrication (i.e. ssDNA nanografting; DDI of Abs-DNA conjugates; antigen binding), with respect to the surrounding SAM of bio-repellent alkanethiols. To protect the surface from non-specific biomolecules binding, we first protected the gold film with a self-assembled monolayer of alkanethiols ( $C_{11}$ ) modified with 6 ethylene-glycol (EG) units at the end. We named it TOEG<sub>6</sub> SAMs (top-terminated ethylene-glycol 6 alkanethiol SAM). The hydrophilic nature of EG portion of the film keeps the hydration shell of any biomolecule in solution intact, preventing non-specific adsorption [110,111,112]. This has been tested in our experiments through roughness measurements: this value was approximately 0.2 nm, and did not change at any level of

device implementation. The anti-fouling nature of the TOEG<sub>6</sub> SAM allows our device to work even in complex matrices, avoiding false positive results, as mentioned in the Introduction section.

The binding of 10 nM ECD-Her2 over MGR2 and MGR3 antibody nanostructures, respectively, is reported in Fig. 25. The images of the nanopatches (Fig. 25A and 25D) show the height increase at each step of the assay formation, till antigen binding (brighter is the colour higher is the nanoassembly height versus the reference SAM). Relative height variations determined from the AFM images, with respect to the TOEG<sub>6</sub> SAM ( $3.4 \pm 0.3$  nm [109]), are visualized showing the topographic lines profiles (Fig. 25B and 25E). Relative height values at each steps of nanoarray development are given in tables (Fig. 25C and 25F).

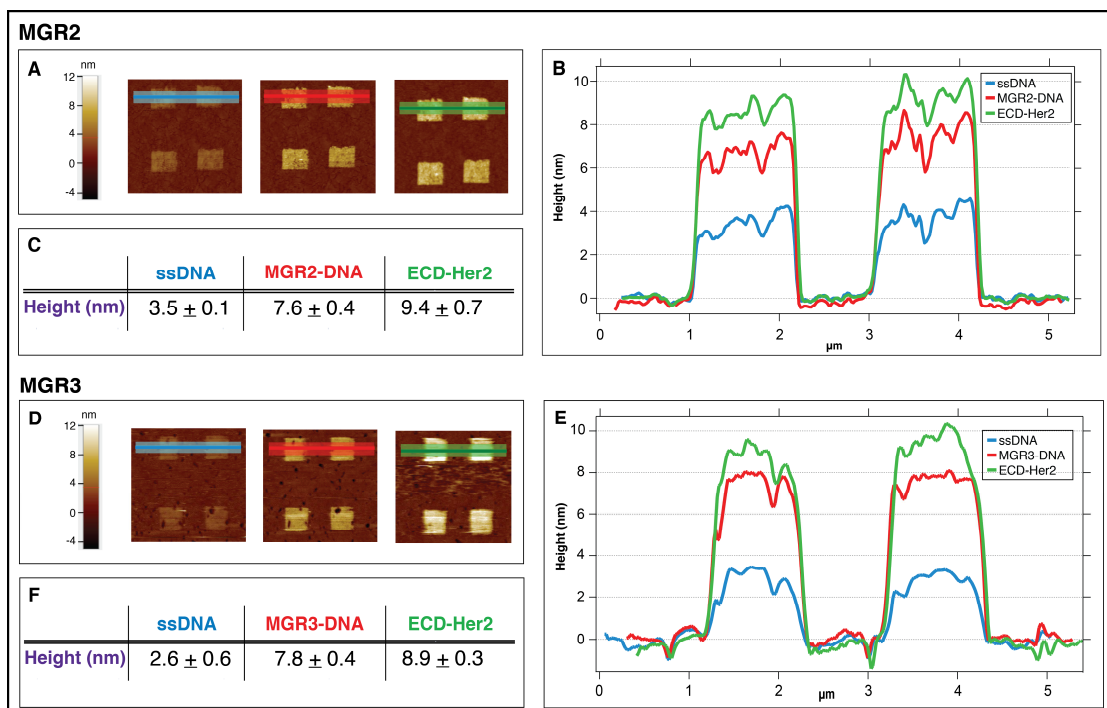


**Fig. 25** ECD-Her2 nanoarray detection by means of MGR2 (A, B, C) and MGR3 (D, E, F) Abs, respectively. (A, D): AFM images across the nanopatches after DNA immobilization, antibody loading via DDI and binding of the antigen. (B, E): Relative topographic line profiles from AFM images A, D (light blue: DNA nanografting; red: Ab-conjugate immobilization via DDI; green: 10 nM ECD-Her2 binding). (C, F): Mean and SD values of the patch heights as measured from the line profiles across the nanopatches in correspondence of the colored areas of images A, D at each step of the experiment.

In all cases, the average height of the thiol ssDNA's nanopatches (Fig. 25B and 25E, blue lines) is close to 3.0 nm. This experimental value is in agreement with what expected for

“low density” nanografting conditions ( $S/A = 0.3-0.6$ ) in which the vertically standing thiolated DNA molecules are below the highest packing limit (the height of the fully stretched DNA in this specific ionic strength conditions (1 M NaCl) is around 6 nm [109]) and therefore not fully vertically stretched by the electrostatic repulsive forces [113]. This DNA density has been identified as the optimal one to accommodate the steric hindrance of the subsequently immobilized antibodies and to make their binding site easily accessible to the analyte in solution. In fact the ssDNA density affects hybridization of the conjugate and so the detection of Her2. As shown in Fig. 26 only at “low DNA density” it is possible to obtain an efficient hybridization of Ab-cDNA (height increase after conjugate incubation); this is due to the fact that the large dimension of the antibody requires spacing between ssDNA molecules in order to avoid steric hindrance problem and to efficiently bind via DDI. All the data of Fig. 25 are relative to this class of “low DNA density”.

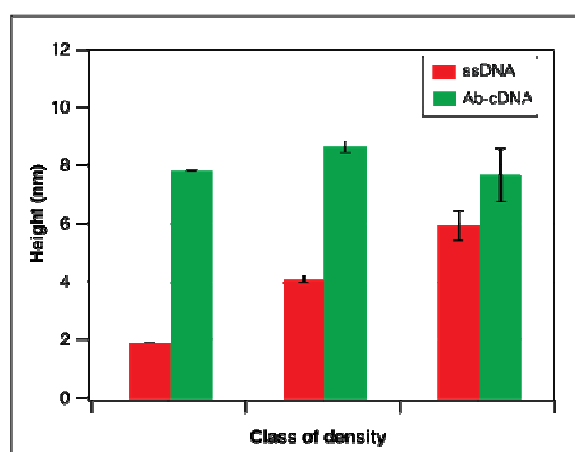


**Fig. 26** Histogram created collecting different experiments (number of experiments: 30); data are subdivided into three classes of density ( $S/A = 0.3 - 0.6 - 2.6$ ). Error bars represent the standard deviation; red: grafting of ssDNA; green: hybridization of Ab-DNA conjugate.

DNA-antibody conjugates immobilization determines a height increase of roughly 4-5 nm (Fig. 25B and 25E, red lines). The further height increment after the incubation with ECD-Her2 (Fig. 25B and 25E, green lines) clearly indicates the efficient antibody-dependent antigen capture.

Next, the nanodevice has been used for the quantitative determination of the target. We calculated the affinity calibration curve for both MGR2 and MGR3 assuming that the variation in height across the nanopatches is proportional to the amount of analyte

bound to the ligand. Height variations were plotted versus ECD-Her2 concentrations ranging from 200 pM to 100 nM in the case of MGR2 and from 1 nM to 300 nM in the case of MGR3 (Fig. 27).

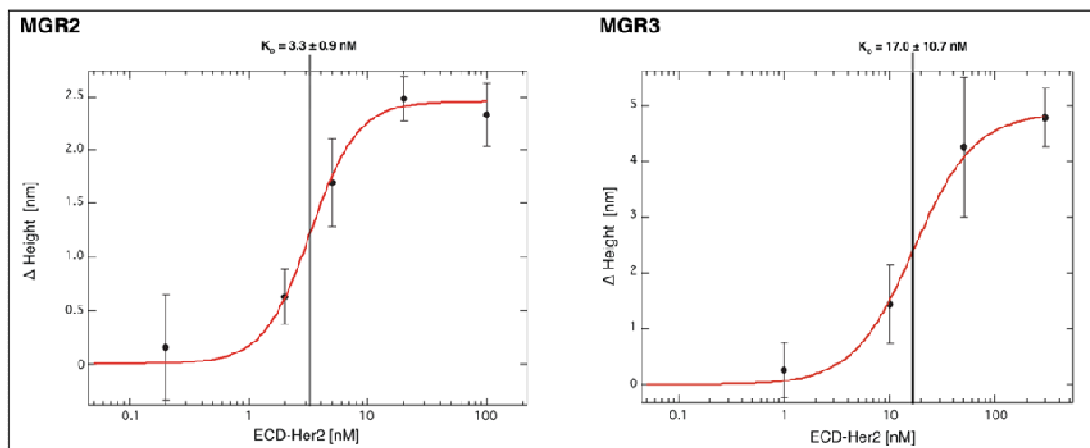


**Fig. 27** ECD-Her2 binding curves on MGR2- (left) and MGR3-DNA (right) conjugates immobilized on the nanoarray, respectively. The average values of height variation ( $\Delta h$ ) detected on nanopatches ( $n=4$ ) have been plotted versus ECD-Her2 concentration. Data have been analysed with Hill equation sigmoidal fitting and  $K_D$  determined.

The sigmoidal distribution of data is in agreement with the saturable binding isotherm for a receptor-ligand binding equilibrium and was fitted with the Hill equation [114], obtaining a dissociation constant  $K_D$  (the parameter that defines the binding affinity of two molecules) in the low nanomolar range for both MGR2 ( $K_D = 3.3 \pm 0.9$  nM) and MGR3 ( $K_D = 17.0 \pm 10.7$  nM). From data of Fig. 27, we determined a limit of sensitivity (LoB – see Materials and Methods) of about 1 nM for the higher affinity MGR2 and 3 nM for MGR3. Although good, these sensitivity values need to be improved in order to reach the current FDA-approved serum Her2 level cutoff ( $\approx 200$  pM); we plan to complete the optimization moving from nanoarray validation to optimization phase, where sensitivity and the proper binder choice will be the crucial aspects of the study. To validate the nanoarray results, we set up a standard ELISA assay in which different concentrations of the same Abs were added in ECD-Her2-coated wells (Fig. 28).

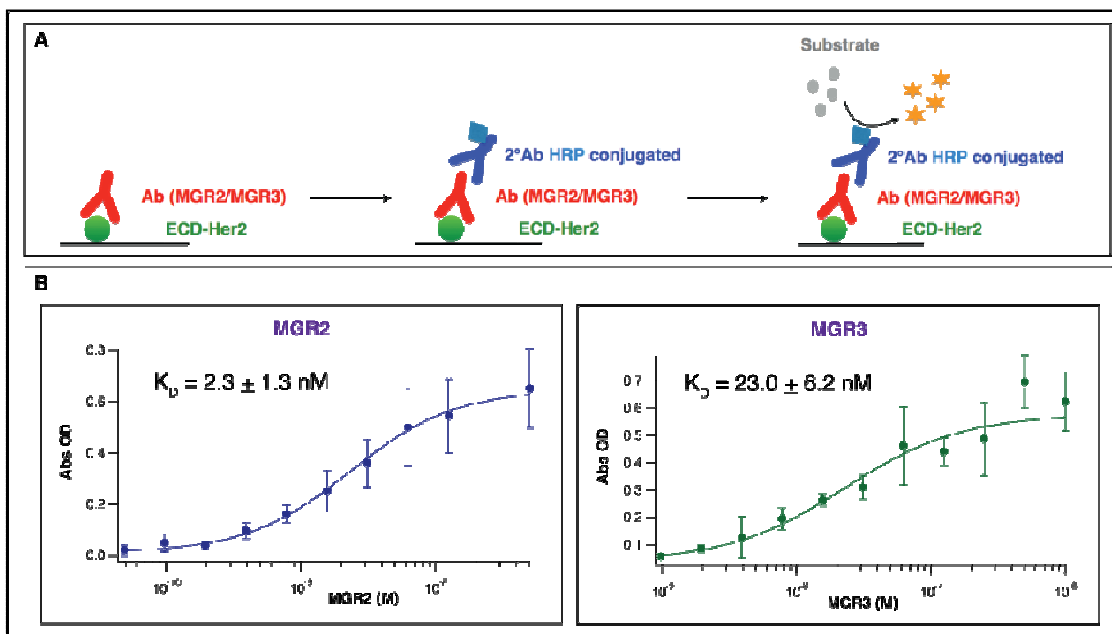


**Fig. 28** Indirect ELISA. (A) Schematic representation of the assay. (B) Determination of binding affinity between ECD-Her2 and Antibodies (MGR2 and MGR3). Absorbance is measured at 450 nm and plotted as a function of Ab concentration. Data are fitted with Hill equation.

The dissociation constant values found with this assay (MGR2:  $K_D = 2.3 \pm 1.3 \text{ nM}$ ; MGR3:  $K_D = 23.0 \pm 6.2 \text{ nM}$ ) were in very good agreement with those found with the nanoarray (Confidence Level (CL) = 0.74 and 0.69 respectively). The different experimental setup justifies the quite higher  $K_D$  value obtained with SPR in the nanoarray-like configuration with respect to the nanoarray and ELISA; nonetheless the value in the low nanomolar range guarantees an efficient antigen recognition in a nanoarray-like configuration.

### 5.1.3 Comparison with Trastuzumab-functionalized nanoarray detection

Since Trastuzumab is the humanized Ab used as therapeutic agent in standard clinical practice and as such it has been chosen and optimized to bind the target with high affinity, it is significant to compare the  $K_D$  of our mouse monoclonal Abs with that one of Trastuzumab, functionalized and immobilized on the nanoarray surface with the same approach used for MGR2 and MGR3 and starting also in this case from a “low DNA density”. As shown in Fig. 29 for Trastuzumab we found  $K_D = 3.2 \pm 0.01 \text{ nM}$  that is perfectly comparable with the value found for MGR2 and not so far from that one of MGR3; the  $K_D$  of Trastuzumab-Her2 interaction reported in other works [86,110] varies depending on the technique used for the affinity determination. The values span from picomolar (*in vitro* assay in solution) to low nanomolar (cell-based assay); the affinity in the

low nanomolar range found with our “surface assay” demonstrates that our strategies of functionalization and immobilization of an high affinity antibody preserved anyhow a range of binding capability sufficient for a sensitive detection.

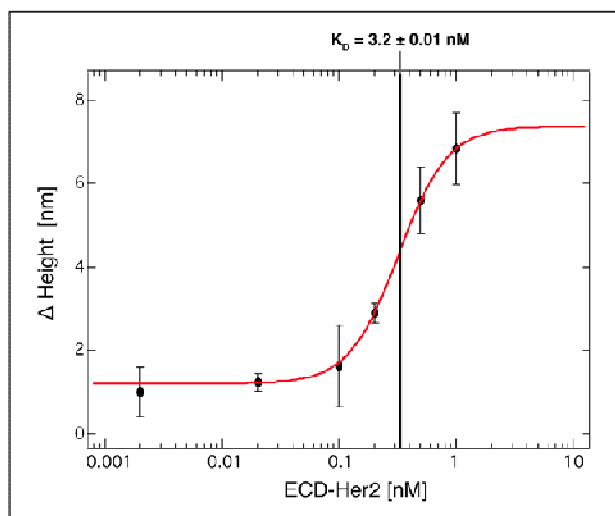


**Fig. 29** Binding curve of ECD-Her2 and Trastuzumab conjugate immobilized on nanoarray surface: the average values of height variation ( $\Delta h$ ) detected on nanopatches have been plotted versus ECD-Her2 concentration. Data have been analyzed with Hill equation sigmoidal fitting.

## 5.2 CAMELID NANOBODY-FUNCTIONALIZED NANOARRAYS

In alternative to conventional antibodies, we exploited here camelid nanobodies, recombinant molecules that can be easily engineered at precise and unique residues to avoid multiple and heterogeneous labeling and loss of activity. Moreover, due to their reduced dimensions, nanobodies can be used to prepare functional surfaces with higher ligand densities compared to conventional antibodies, hence simultaneously increasing the active detection surface and avoiding steric hindrance. In particular, it has been demonstrated the advantage of producing nanobodies specialized for ECD-Her2 biorecognition with a free C-terminal cysteine available for single-point maleimide functionalization [115]. This approach enables functionalization using residues not involved in the Ab paratope consequently preventing modifications of the Ab-antigen binding features. The llama nanobody EM1 has been selected *in vitro* from a naïve library [116] using the same strategy reported in Djender *et al.* [117]. It binds to an ECD-Her2 epitope close to the one recognized by Trastuzumab.

### 5.2.1 VHH-DNA conjugates production and characterization

EM1 was expressed with a free C-terminal cysteine and covalently linked with a maleimide-ssDNA construct (Fig. 30).

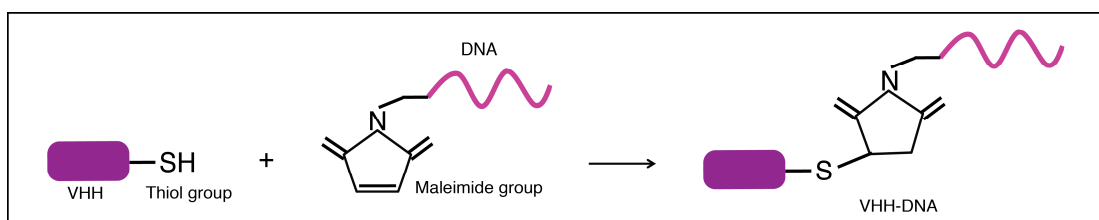


**Fig. 30** Schematic representation of nanobody-DNA conjugation reaction: the Cys thiol group at the C-term of VHH reacts with the maleimide group attached to the 5' end of the DNA sequence.

Similarly to what discussed in paragraph 5.1.1, we measured the binding properties of 1:1 EM1-ssDNA conjugates by SPR (in the nanoarray-like configuration), finding a  $K_D$  of  $3.4 \pm 0.3$  nM.

### 5.2.2 ECD-Her2 detection: calibration curve and sensitivity

We proceeded with nanobody-DNA conjugate nanoscale immobilization on the gold surface with the same DDI approach used for MGR2 and MGR3 antibodies. The two first preliminary steps (grafting of ssDNA, hybridization of DNA-nanobody conjugate) were optimized according to the small dimensions of VHHs ( $2 \times 2 \times 3$  nm;  $\sim 15$  kDa [93,94]). Notably, the density of grafted ssDNA sequences has a great impact on the hybridization of the conjugate and consequently on the detection of Her2. While in the case of full antibodies low DNA densities are needed to avoid steric hindrance effects, for nanobodies we should pay attention not to leave voids in the nanografted DNA SAM into which the nanobody itself could hide, becoming unavailable for the interaction with the analyte (Fig. 31A). On the contrary, at high DNA density the nanostructures are well packed and the binder stands up over the DNA layer surface in the right configuration (Fig. 31B).

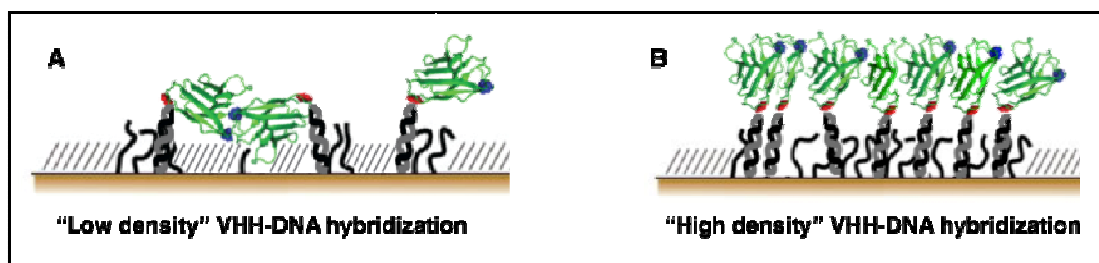


**Fig. 31** Schematic representation of DNA density impact on VHH-DNA conjugates configuration over the gold surface.

This explains why, as shown in the Fig. 32, conditions for highly performing target

detection were reached only at high density.

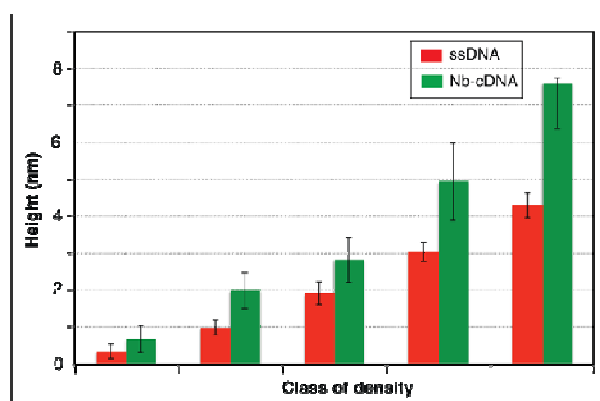


**Fig. 32** Histogram created collecting different experiments (number of experiments: 30); data are subdivided into classes of density related to ssDNA relative height. Error bars represent the standard deviation; red: grafting of ssDNA; green: hybridization of Nb-DNA conjugate.

Tuning DNA density and DDI conditions depending on the dimension and the specific characteristics of the binders to optimize detection performance in the immunoassay is a unique feature of AFM nanografting.

Once optimized the immobilization conditions we performed ECD-Her2 detection with EM1 conjugate nanostructures, following the same experimental procedure used for Abs (ssDNA grafting, DDI-driven conjugate immobilization and target binding). As a representative case we report the results related to the detection of 1 nM ECD-Her2 (Fig. 33).

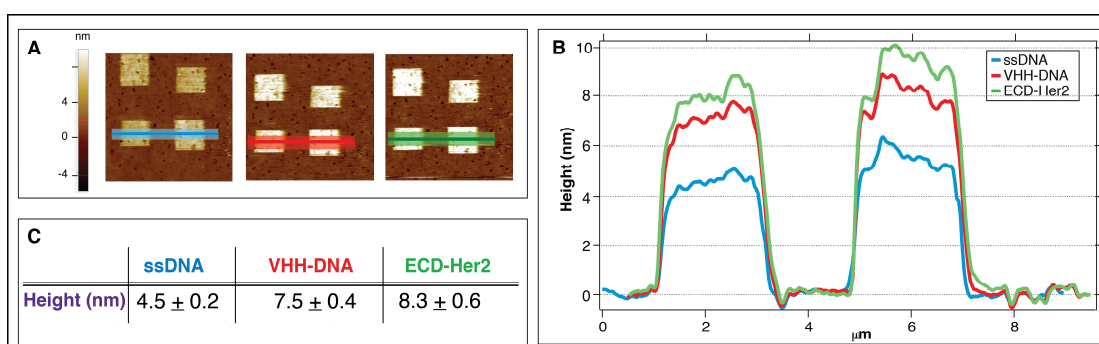


**Fig. 33** Detection of ECD-Her2 on nanoarray. Images of the nanopatches on the gold surface (A) and their relative height topographical profiles (B). (C) Average and Standard Deviation values of the height are measured across the nanopatches at each step of the experiment (light blue: grafting of ssDNA; red: hybridization of VHH-DNA conjugate; green: ECD-Her2 1 nM incubation).



The measured relative height of the “high density” grafted ssDNA is  $4.5 \pm 0.2$  nm, a value that describes the highest packing nanopattern in which the thiolated DNA molecules are vertically standing [109].

As provided for MGR2 and MGR3 Abs, we determined the EM1-ECD-Her2 binding affinity curve with different analyte concentrations ranging from 200 pM to 30 nM (Fig. 34).

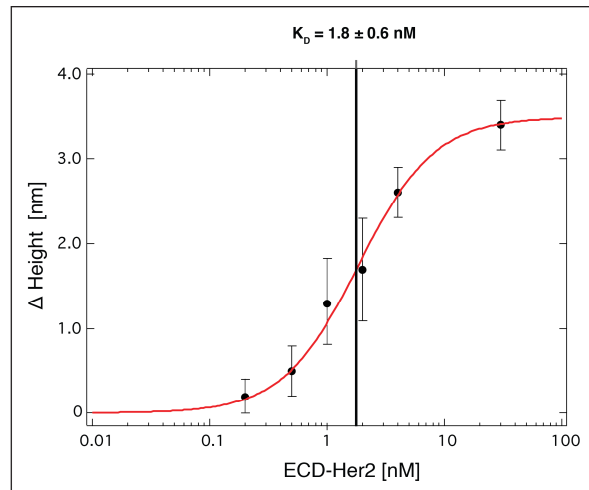


**Fig. 34** Binding curve of ECD-Her2 and EM1 nanobody conjugate immobilized on nanoarray surface. The average values of  $\Delta$  height detected on nanopatches ( $n=8$ ) have been plotted versus ECD-Her2 concentration; data have been analysed with Hill equation sigmoidal fitting and  $K_D$  determined.

Also in this case, we fitted data with Hill equation, determining a dissociation constant value of  $K_D = 1.8 \pm 0.6$  nM, lower than for MGR2. The S/N ratio improves substantially moving from antibody- to nanobody-binders, probably because the higher density DNA layer underneath increases the mechanical robustness of the device: the readout in fact is based on a mechanical probe which, although operated at minimum force, still reflects the mechanical resistance of the surface. Overall the limit of sensitivity decreases to about 200 pM, pushing the nanoarray sensitivity to a level comparable to the cutoff value of 15 ng/ml ( $\approx 200$  pM) which is commonly used in clinic for Her2 positive breast cancer assessment [34,36]. Although this result is already very sound, we would like to stress here the fact that in principle, the nanoarray sensitivity could be further improved up to the low picomolar range by exploiting new computational/experimental protocols for accelerating the evolution of new biosynthetic binders with increased affinity and specificity. In this direction we plan to identify *in silico* customized VHHs for specific (non-immunogenic) epitopes of

Her2 fragments by means of computational design [118] and/or high-affinity peptides for chosen epitopes of target proteins by stochastically exploring their sequence and structure space.

### 5.3 REGENERATION OF THE NANOARRAY

Regeneration is the process of removing bound antigen from the Ab/Nb functionalized nanoarray surface after each sample analysis incubation, in order to prepare the device for the next analysis cycle.

Efficient regeneration is a crucial step for a successful assay: a complete regeneration and the maintenance of the binding activity from the surface guarantee the performance of the assay and a longer useful lifetime of the nanoarray. Regeneration of the surface with a chemical treatment could be avoided if the antigen dissociates fast enough and all molecules may be removed within a reasonable time simply by washing with buffer. When the spontaneous dissociation is not sufficient it is necessary to determine suitable regeneration conditions.

We tested many regeneration conditions evaluating the dissociation of a high ECD-Her2 concentration (50 nM) from MGR2-functionalized nanoarray: low pH (1.5–3), high pH (10), high ionic strength (5 M NaCl) solutions.

Among the different chemical treatment tested we identified as best condition the use of Glycine-HCl 12mM pH 2.0; it leads to a successful result since, as shown in Fig. 35, after such treatment the height across the nanopatch recovered almost the same value the conjugate only present on the surface, before ECD-Her2 binding. In another step, we also verified that the conjugate after regeneration doesn't lose its capability to rebind Her2.

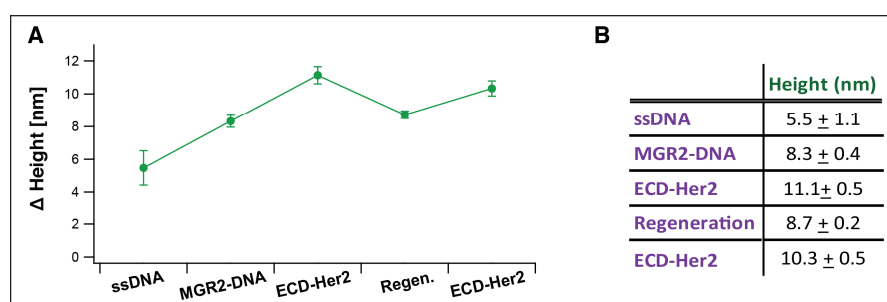


**Fig. 35** Regeneration of the nanoarray. (A) Relative height of the nanopatches at each step of the experiment (grafting of ssDNA; hybridization of MGR2-DNA conjugate; ECD-Her2 50 nM incubation; regeneration with Glycine-HCl 12mM pH 2.0, second incubation with ECD-Her2 50 nM) is plotted. (B) Average and Standard Deviation values of the height are reported on the table.

The possibility to regenerate the nanoarray not only proves the robustness of the molecular assembly on the surface but also offers a great advantage in the experimental tests to setup the assay, since it allows performing different trials avoiding the wastage of materials and molecular reagents. Although for clinical devices a disposable approach is preferred, during their optimization phase the capability to regenerate the active surface might be strongly helpful.

#### **5.4 ECD-Her2 DETECTION IN STANDARDIZED HUMAN SERUM**

As intermediate step to move towards detection in blood serum samples we tested the capability of the nanoarray to recognize the target of interest in human serum. We chose to work with standardized human serum, which in terms of protein content (60% IgG antibody and 20% albumin w/w with respect to the total protein content) mimics the serum of human patients. First, we assessed unspecific protein binding to the nanobody-functionalized patches and/or to the surrounding thiol carpet. As shown in Fig. 36A we observed a negligible increase of patch height (about  $0.2 \pm 0.4$  nm) upon moving from PBS to standardized human serum (in absence of antigen). Also, the roughness of the biorepellent SAM carpet did not change sensitively (Rms = 0.23 nm and 0.25 nm, before and after serum incubation, respectively). This is a crucial result, since the TOEG<sub>6</sub> SAM is for us the reference level to assess all the changes on the sensitive part of the assay. The biofouling properties of the TOEG<sub>6</sub> SAM seem to be maintained also when measurements are performed in matrices more complex than PBS. Upon addition of 1 nM ECD-Her2 to the serum, and using a nanoarray configuration with a high-density NAM of nanobodies, we observed a relevant patch height increase of 1.3 nm (Fig. 36A). Considerably this value is the same of the differential height increase value  $\Delta h$  extracted in correspondence to an ECD-Her2 concentration of 1 nM in the calibration curve obtained with the recombinant protein in buffer solution. This further proves that our nanoarray is capable to filter the background noise of a biological sample and recognise the specific biomarker of interest.

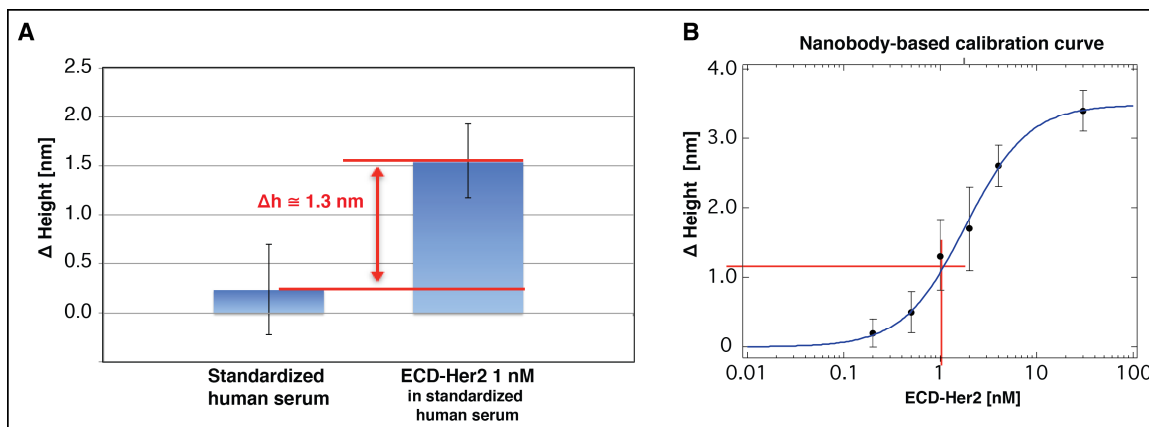


**Fig. 36** ECD-Her2 detection in standardized human serum. (A) Nanopatches height variation ( $n=8$ ) on nanobody-immobilized nanoarray incubated with standardized human serum with or without ECD-Her2 1 nM; the two variations are statistically different ( $p \ll 0.05$ ). (B) Extrapolation of the height increase expected from the nanobody-based calibration curve presented in Fig. 34.

As additional test to validate the ECD-Her2 detection in standardized serum we repeated the measurements using test explained before using a NAM of Abs as binders (Fig. 37). In this case we observed a quite higher increase of patch height (about  $1.5 \pm 0.7$  nm) upon moving from PBS to standardized human serum, in the absence of antigen. This evidence could be explained by the fact that the density of the DNA patch is lower with respect to that one created for nanobody-functionalized nanoarray. The presence of a certain distance between DNA molecules could allow the permeation of serum protein and therefore determine a slight aspecific binding. However the binding affinity of MGR2 is preserved: upon addition of 10 nM ECD-Her2 to the serum another significant patch height increase of 1.5 nm (Fig. 37A) was obtained.

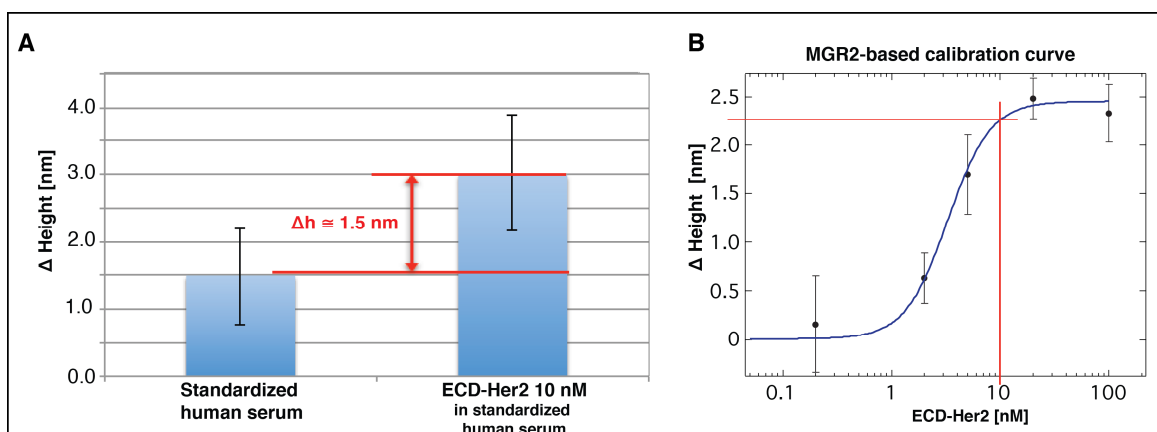


**Fig. 37** ECD-Her2 detection in standardized human serum. (A) Nanopatches height variation ( $n=8$ ) on MGR2-immobilized nanoarray incubated with standardized human serum with or without ECD-

Her2 10 nM; the two variations are statistically different ( $p < 0.05$ ). (B) Extrapolation of the height increase expected from the MGR2-based calibration curve presented in Fig. 27.

Also in this case the differential height increase has been compared with that one extrapolated from the calibration curve obtained using the recombinant protein in buffer solution; the slight discrepancy could be due to the presence of a non-specific binding of the serum alone, as explained before, that affects somehow the measurement.

Therefore if we consider the two assays, performed with nanobody- and antibody-functionalized nanoarray respectively, it is evident that reducing the non-specific binding by the molecular constituents of the complex matrix in which the biomarker of interest is dissolved is a crucial step to improve the precision of the quantitative analysis.

## 5.5 MULTIPLEXED DETECTION

To further challenge the nanoarray and to prove its validity in clinical practice, we performed a preliminary multiplexing analysis, testing the simultaneous detection of ECD-Her2 and uPA, another relevant breast cancer biomarker.

Urokinase plasminogen activator (uPA) is an extracellular matrix-degrading protease involved in cancer invasion and metastasis, interacting with plasminogen activator inhibitor-1 (PAI-1); in the last years several retrospective and prospective studies have shown that elevated levels of uPA and PAI-1 in breast tumor tissue are prognostic biomarkers as powerful predictors of poor patient outcome, including adverse outcome in the subset of breast cancer patients with lymph node-negative disease [119]. Moreover it has been demonstrated that in some cases uPA is secreted as pro-urokinase (53 kDa) and released in bloodstream [120], hence representing a good candidate as circulating biomarker.

As shown in Fig. 38, we grafted two DNA sequences of the same length (cF5 and cF9, see Materials and Methods section) complementary to the conjugated tail of, respectively, the  $\alpha$ -uPA Ab and EM1 VHH. Then we introduced the two conjugated binders and the respective antigens, following the order reported in the legend of Fig. 38B (from the top to the bottom). Relative height profile variations across the functional spots are reported in Fig. 38B and in the tables of Fig. 38C. Following the line profiles it appears evident the high selectivity of the DDI process, as well as the antigen recognition by the relative binders: no cross-talking can be measured in the multiplexing nanoarray.

Also, the unchanged roughness of the thiol SAM carpet at each step of biomolecules incubation indicates that no non-specific binding over the surface occurred, pointing again towards the powerful anti-fouling properties of our TOEG<sub>6</sub> SAM.

In quantitative terms, we can see that the final height increase over the cF9 spots upon loading of 20 nM ECD-Her2 consists of about 4 nm. This value is compatible with the 3.3 nm  $\Delta h$  value extrapolated from the calibration curve of Fig. 34, for the same concentration over a single VHH binder-functionalized surface. Moreover, the  $\Delta h$  values corresponding to the same concentration of uPA and ECD-Her2 (20 nM) are of 2.7 nm and 4 nm respectively. This can be explained taking into account the different dimensions of the two proteins (53 kDa uPA and 72 kDa ECD-Her2).

The high selectivity of the binding of the two Ab-Ag pairs working in parallel is then a promising result that ensures the multiplexing nanoarray implementation in real conditions.

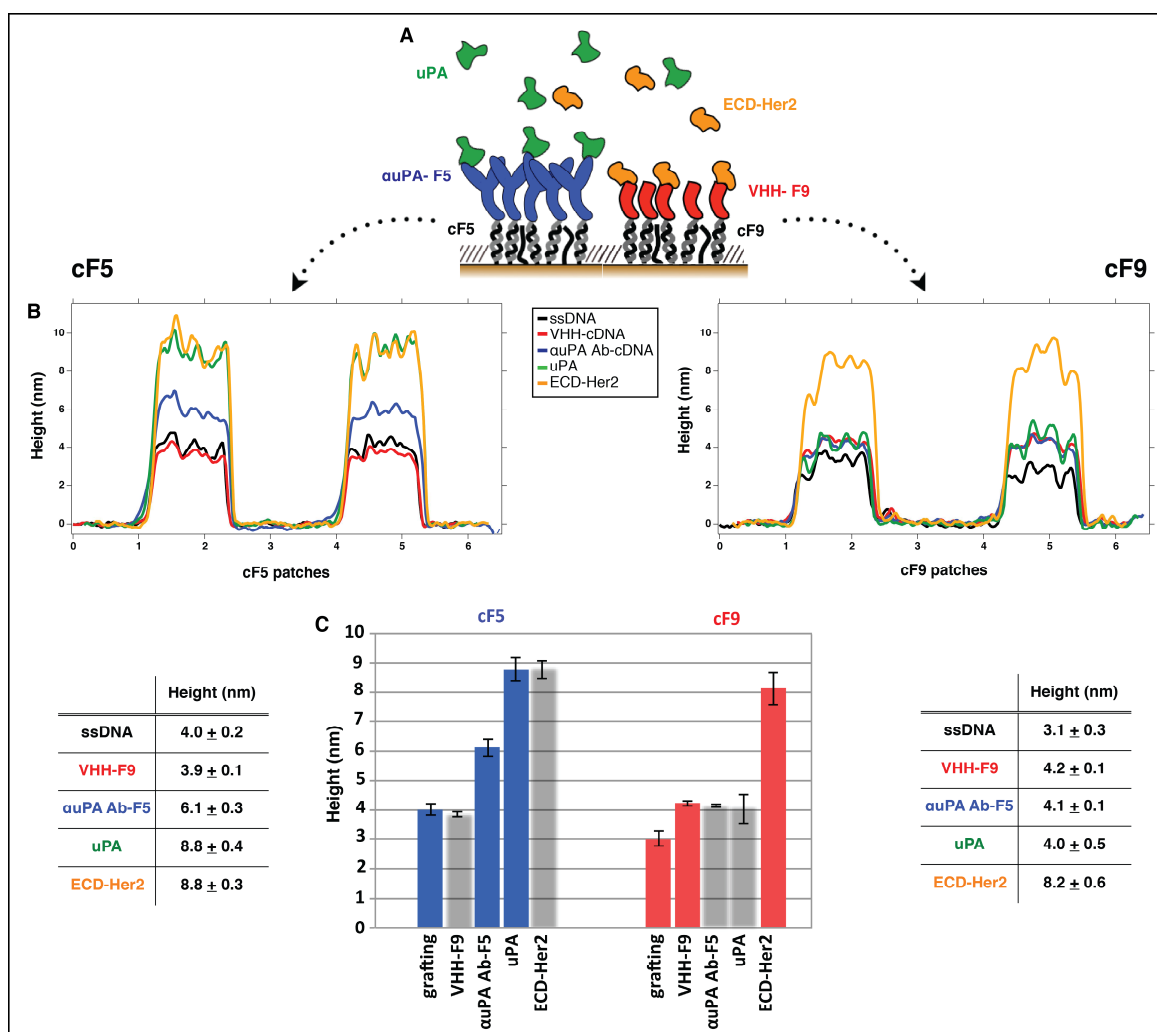


**Fig. 38** Multiplexed detection of two different biomarkers (ECD-Her2 and uPA) on the same surface. (A) Schematic representation of the DDI immobilization of the binders on the DNA-based biosensor and the subsequent detection of the antigens. Height variations of the two separated sets of DNA nanopatches (cF5 and cF9) after each step of incubation of biomolecules (the two different conjugates  $\alpha$ uPA Ab-F5 and VHH EM1-F9) and then the two different biomarkers ECD-Her2 and uPA 20 nM) are visualized by topographic profiles (B) and by histograms (C); Average and Standard Deviation

height values (n=4) are reported on the tables. Grey columns correspond to controls (no expected height increase).

## 5.6 FLUORESCENCE EXPERIMENTS

So far we have demonstrated that our nanoarrays work in a sensitive and antigen-specific manner, with the clear advantage over the standard ELISA platforms to use small volumes and, more importantly, to require only one binder per antigen. In order to perform an additional validation of our nanoarray, and convince about the selectivity for the specific antigen, we compared the single protein-binder topographic measurements approach and the conventional nanoarray-based sandwich approach with fluorescent readout. The goal is to label the nanostructures with a fluorescent molecule as unequivocal proof of the presence of the target bound on the surface.

Moreover we like to demonstrate that a fluorescence-integrated sandwich nanoarray allows performing epitope binning of the binders by analysing the pattern of simultaneous or competitive action of different couples of binders.

### 5.6.1 Validation of nanoarray topographic measurements

As a first approach, we used an “indirect” sandwich configuration (Fig. 39A), more similar to classical ELISA setups. We first immobilized the Abs on the surface and, after ECD-Her2 capture, we added another Ab specific for a further independent ECD-Her2 epitope. The fluorescence signal was obtained using a fluorescently-labeled secondary  $\alpha$ -mouse Ab. From Fig. 39 it is possible to perceive the very good matching between topographic and fluorescence data in this “indirect” nano-sandwich approach.

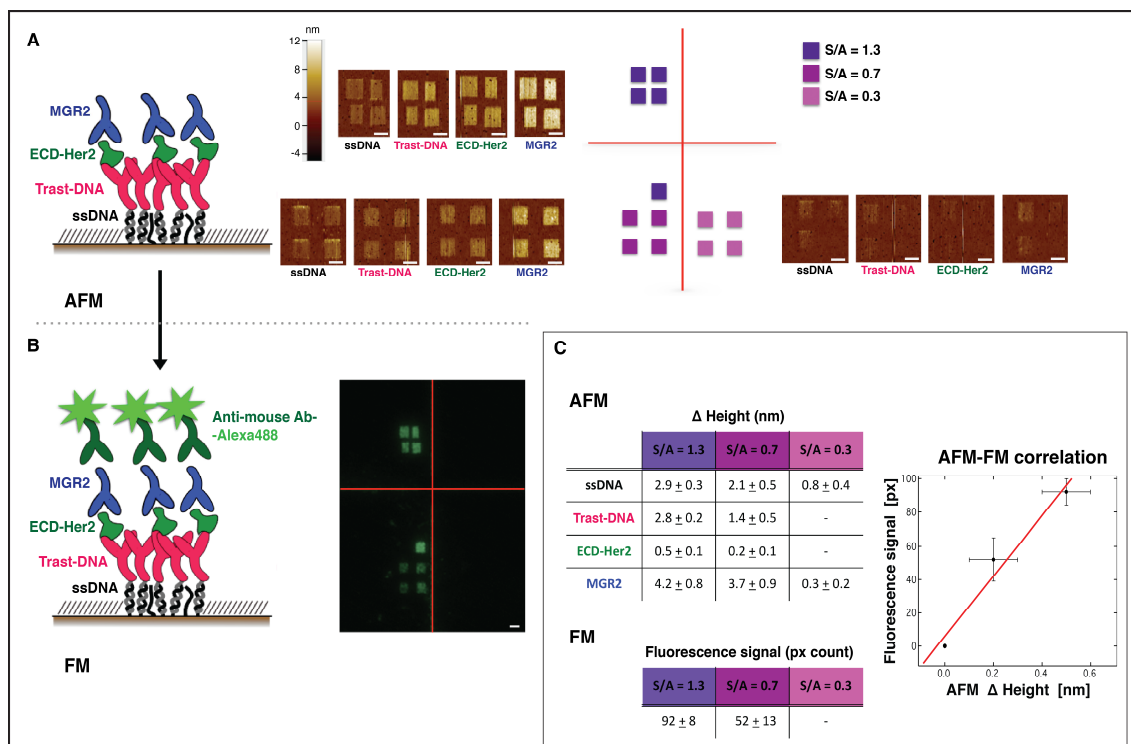


**Fig. 39** Fluorescent visualization of ECD-Her2 captured by the nanoarray. (A) Schematic representation of molecular nanoassembly on the gold surface together with AFM images of the patches at each step of incubation (sequentially: ssDNA, Trastuzumab-DNA conjugate, 200 pM ECD-Her2 and MGR2) at different densities of grafted ssDNA (indicated with different colors, see text). Scale bar 2  $\mu$ m. (B) Fluorescent image of the patches described in (A) after the incubation with anti-mouse Ab labeled with the fluorophore Alexa488. Scale bar 2  $\mu$ m. (C) Height increase values recorded with AFM topographic analysis after each incubation step on the patches and fluorescence values intensity measured as pixel counts are reported in the two tables; fluorescence-AFM topography correlation plot (number of independent patches: 4 for each grafted ssDNA density).

The successive incubation steps were: i) ssDNA; ii) Trastuzumab-DNA conjugate; iii) ECD-Her2; iv) MGR2; v) secondary  $\alpha$ -mouse fluorescent Ab. Notably we confirmed, by means of fluorescence measurements, that even a low topographic height increase (0.2 - 0.5 nm) corresponds to a measurable fluorescent signal, validating the occurrence of binding of very low target concentrations (200 pM). Moreover, as demonstrated by the values reported on the tables and in the AFM-fluorescence correlation graph of Fig. 39C, the fluorescence signal is linearly scaling with the topographic signal and with the density of the ssDNA grafted on the surface, which in turn correlates with the binder density and therefore the total amount of captured target molecules. This validates the quantitative



analysis performed through topographic measurements across the nanopatches of the nanoarray, that anyhow will be carried on without this fluorescent additional tool, confirming that our single-binder assay retains all the potentiality of ELISA with the great advantage of simplicity, cost, efficiency and avoiding the possible artifacts of the fluorescent readout.

### 5.6.2 “Epitope mapping” studies

In addition, the fluorescence-integrated sandwich-nanoarray setup might be useful to obtain important information about protein epitopes recognized by the different binders. For that we used the same “indirect” approach described before, but also a simplified “direct” sandwich approach by exploiting the easy functionalization of the VHH EM1: as a first binder we used a mouse/humanized Ab while the second one was chosen to be the GFP-conjugated VHH. The two configurations are reported in the cartoons of Fig. 40 together with fluorescence images relative to different combinations of binders in the sandwich.

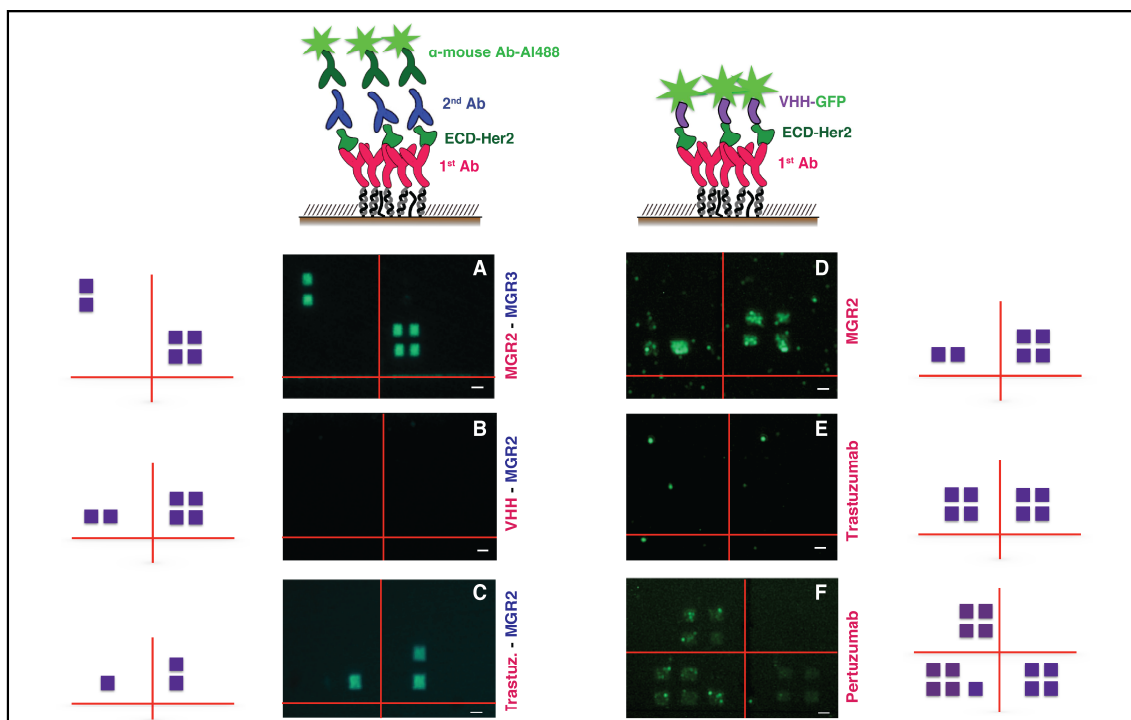


**Fig. 40** Fluorescence images obtained with different combinations of Ab/VHH “sandwich” assay. For images related to the “indirect” configuration (A, B and C) the first Ab of the “sandwich” is indicated in purple and the second in blue; for the “direct” configuration (D, E and F) the first Ab of the “sandwich” is indicated in purple. Next to each fluorescence image the schematic representation of the patches position (violet squares) is reported. Scale bar 2  $\mu\text{m}$ .

We noticed that the fluorescence signal coming from the secondary antibody is generally sharper with respect to the GFP fluorescent signal on the VHH. This could be related to the different fluorescence quantum yield, to the amplification effect due to the secondary Ab, and also to the different dimensions of the two systems, being the VHH four times shorter than Abs and therefore closer to the gold surface, which could partially quench the fluorescence signal.

That given, we used the VHH-related “direct” configuration (Fig. 40D-F) to test its relative epitope on ECD-Her2 recognition. While a fluorescence signal was visible when coupled to MGR2 (Fig. 40D) and Pertuzumab (Fig. 40F), no fluorescence was observable when coupled to Trastuzumab (Fig. 40E). This fact indicated that VHH EM1 and Trastuzumab bind on close/overlapping epitopes and that these are totally independent from the one recognized by Pertuzumab, as reported in the literature [41]. Concerning MGR2, whose epitope has not been mapped yet, our preliminary experiments indicate a simultaneous binding with the VHH and therefore a non cross-reactivity with it. Translating results of Fig. 40D and 40E, we could also conclude that MGR2 and Trastuzumab recognize different epitopes. This is confirmed by result obtained with the “indirect configuration” (Fig. 40C) where we observed the presence of the fluorescence signal in correspondence of the concomitant binding of MGR2 and Trastuzumab proving that the MGR2-functionalized nanoarray is suitable for monitoring the response to therapeutic treatment with this humanized Ab.

With the “indirect assay” we also confirmed the simultaneous binding of MGR2 and MGR3 (Fig. 40A). Data in Fig. 40B relative to the sandwich binding of MGR2 and VHH are apparently contradicting data of Fig. 40D, in which the same couple of binders is used but just in the reverse order. This could be explained by the fact that due to the small dimensions of nanobody, the Ab accessibility to the analyte would be limited as consequence of the proximity to the surface (Fig. 41).

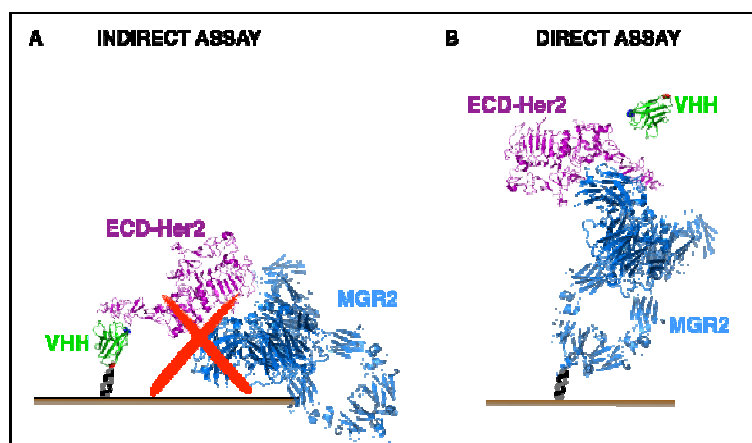


**Fig. 41** Schematic representation of the two different likely configurations of the simultaneous binding of MGR2 and VHH on ECD-Her2.

Combining the evidences of both direct and indirect configuration with these two binders we can however assume that the binding sites of VHH EM1 and MGR2 on ECD-Her2 are most likely very close.

The characterization of the epitope recognized by the binders employed in the nanoarray is also crucial to identify the best molecule capable to discriminate the soluble Her2 variant associated with pro-oncogenic activity, by identifying the specific neoepitope generated upon proteolytic cleavage (the primary cleavage site of Her2 has been located at amino acid position 647–648 and a minor cleavage site has been located at amino acid position 644–645 [33]) and hence improving the specificity of a serum Her2 assay. The evidences obtained up to now with our nanoarray fluorescence approach are not sufficient to prove this specificity. However, we plan to exploit *in silico* engineering of the nanobodies to search for higher affinity binders highly specific only for the cleaved form of Her2, to overcome the limits of the current FDA-approved serum Her2 immunoassay. Moreover such kind of binder will also help to discriminate the fraction of ECD-Her2 related to the Her2-expressing exosomes, another important class of potential biomarkers for Her2-positive breast cancer, whose role needs further elucidation.

These experiments demonstrated that nanografting-based nanoarrays, beyond their potentiality as detection tool, can serve as an alternative approach, complementary to more conventional methods, for identifying the molecular determinants of antibody-antigen recognition.

## **6. APTAMERS: A PRELIMINARY STUDY TO ASSESS ITS FEASIBILITY AS INNOVATIVE NANOARRAY BINDERS <sup>2</sup>**

To increase the nanoarray assay sensitivity, in this part of the study, we tested other high affinity protein binders, the nucleic acid aptamers, to exploit them as active recognition elements of miniaturized DNA-based biosensors.

As a proof of principle, in this study we used an extensively investigated aptamer for thrombin (THR) [121] that shows a well-characterized structure and binding properties ( $K_D = 50$  nM), confirmed by several studies [123,127]. We modified aptamers with a DNA tag

---

<sup>2</sup> “Miniaturized Aptamer-based Assays for Protein Detection” A. Bosco, E. Ambrosetti, J. Mavri, P. Capaldo, L. Casalis. *Chemosensors*. 2016; 4:18.

(cDNA), meant to hybridize to micron-sized surface-grafted complementary DNA monolayers, to create the desired functional areas. We carefully optimized the immobilization strategy to implement DNA-modified aptamers onto the DNA-based miniaturized AFM nanoarrays. As already explained in the experiments related to antibodies/nanobody functionalized nanoarray, this sensor platform has been designed and developed to allow for the sensitive detection of biomolecules in small sample volumes.

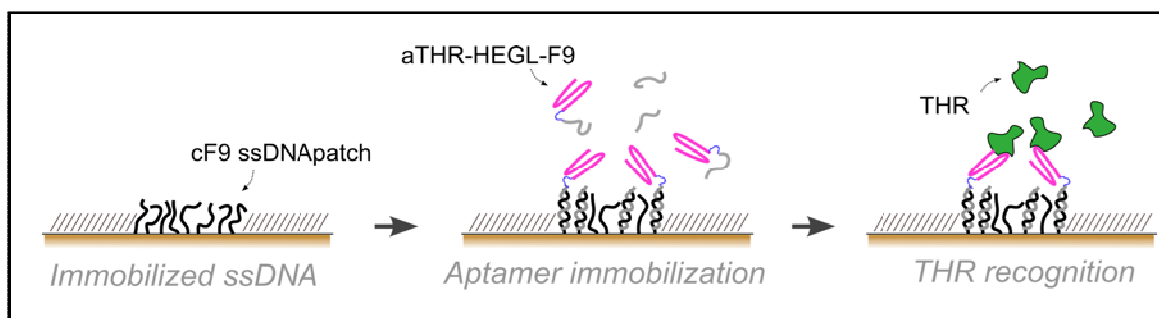


**Fig. 42** Cartoon representing the DDI strategy to immobilize an aptamer on the micron-sized DNA-based biosensor.

By AFM nanografting we confined nanospots of thiol-modified single-stranded DNA monolayers inside a bio-repellent, self-assembled monolayer (SAM) of oligoethyleneglycol-terminated alkanethiols. The density of the DNA-confined SAM can be tuned via nanografting, and adjusted to the steric requirements of this specific biorecognition elements. On such active DNA nanospots, the aptamer-DNA conjugate is then loaded through Watson-Crick base-pairing, in a process known as DNA-directed immobilization.

Two THR-binding constructs were proposed in this regard: a simple design consisting of the aptamer region on the 5' side, extending with the immobilization region complementary to the DNA grafted monolayer on the 3' side (Fig. 43A); a second design similar to the first one, but containing a hexaethylenglycol-spacer (HEGL) between the two regions to improve the functionality of aptamer binding site (Fig. 43B).

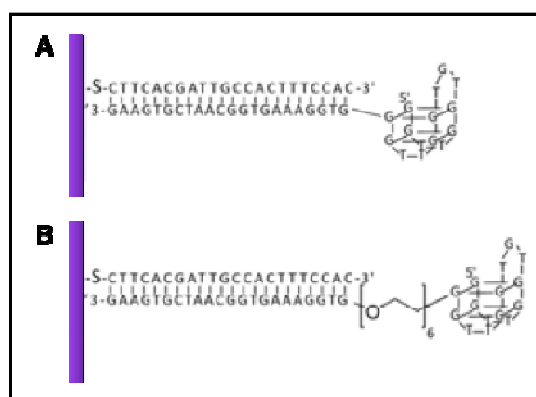


**Fig. 43** Thrombin aptamers sequences, with (A) and without (B) hexaethylenglycol-spacer, hybridized to the complementary ssDNA on the surface.

As stated in several works, the use of polyethyleneglycol groups can significantly improve biorecognition sensitivity by reducing nonspecific interactions and steric hindrance effects [124,125]. In both cases the surface linking oligo sequence (with an alkanethiol linker to bind to the gold surface), and the complementary one on the aptamer side, were carefully selected to have minimal influence on the protein binding—aptamer region in order to avoid possible interferences during aptamer immobilization and then on the aptamer binding interaction with THR.

## 6.1 PRELIMINARY AFFINITY CHARACTERIZATION OF THE DNA-APTAMER CONSTRUCT

All of the experiments were carried out using a buffer (THR buffer) that folds the aptamer in the functional conformation for the recognition of the antigen. To this aim, preliminary tests were carried out to check that both the affinity of the DNA-aptamer construct for the surface immobilized complementary strand and the one for the ligand were preserved. In this regard an estimation of hybridization affinity between the thiolated linker and aptamer construct was first performed *in silico*. According to UNAFold analysis, the calculated  $K_D$  value of cF9-F9aTHR binding in bulk conditions resulted to be in the order of magnitude of attomolar, much lower than the  $K_D$  value obtained for F9 (see Materials and Method section) binding to the aptamer region alone (6.5  $\mu\text{M}$ ), therefore, suggesting that the immobilization of the DNA-aptamer constructs is occurring essentially through the cF9-F9 pairing. Using EMSA, it has been previously verified that both DNA-aptamer constructs were able to bind thrombin. However, F9-HEGL-aTHR was observed to bind more efficiently to THR compared to F9aTHR, so in the following experiments we decided to focus on the first construct.

Binding affinity analysis was then performed on surface immobilized aptamers via SPR, following the DNA-aptamer immobilization procedure described in the previous session. A wide THR concentration range (0.8–200 nM) was screened with Biacore. The signal response is proportional to the THR concentration (Figure X); the mostly straight binding lines in the association phase obtained with analyte injections up to 12.5 nM show a possible mass transfer contribution. These curves do not display a sufficient curvature to perform kinetic analysis. Although an equilibrium state has not been reached for all the concentrations tested, we recorded the binding level at the end of the association phase. These values, plotted against THR concentration, were fitted with a single site interaction model. This “non-steady-state”

analysis implies an underestimation of the binding affinity [126,127]. Therefore, we can conclude from the SPR data that the  $K_D$  is in the range 10–100 nM, in agreement with the value reported in the literature for the aptamer-THR binding ( $K_D = 50$  nM) (Figure 44).

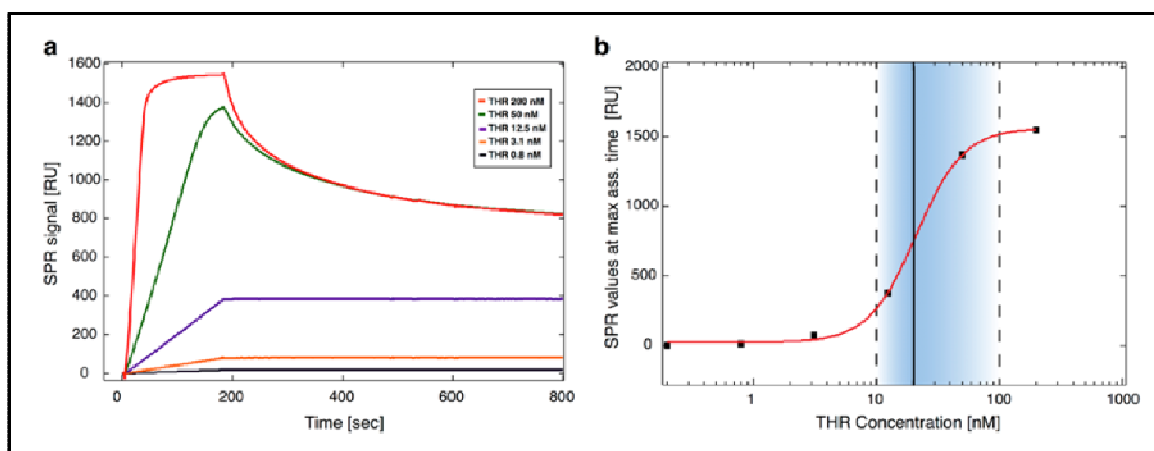


**Fig. 44** SPR characterization: (a) sensograms of different THR concentrations (0.8–200 nM); and (b) binding affinity analysis; SPR responses at the end of the association phase are plotted against THR concentration and fitted (red line) to a single site interaction model ( $[RU] = RU_{max} - (1/(1 + K_D/[A]))$ ) the black vertical line indicates the value of  $K_D$  found from the RU model; the light-blue area is the range of possible  $K_D$  values (see text).

## 6.2 AFM MECHANICAL SENSING ON NANOSTRUCTURED ASSAYS

The AFM nanoarray platform was built starting from cF9 DNA nanografting, on which we loaded via DDI the F9-HEGL-aTHR aptamer construct (Figure 45 left, top image).

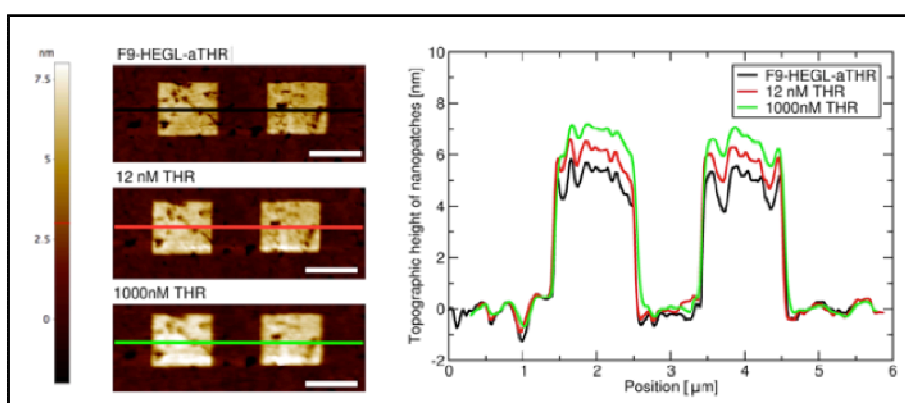


**Fig. 45** Images of the nanopatches on the gold surface (left, scale bars 1  $\mu\text{m}$ ) and their topographic profiles (right). Black: F9-HEGL-aTHR aptamer immobilization; red: THR 12 nM incubation; and green: THR 1000 nM incubation.

By using AFM topographic imaging, we monitored height profile changes over DNA-aptamers loaded by DDI on cF9 nanografted arrays (Fig. 45 left, upper patches; right, black profile) vs. different THR concentrations in the binding buffer (Fig. 45 left, mid and lower images; Figure

46 right, red and green profiles correspond to 12 nM and 1000 nM THR, respectively), due to the conformation change of the aptamer upon binding the ligand. In all these steps the TOEG SAM embedding the patches is used as a reference level to monitor topographic height changes. Differential height changes are shown in Figure 46a. By plotting height change vs. concentration, we extracted an effective dissociation constant for this system in the range 10–100 nM, a value that is in good agreement both with literature and with the SPR results obtained using the same molecular construct. As one can clearly see in Figure 46, the data are affected by significantly large errors that could be attributed to the fact that when the ligand binds to the aptamer, it folds to a more compact shape.

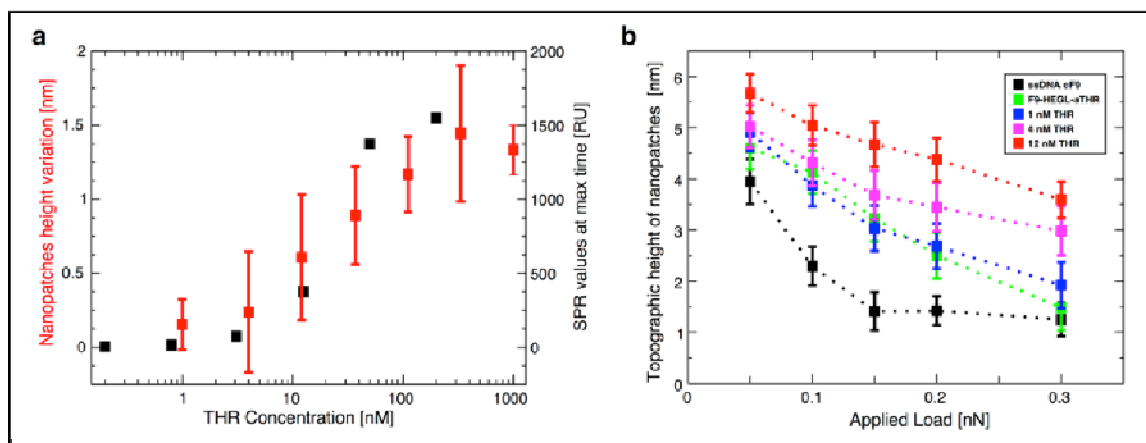


**Fig. 46** (a) Comparison of binding curves obtained from the height variation measured with the AFM on DNA nanopatches (left) and SPR data (right) vs. THR concentration; and (b) evaluation of the static compressibility on DNA nanopatches at low concentrations of THR.

This results in a reduced AFM differential height, since the height increase due to protein uptake is counterbalanced by the height decrease due to a change in binder conformation. Additionally, the softness of the nanopatches contributes to such large errors: the coupling of the aptamer to the nucleic acid linker, in fact, increases the compressibility of the entire nanopatch, giving more variability while measuring AFM height variation [102]. We then performed a so-called “compressibility analysis”: we monitored the softness of the patches, exposed to different THR concentrations, by imaging progressively the patches at increased tip load. The variation of (absolute) patch height vs. tip load for the bare DNA patches, the patches loaded with the aptamer constructs and then the last ones exposed to different THR concentrations are shown in Figure 46b. As shown in Figure 46b, while applying only 200 pN, nanopatches can be compressed up to 40% of the height measured at minimum force (about 50 pN below which the AFM tip loss its contact with the surface). However, from such analysis we can conclude that the higher the THR concentration, the stiffer the patch

towards tip compression. The increase of nanopatch stiffness upon THR immobilization is due to the high compactness of globular proteins (as THR), much higher than for nucleic acids at the ionic strength used for the experiments. A stiffness change of about 30%–35% upon 4 nM THR binding can, in fact, be estimated from the compressibility experiments, at variance with the patch height that stays almost constant.

Therefore we demonstrated the feasibility of aptamer as potential recognition molecules suitable for the nanoarray; the nanoarray platform has to be carefully optimized in both in the immobilization of the molecules by adding of a short oligo via a polyethyleneglycol linker and by tuning aptamer surface, and in the AFM-detection strategy, due to the peculiar features of this oligonucleotide sequences that undergo to conformational rearrangement to bind the ligands.

We obtained a value of  $K_D$  in good agreement with the available literature for in bulk studies, demonstrating that the immobilization of aptamer via DDI on the surface preserves its functionality and allows successful thrombin detection.

Once selected a Her2 specific aptamer a study of the nanoarray capability with respect to antibody/nanobody-functionalized AFM assay will be performed. However the evidences obtained by the different experiments presented in this work can lead to a preliminary consideration yet: in the AFM approach nanobodies seem to be the most promising binders not only for their sensitivity but mainly in terms of robustness of the assay and readout results. On the contrary aptamers would be preferred in some alternative surface-based miniaturized platforms (i.e. electrochemical impedance spectroscopy devices) characterized by a different readout system that fully exploits some peculiar features of this kind of molecules.

## **7. STUDY OF THE POTENTIAL VALUE OF RELEASED ECD- Her2 AS INDICATOR OF TUMOR PROGRESSION**

The precise quantification of circulating ECD-Her2 in blood serum and of total Her2 or Her2 homodimers in living cell membranes would help to classify Her2 status and to define the impact of shedded Her2 on prognosis and response to anti-Her2 therapies.

However, conflicting results are correlating Her2 gene amplification, protein expression and cleavage of the ECD [30,46,128]; only few studies analyzed simultaneously tissue and serum data, to precisely understand the relationship between dimerization and ECD release at different level of tumor progression and in response to therapy. Clarifying whether the amount of shedded ECD-Her2 predicts tissue Her2 expression status, would validate ECD-



Her2 value in serum screening as complement analysis to tissue testing both in early breast cancer and in metastatic disease.

Since so far the clinical significance of circulating ECD-Her2 remains uncertain, it is a general opinion that this issue deserves further studies in large prospective trials, together with *in vitro* studies to elucidate fundamental aspects of the relationship between dimerization, ECD shedding and its prognostic/therapeutic value.

Therefore to assess the role of shedded ECD-Her2 as tumor biomarker we studied the localization and quantification of Her2 levels in membranes and the correlation of this information with sensitive quantification of ECD-Her2 in cell medium through nanotechnology-based diagnostics.

### **7.1 LOCALIZATION AND QUANTIFICATION OF Her2 ON CELL MEMBRANE**

We performed fluorescent labelling on SKBR3 cells (breast tumor Her2-overexpressing cell line), MCF7 cells (Her2-negative breast tumor cell line) and HEK293 cells (human embryonic kidney cell line) as negative control. We labeled fixed cell with MGR2 as primary antibody specific for ECD-Her2 and a secondary green fluorescent Ab to mark the target membrane protein; we used DAPI labeling of the nucleus for an easier identification of cells. The fluorescence signal has been monitored with epifluorescence inverted microscope.

As visualized in Figure 47 by green fluorescence localized in the plasma membrane, the SKBR3 tumor cell line (A, B, C) shows an higher level of Her2 if compared with both the negative control (D) and the Her2-negative cell line (E); the overexpression in the tumor cell line could be connected to an oligomerization mechanism revealed by the presence of clusters (C – red arrow).

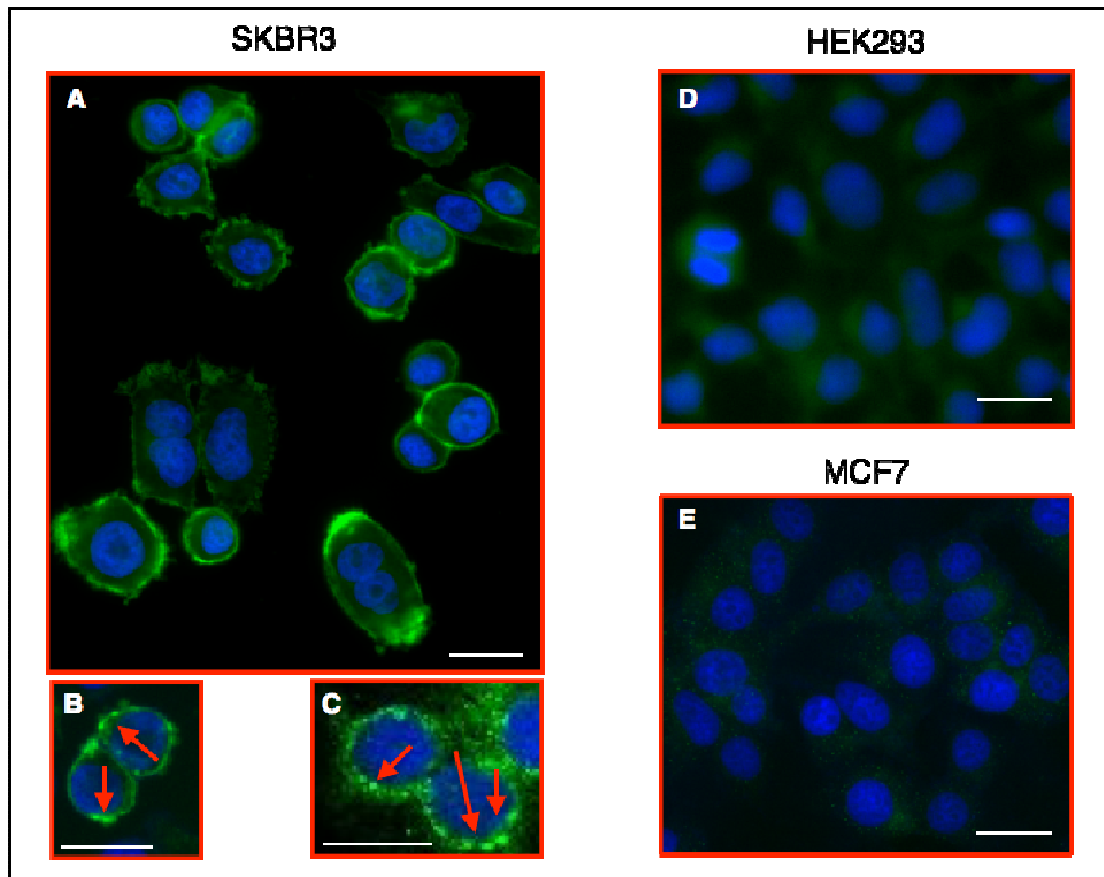


**Fig. 47** Epifluorescence microscopy images of fluorescence labeled SKBR3 (A, B, C), HEK293 (D), and MCF7 (E) cells; ECD-Her2 has been detected by means of MGR2 as primary Ab and secondary  $\alpha$ -mouse-Alexa488 Ab. Scale bars 20  $\mu$ m.

Due to resolution limit of the setup, we expect that precise localization and quantification of the protein of interest being hampered. In order to improve the resolution of fluorescence imaging, we preliminary attempted few localization and co-localization experiments with a commercial STED setup available in the lab of Dr. Ilaria Testa of the KTH in Stockholm. There we performed two series of independent experiments, labeling the ECD-Her2 (Fig. 48A, B, C) and the ICD-Her2 (Fig. 48D, E, F), respectively, by means of an Oregon Green488-labeled secondary Ab targeting MGR2 in one case and an  $\alpha$ -ICD Ab in the other. Results have been collected for SKBR3 and HEK293 cell lines, as in epifluorescence experiments. As Her2-negative cell line we used in this case a triple negative breast tumor cell line (MDA-MB-231).

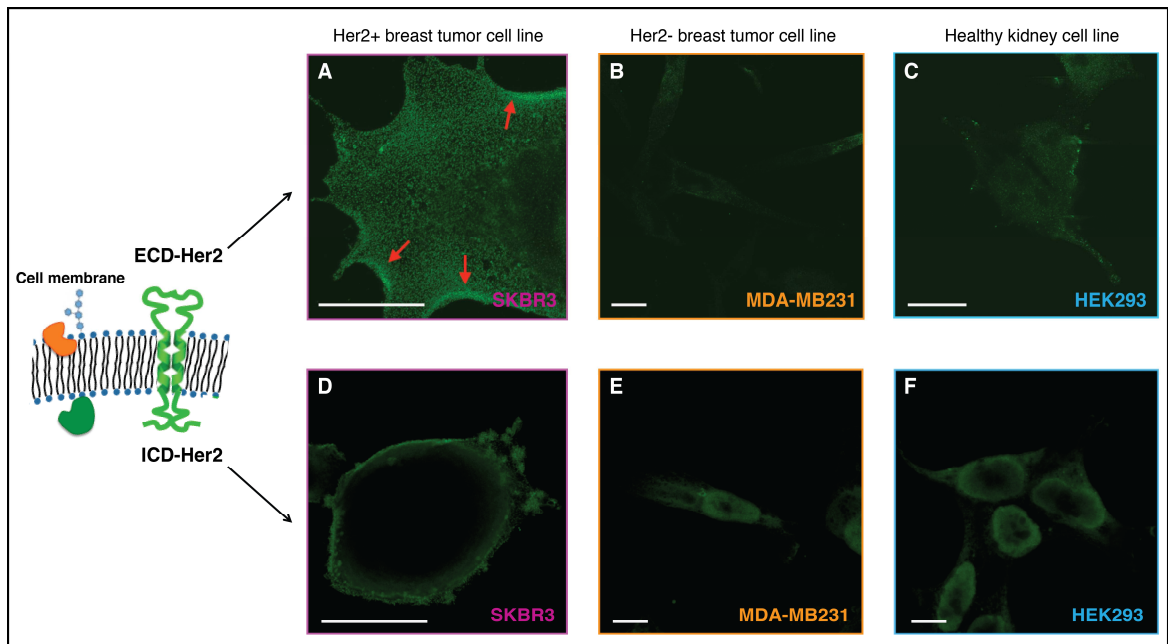


**Fig. 48** STED microscopy images of fluorescence labeled SKBR3 (A, D) MDA-MB-231 (B, E) and HEK293 (C, F); cells have been labeled to visualize ECD-Her2 (A, B, C) and ICD-Her2 (D, E, F). Scale bars 10  $\mu\text{m}$ .

Concerning ECD-Her2 we confirmed the previous results: SKBR3 cells exhibits higher receptor level (Fig. 48A) with respect the control cell lines (Fig. 48B, C). The increased resolution obtained with STED microscopy (below 50 nm) allowed also distinguishing the presence of Her2 clusters localized in the cytoplasmic membrane (Fig. 48A – red arrow). Analyzing the ICD-Her2 signal instead, we can surprisingly notice that the different cell lines seems to vary not much for the expression level but rather for the localization of the intracellular receptor domain. In SKBR3 cells the ICD-Her2, as the ECD-Her2, is visualized on the cytoplasmic membrane (Fig. 48D), instead on MDA-MB-231 and HEK293 cells it is strongly expressed into the nucleus (Fig. 48E, F). Although it is commonly known that tyrosine kinase receptors, such as the Her family, function as signaling initiators on the cell membrane, this evidence seems to be in agreement with some works present in literature which demonstrate that receptors or fragments of them travel from the plasma membrane to the nucleus by different mechanisms and may act as transcription factor in the nucleus [129]. Moreover it has been demonstrated that the nuclear ICD-Her2 targets several gene promoters to mediate gene expression. Since Her2 lacks any known structural signatures required for DNA association, it is likely that Her2 may associate to AT-rich DNA sequences and with other DNA binding nuclear factors, as histone 3 isoform [130]. Since the different scenario in SKBR3 cell line and the negative control ones it can be speculated that Her2 overexpressing cells promote the molecular cascades strictly connected the membrane

dimerization of the receptors, the proteolytic release of ECD-Her2 and the N-terminally truncated Her2 increase of the tyrosine kinase activity, that activates the downstream proliferation signalling pathways rising the oncogenic potential.

On the contrary Her2-negative cells show a genomic function of ICD-Her2 and a possible alternative activation of gene regulation mechanisms, responsible of the different cell phenotype or the different breast cancer subtype. This explanation requires additional measurements to be fully proved.

## 7.2 CO-LOCALIZATION OF INTRACELLULAR DOMAIN (ICD)-Her2 AND ADAM10 ON SKBR3 CELL MEMBRANES

Since the metalloprotease ADAM10 has been identified as the main ECD-Her2 sheddase, we studied the co-localization of the ICD-Her2 and this protease in the SKBR3 cell line (Fig. 49).

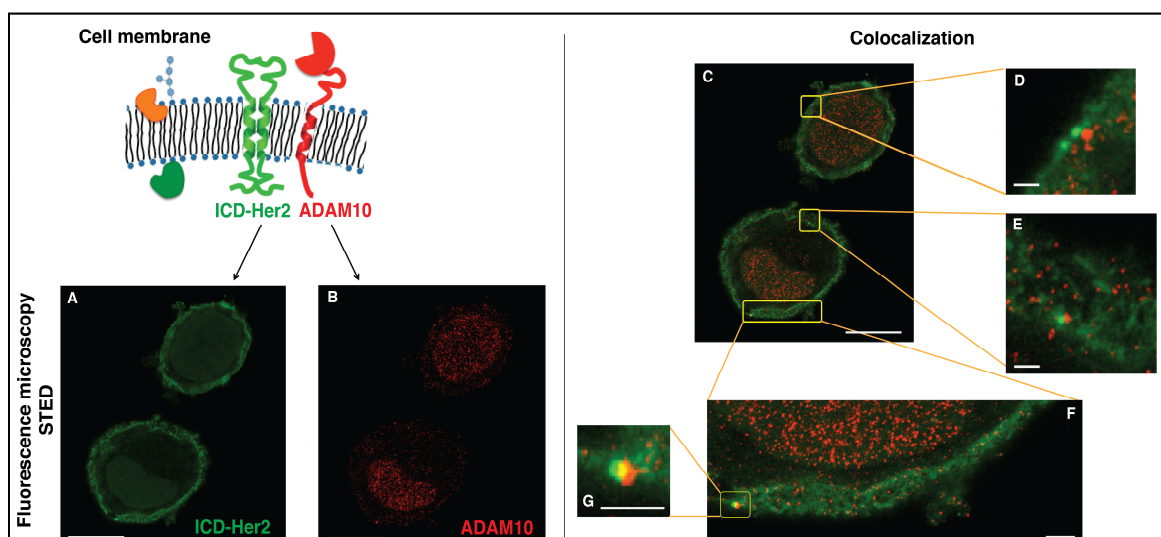


**Fig. 49** STED microscopy images of fluorescence labeled SKBR3; cells have been labeled to visualize ICD-Her2 by means of green fluorescence signal (A) and ADAM10 by means of red fluorescence signal (B). The super-imposition of the signals (C), and in particular the magnification of some region of interest (D, E, F, G) visualizes the co-localization of Her2 and ADAM10. Scale bars: (A, B, C) 10  $\mu\text{m}$  – (D, E, F, G) 1  $\mu\text{m}$ .

As shown in Fig. 49 by means of high resolution STED microscopy we were able to identify some regions in the cell membrane in which ICD-Her2 (labeled with green fluorescent dye) and ADAM10 (labeled with red fluorescent dye) co-localize. This first experimental evidence represents only a preliminary result in the global understanding of the correlation between Her2 overexpression status and the cleavage of its extracellular domain. Exploiting another super-resolution microscopy approach, called reversible saturable optical fluorescence transition (RESOLFT) [131], also available in the lab of Dr. Ilaria Testa, that allows an

extremely precise (lateral resolution between 20 and 50 nm) simultaneous localization of biomolecules in cells, we plan as a next step to perform the quantitative study of the co-localized receptor-protease couples with the different levels of cell membrane receptor expression.

### 7.3 CORRELATION BETWEEN ECD-Her2 LEVELS IN CELL MEDIUM AND Her2 TUMOR STATUS

The relationship of Her2 overexpression status with ECD released by means of the shedding process has been preliminary studied in order to correlate fluorescence measurements described in paragraph 7.1 with the amount of ECD present in the medium of cell cultures. The quantitative detection of the target has been performed by the previously described AFM-based nanoarray, functionalized with Trastuzumab conjugate. Fig. 50 reports the results related to the detection of ECD-Her2 released in the culture medium of two different cell lines: SKBR3, that overexpresses Her2, and HEK293, that shows a normal level of the receptor. Notably a height increase has been detected only when incubated with the SKBR3 cell medium, instead no increment has been observed for the negative control. This evidence withstands the hypothesis that the overexpression of Her2 is directly correlated to an increased dimerization and shedding, and hence to a higher amount of released ECD-Her2, supporting the prognostic significance of this circulating biomarker.

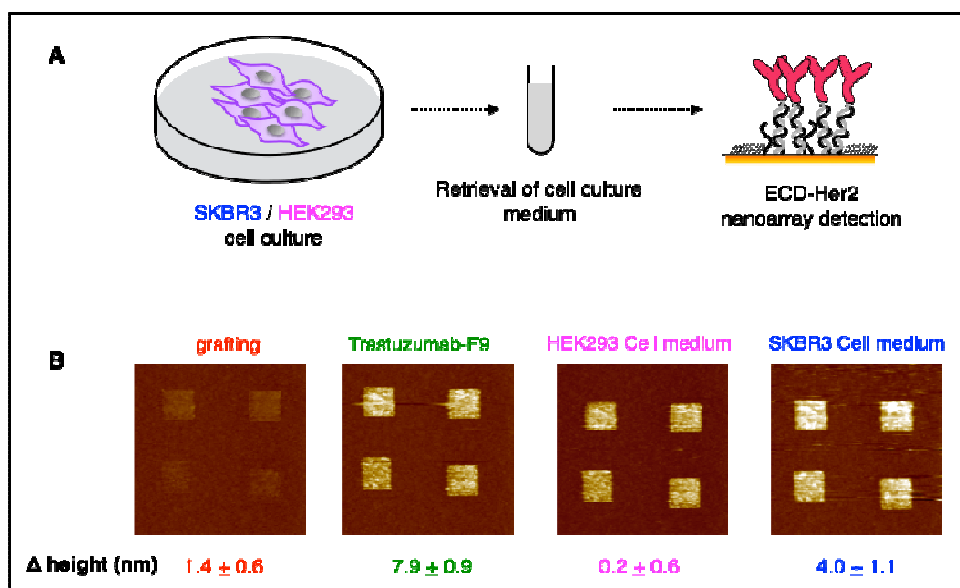


**Fig. 50** Nanoarray detection of ECD-Her2 on cell culture medium. (A) Schematic representation of the assay. (B) Images of the nanopatches on the gold surface with relative average and standard deviation values of the height measured across the nanopatches at each step of the experiment (grafting of ssDNA; hybridization of Trastuzumab-DNA conjugate; HEK293 cell medium incubation;

SKBR3 cell medium incubation).

## **8. STUDY OF Her2 STATUS IN EXOSOME-DRIVEN TUMOR CELL COMMUNICATION**

Quantitative fluorescence microscopy studies have demonstrated that clusters of Her2 co-localize with lipid rafts on Her2 overexpressing SKBR3 breast cancer cells [52,53]. Lipid rafts are sub-domains of the cell membrane enriched in cholesterol and glycosphingolipids, involved in important cellular processes, such as proteins traffic, cell polarity control and cell signaling alteration. Therefore rafts are considered crucial regulators of mechanism as cell fate, growth, adhesion and migration, all processes which are disregulated in cancer [49]. From the studies in ref. 52, 53, it has then been proposed that lipid rafts influence the association properties and the biological function of Her2. This evidence introduces two novel research routes towards:

- understanding how rafts regulate Her2 dimerization and hence if/how rafts dissociation decreases Her2 activation. This could be useful to hypothesize an alternative therapeutic approach to Her2-positive breast tumor, which would involve the altering of rafts physiology;□
- clarifying the relationship between rafts-mediated exosomes formation and Her2 integration on them. Her2 dimerization in breast cancer cells seems to takes place in the specific rafts subfamily caveolae. Moreover it has been demonstrated that a specific caveolae protein Caveolin-1 is strongly expressed in exosomes secreted by tumor cells [56]. Experiments on co-localization of Her2 and raft-related Caveolin-1 may indicate its possible involvement in the biogenesis of tumor cells secreted exosomes and elucidate the significance of Her2 status in exosome-driven tumor cell communication as crucial mechanism in tumor spreading and metastasis occurrence.

Towards this goal we used fluorescence microscopy to co-localize Her2 with other molecular markers of lipid rafts and specifically of caveolae; we also isolated exosomes in the medium in order to characterize the presence of Her2 in them through AFM-based nanoarray.

### **8.1 CO-LOCALIZATION OF Her2 AND RAFTS COMPONENTS IN CELL MEMBRANES**

The co-localization of Her2 receptors and rafts components (i.e. GM1 ganglioside, caveolin-1) has been performed exploiting specific markers of rafts molecular constituent, as Cholera

Toxin (subunit B) that binds to GM1, an Ab directed against Caveolin-1. We first labeled GM1 rafts components and simultaneously ECD-Her2 in Her2-positive SKBR3 cell lines and in Her2-negative MCF7 cell lines. The immunofluorescence results are reported in Fig. 51; we observed that SKBR3 cells show higher level of ECD-Her2 (red signal) with respect of the negative control, as already demonstrated the experiments previously discussed. Instead the presence of rafts GM1 (green signal) is comparable in the two cell lines, as expected. Interestingly in Her2 overexpressing cells receptor clusters localize on the same membrane regions in which GM1 is detected, supporting the hypothesis of Her2 preferential localization in lipid rafts.

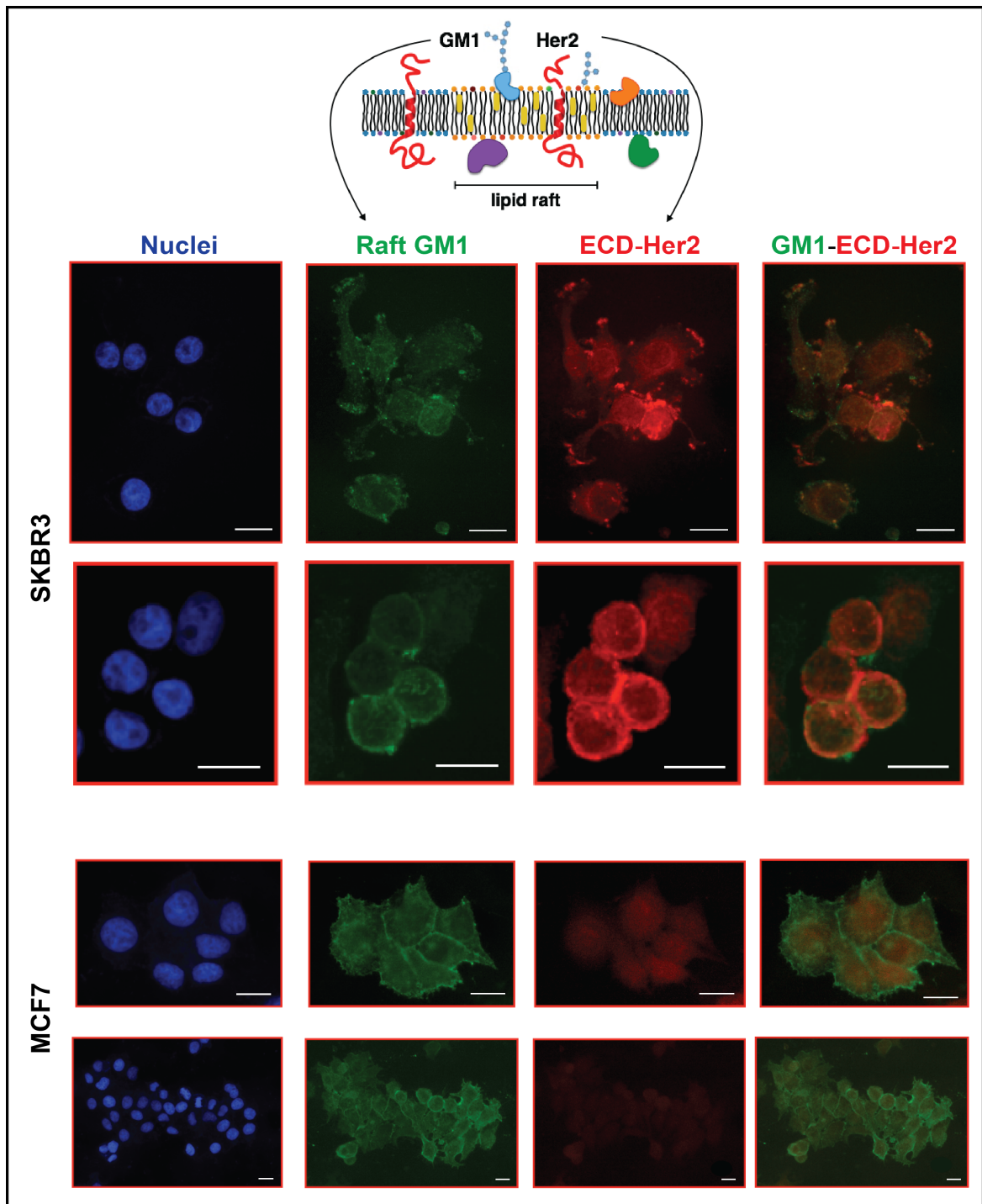


**Fig. 51** Immunostaining of SKBR3 and MCF7 cells; nuclei are labeled with DAPI (blue signal), GM1 with Subunit B of Cholera toxin-FITC (green signal), ECD-Her2 with MGR2 and secondary Ab-Texas Red (red signal). Green and red fluorescence is merged in the last column to display the co-localization of GM1 and ECD-Her2. Scale bars 20  $\mu$ m.

Then we proceeded with the visualization by fluorescence of caveolae, the rafts subfamily in which Her2 dimerization may occur. We labeled caveolin-1 as specific caveolae marker in



SKBR3 and HEK293 cell lines. As shown in Fig. 52 SKBR3 exhibits a higher fluorescence level with respect to HEK293 of caveolin1-related signal, localized, as expected, in the membrane. This preliminary result is in agreement with the hypothesis that caveolae, due to their role in vesicles formation and transport, could be involved in the release of signaling molecules and the spreading in distant tissue and hence be highly expressed in tumor cells [55,56,57,132].

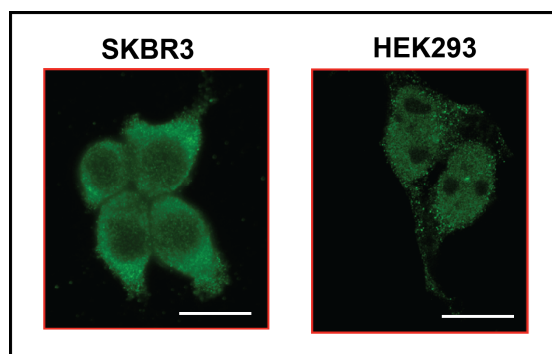


**Fig. 52** Epifluorescence microscopy images of fluorescence labeled SKBR3 and HEK293 cells; Caveolin-1 has been detected by means of primary  $\alpha$ -Cav1 mouse Ab and secondary  $\alpha$ -mouse-Alexa488 Ab. Scale bars 20  $\mu$ m.

Next step will be to perform with the STED setup the simultaneous detection of Caveolin-1 and Her2 receptors in order to verify the co-localization of the two molecules and hence to speculate about rafts-mediated exosome formation and the role of Her2 integration/dimerization on them.

## **8.2 EXOSOMES SPREADING BY Her2-POSITIVE CELLS: A MULTI-INTEGRATED APPROACH FOR THE CHARACTERIZATION AND FOR THE CORRELATION OF Her2 STATUS IN CELL MEMBRANES AND RELEASED ECD-Her2 LEVELS**

Analysis and characterization of exosomes released in SKBR3 cell culture medium have been performed first isolating them with size-exclusion chromatography; qEV size exclusion columns [133] contain a resin with an approximately 75 nm pore size. Proteins and other contaminating molecules smaller than EVs enter the pores of the resin and are delayed in their passage through the column, eluting in later fractions. Depending on the pore size the columns have been primarily optimized for accurate nano-size vesicles, such as exosomes. The different collected fractions have been analyzed in protein (by means of adsorbance spectrophotometer measurements) and exosomes content (by means of preliminary AFM tapping-mode imaging in air, after fixation in 4% paraformaldehyde). No protein contaminants have been detected in all the fractions analyzed (the first five after the void

volume); instead we observed in the first two fractions different sized-nanovesicles that have been statistically analyzed for their dimension in terms of diameter and height (Fig. 53).

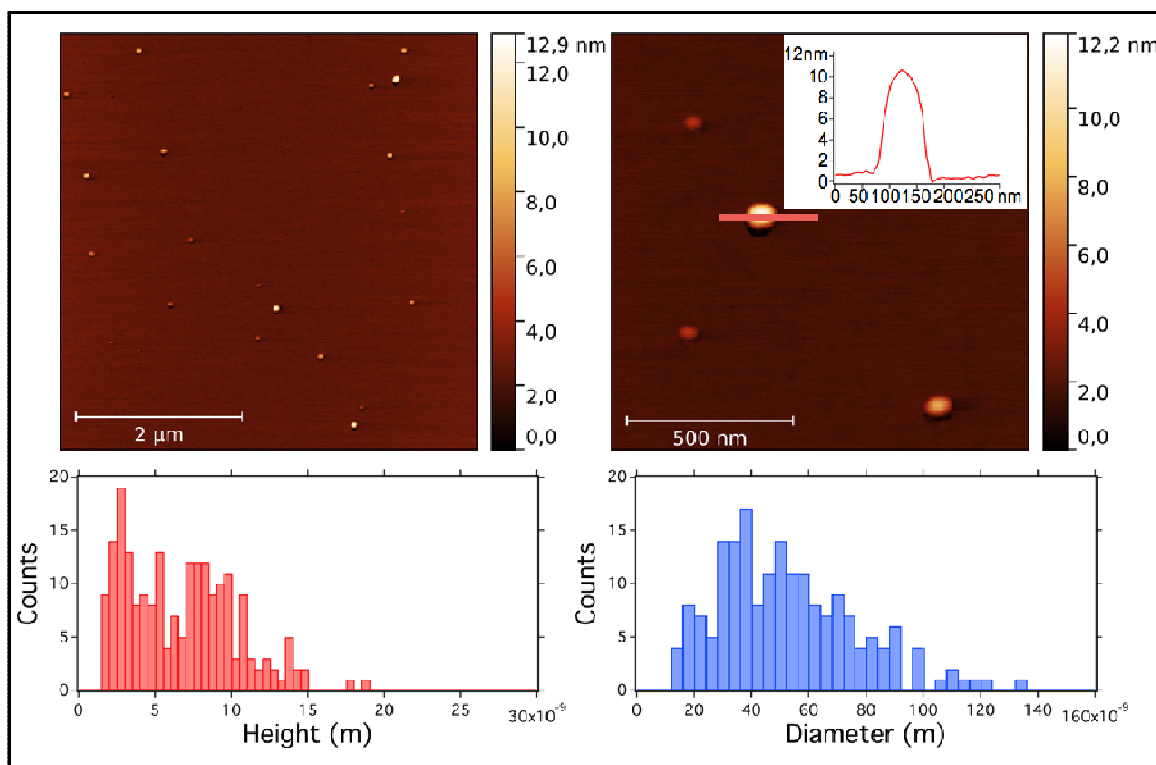


**Fig. 53** AFM images (topography) in air of SKBR3 cell medium derived exosomes deposited on mica substrate and fixed with 4% paraformaldehyde. Histograms show exosomes height and width distribution.

The measurements in air revealed the presence of round particles of diameters ranging from 20-90 nm and height ranging from 4-15 nm. It's important to underline that AFM imaging in air can rather deform the vesicles and determine an underestimation of the height. In fact the absence of a liquid environment determines a “collapse” of the vesicles and an increased amount of adhesion points to the surface; this results in less reliable height information.

The PFA fixation does not significantly changes the diameter and height distributions, only preserving a more roundish shape. The advantage coming from imaging in liquid is that the vesicles are less deformed and the height information therefore more reliable; however this kind of measurements is impaired by the movements of the nanovesicles induced by the interaction with the tip. Moving towards, this imaging approach would require a proper anchoring approach that consists in a proper immobilization of the exosomes on *ad-hoc* produced AFM-based nanoarray surfaces by means, for instance, of the exosome specific membrane tetraspanin CD9 [134]. This methodology ensures not only a stronger anchoring on the surface but also a specific recognition of exosomes, due to the presence of this

constitutive marker. Then the nanovesicles can be characterized in terms of membrane expressed protein components, as Her2 receptors to begin with, targeting them with proper Abs (Fig. 54).

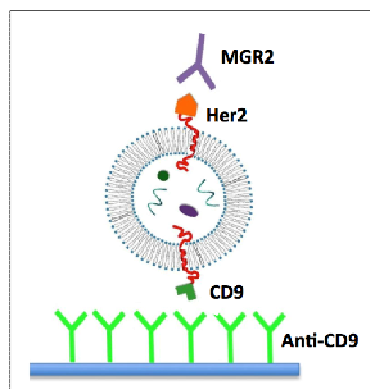


**Fig. 54** Schematic representation of the experimental approach for exosomes immobilization on gold surface and their characterization by means of Abs specific for different membrane receptors.

At present we succeeded in the production of  $\alpha$ -CD9 Ab-DNA conjugates and in their immobilization on the surface via DDI. We are optimizing the functionalized surface conditions in order to perform the exosomes anchoring. Once this molecular characterization will be obtained, in relation to different cell lines, it would be useful to distinguish specific subpopulations and to relate them to the originating cell (tumor versus healthy, Her2-positive versus Her2-negative).

The quantification of the specific subpopulation of nanovesicles, exosomes expressing Her2 on their surface, would help to understand their contribution to the computation of the total amount of ECD-Her2 (the one freely circulating and the one embedded in the vesicle membrane) in serum.

Moreover a multi-integrated approach would be useful to assess the correlation between Her2 overexpression, dimerization, ECD cleavage and exosome-driven tumor spreading, towards a clarification of the prognostic significance of Her2-related circulating biomarkers.

The results of the experiments discussed above can be merged in order to correlate information coming from advanced microscopies (membrane proteins localization), nanotechnology-based diagnostic tools (detection of protein and vesicle biomarkers) and novel super resolution fluorescence microscopies (quantification and co-localization of different biomarkers). An example of the multi-integrated experimental design is described in Fig. 55.

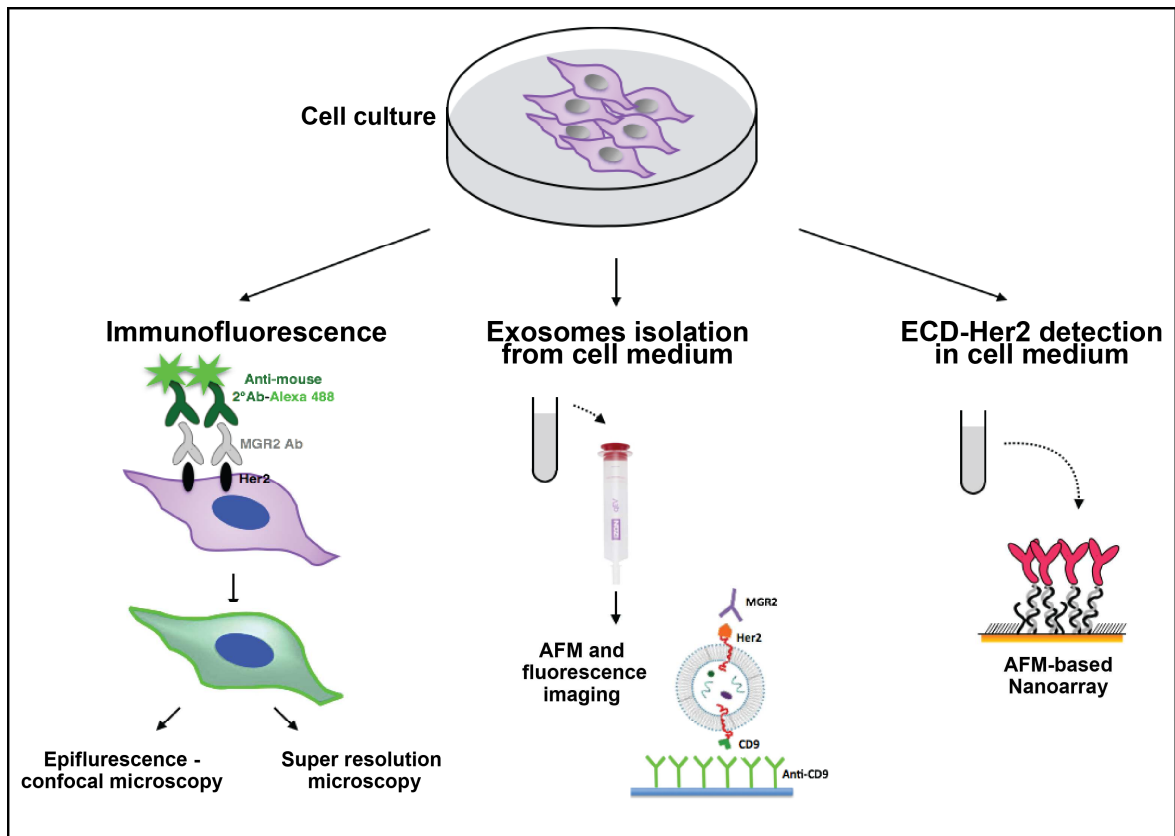


**Fig. 55** Schematic representation of the multi-integrated approach to study the correlation between Her2 overexpression, dimerization, ECD cleavage and exosome-driven tumor spreading.

Towards this direction we already got results related to SKBR3 cells: the Her2 overexpression detected in cell membrane is consistent with the presence of ECD fragment and exosomes released in the medium. The possibility to separate the nanovesicles fraction from the protein content released in the medium will be a crucial tool for the comprehension of how these two different biomarkers contribute to ECD-Her2 significance in diagnosis. A quantitative consideration about the relationship of Her2 status and circulating biomarkers spreading will be performed with the analysis of cell lines with a different Her2 expression signature (i.e. SKBR3 versus MCF7 and HEK293) or with different tumor progression or primary/metastatic nature (i.e. SKBR3 versus MDA-MB-453).

## DISCUSSION

The use of miniaturized devices in liquid biopsy for cancer biomarker detection and therapy monitoring will ultimately improve the outcome of tumor early diagnosis and treatment. Here we trial a nanoarray based on AFM nanolithography, DNA-directed immobilization of protein binders and topographic readout for the detection of cancer-relevant biomarkers circulating in the bloodstream. We focused on the detection of ECD-Her2, optimizing the choice of binders to increase detection sensitivity, even in multiplexing with uPA, to move towards a biomolecular footprint of the disease. We demonstrated that this simple assay has the required sensitivity to be operated in the clinics, allows detection in small volumes of complex matrices, enabling continuous non-invasive therapy monitoring from single blood droplets (few microliters). Moreover, at variance with ELISA, it requires a single binder for each biomarker and is label-free, avoiding false results connected to fluorescence interference susceptibility, overall tremendously reducing diagnostics costs while maintaining high biorecognition specificity and fast readout. A simplified, automatized, cantilever-based readout machine can in fact be conceived for antigen quantification purposes.

In particular we demonstrated that nanoarrays employing panning-selected camelid nanobodies can detect ECD-Her2 up to less than 200 pM, which corresponds to the cut-off value of 15 ng/mL currently used in clinics to discriminate between healthy and pathological status. We showed that the high affinity of nanobodies can be fully exploited by tuning binders surface density: at variance with classical antibodies, for which steric hindrance can promote anti-cooperativity of adjacent binders, higher probe densities are allowed for smaller binders and indeed help improving the overall sensitivity for target identification. We expect that the optimization of the linker length and the *in silico* engineering for boosting the affinity for cognate antigen will enable improving substantially the use of nanobodies as capture molecules and further drop the detection limit.

Our platforms are ready to perform biomarkers detection in real blood serum samples (exploiting our collaboration with the Department of Medical and Biological Sciences - University of Udine and with the Department of Experimental Oncology and Molecular Medicine - Istituto Nazionale Tumori): once proved non-invasive monitoring in single blood droplets, our method might then have a crucial impact on therapeutic drug monitoring, profiling simultaneously multiple circulating biomarkers, accounting for time evolution of cancer genome and consequent resistance occurrence to drugs treatment. All this features

heighten the significance of our nanoarray as an attractive platform for personalized cancer diagnostic applications.

Moreover, the same nanoarray can serve as a platform for epitope binning. This, combined with fluorescent assays in living cell membranes for co-localization of different receptors, will help understanding the specific functions habilitated by selective binding, paving the way to modular design of synthetic binders.

Since the presence of controversial results concerning the classification of Her2 status and its correlation with circulating ECD-Her2 impairs a clear definition of the impact of shedded Her2 on prognosis and response to anti-Her2 therapies, we performed studies *in vitro* to assess Her2 biology and evaluate ECD-Her2 prognostic value through the correlation between overexpression/dimerization/ECD-Her2 released in normal and cancer cell lines. Also we developed nanotechnology-based platforms to detect Her2 in exosomes, to address their role in cell-cell communication and ultimately in metastasis occurrence. Moving towards this goal we preliminarily evaluated with standard and super-resolution microscopies Her2 quantification and co-localization with other molecular markers of lipid rafts in tumor and healthy cells; then we set up a multi-integrated approach to correlate shedded ECD-Her2 and selection/characterization of the Her2 presence in cell-released exosomes, detected through nanotechnology-based devices, with the fluorescence outputs. This part of the research is still ongoing.

Finally, in a different benchmarking context, that is THR detection, we proved that another class of binders, short nucleic acid aptamers, can be easily and efficiently integrated in the nanoarray for multiplexing analysis. First, we demonstrated in bulk that, by linking a short oligo via a polyethyleneglycol linker to an aptamer designed and optimized for thrombin recognition, the binding affinity was preserved. Then, by immobilizing the DNA-aptamer construct on a SPR chips via DNA-directed immobilization and performing binding affinity measurements via SPR, we obtained a value of  $K_D$  in good agreement with the available literature for in bulk studies, demonstrating that the aptamer functionality was retained upon surface immobilization. Successful thrombin detection was achieved by tuning aptamer surface density on the active area to low values in order to allow aptamers conformational rearrangement necessary to bind the ligands. The measured binding affinity curves overlapped with SPR data impressively well. In particular, DNA nanoarrays also allowed for an estimation of the binding affinity which resulted in good agreement with SPR data. Here, the change of conformation of aptamer upon THR binding towards a more compact structure worked reducing the expected height variation due to immobilization of THR on

the device. Although still detectable, the error associated to the measurements makes this device less reliable than SPR chips to measure binding affinity. However, mechanical compressibility measurements performed on the nanopatches helped to validate the result. The height change measurements on the nanoarrays, moreover, can be combined with the monitoring of roughness variations on the patch and outside it to infer the occurrence of specific binding only on the patch, and exclude the presence of aspecific binding outside it, even without the use of (expensive) sandwich schemes.

We put forward the idea to complement our data with AFM-based force spectroscopy measurements to investigate the variation of the mechanical properties of the DNA-aptamer conjugate structures upon ligand binding. This additional strategy might be particularly profitable given the peculiar properties of aptamers, which undergo a global conformational change upon binding. Once validated aptamers as powerful binders suitable for high sensitive protein detection, Her2 specific aptamer will be selected to study the nanoarray capability with this innovative binder category and to evaluate their performance in terms of sensitivity and selectivity with respect to antibody/nanobody-functionalized AFM platform.

Although the DNA-based nanoarray used throughout this work has been obtained from a serial fabrication process (i.e. nanografting one DNA patch at the time), mass production of multiple-spot nanoarrays can be envisaged by using parallel writing, supramolecular strategies and simplified, low-cost, easy to use detection systems. Parallel writing can be obtained by means of a set of parallel cantilever or by in situ parallel synthesis of DNA strands on the chip layer-by-layer (as used by all of the major DNA sequencing companies as Affymetrix, Illumina and Agilent to produce arrays with short and uneven oligo length, [135] or by the employment of photo-active molecules [136] immobilized on a micro-/nano-array prepared by state-of-the-art lithography techniques, as X-ray lithography, e-beam lithography, EUV lithography, focused ion-beam lithography. For master replication, supramolecular strategies as supramolecular nanostamping (SuNS), a technique used for replicate DNA masters based on the hybridization (or enzymatic in situ synthesis) [137,138] of oligos of DNA onto a master DNA array [139] could be employed, to obtain a sort of in situ synthesis easily scalable to any number of spots. For detection, a simplified topographic readout machine with parallel cantilevers, or the implementation of the multiplexing device into a microfluidic setup with electrical output can be envisaged.

At the end, in comparison with nanografting, the proposed scalable strategies would reduce the precision of molecular conformation and density control, a price paid in favor of a faster

and high throughput nanoassay.

Our work finds its deep meaning in the framework of what is called translational research for personalized medicine: we aim at studying biological phenomena as Her2 protein expression and interactions with other molecules in membranes of tumor-related cell lines, to define new biomarkers for early disease detection and therapy monitoring, and ultimately to translate them into novel targets for “personalized” anti-cancer treatments, to treat this multi-faceted disease by more optimally matching drugs and individuals.



## MATERIALS AND METHODS

### DNA

ssDNA sequences (SH-cF9: SH-(CH<sub>2</sub>)<sub>6</sub>-5'-CTTCACGATTGCCACTTCCAC-3', F9: NH<sub>2</sub>-(CH<sub>2</sub>)<sub>6</sub>-5'-GTGGAAAGTGGCAATCGTGAAG-3', SH-cF5: SH-(CH<sub>2</sub>)<sub>6</sub>-5'-CTTATCGCTTATGACCGGACC-3', F5: NH<sub>2</sub>-(CH<sub>2</sub>)<sub>6</sub>-5'-GGTCCGGTCATAAAGCGATAA-3') were from Biomers GmbH Ulm, Germany.

### Antibodies and Nanobodies

Monoclonal mouse antibodies MGR2 and MGR3 [104,105] were produced at Fondazione IRCCS Istituto Nazionale dei Tumori, Milan. These Abs have been tested in IHC, Immuno Precipitation (CoIP) and Immuno Blot assays [104,105].

Commercial monoclonal human antibodies Trastuzumab and Pertuzumab were from Genentech.

Commercial monoclonal  $\alpha$ -uPA and  $\alpha$ -CD9 antibodies was from MyBioSource.

Single-domain antibodies (VHH) were isolated and produced at the University of Nova Gorica (Slovenia) as described previously using a naïve nanobody library [116], a differential panning approach on whole cells and the cytoplasmic expression of the nanobodies in the presence of sulfhydryl oxidase [117].

### Aptamers

Centre of Excellence for Biosensors, Ajdovščina (Slovenia), provided the selection and affinity characterization of the DNA-aptamer constructs, first carried out *in silico* using the web service UNAFold, developed by Zucker and his coworkers [140]. The designed aptamer constructs were further tested in bulk conditions for their functionality, testing the binding affinity for human thrombin (THR) in a qualitative electrophoretic mobility shift assay (EMSA). Two different aptamer constructs were prepared: the one in which the F9 sequence is directly extending from the aptamer sequence (5'-GGTTGGTGTGGTTGGGTGGAAAGTGGCAATCGTGAAG-3'), named F9<sup>a</sup>THR and with hexaethyleneglycol (HEGL) linker in between, (5'-GGTTGGTGTGGTTGG-HEGL-GTGGAAAGTGGCAATCGTGAAG-3'), named F9-HEGL-<sup>a</sup>THR.

### Proteins and Standardized serum

Recombinant human ECD-Her2 and uPA were from ACRO Biosystems.

Standardized human serum was from Biseko® (Biotest).

## CONJUGATES PRODUCTION

### Antibodies

The conjugation of Abs MGR2, MGR3, Trastuzumab, Pertuzumab and  $\alpha$ -CD9 Ab with the ssDNA sequence F9 and of  $\alpha$ -uPA Ab with F5 was performed by means of click chemistry reaction exploiting the commercial 3-step Protein-Oligo Conjugation Kit SoluLink.

- Protein Modification: Antibodies at a concentration of 2.5-4.0 mg/mL were buffer exchanged into Modification Buffer (100 mM phosphate, 150 mM NaCl, pH 8.0) using Zeba Desalt Spin Columns (Pierce Chemical) before adding 10-20 mole equivalents of HyNic/mole antibody. The reaction was carried out at room temperature for 1.5 hours and successively the HyNic-modified antibody was desalted into conjugation buffer (100 mM phosphate, 150 mM NaCl, pH 6.0).

- Oligonucleotide Modification: The oligonucleotide was desalted into nuclease free water using a 5K MWCO VivaSpin diafiltration apparatus and OD/ $\mu$ L concentration at 260 nm was adjusted to 0.2-0.5 OD/  $\mu$ L. A volume containing 20 equivalents S-4FB was added to the oligonucleotide solution and incubated at room temperature for 2 hours. The 4FB-modified oligonucleotide was equilibrated into conjugation buffer (100 mM phosphate, 150 mM NaCl, pH 6.0).

- Protein-Oligo Conjugation: Volumes of the antibody and oligonucleotide are mixed adding 1/10 volume 10X TurboLink Catalyst Buffer was added to the conjugation solution and the reaction was carried out at room temperature for 2 hours; the amount of the two components used in this step is strictly related to the concentration and the Molar Substitution Ratio (MSR) of both HyNic-modified protein and 4FB-modified oligonucleotide obtained in the previous steps.

The conjugation reaction is visualized spectrophotometrically by determining the absorbance at A354 due to the formation of the chromophoric conjugate bond. The reaction solution was exchanged in PBS using Zeba columns.

### Nanobody

The conjugation of nanobody EM1 with the ssDNA sequence F9 was performed by means of a maleimide reaction: the nanobody, containing a free cysteine at its C-term, was diluted to a concentration of 100  $\mu$ M in Hepes 10 mM pH 7.4 buffer and kept reduced by the addition of TCEP in 10-fold molar excess for 20 minutes at room temperature. F9-maleimide was dissolved in TE buffer (Tris 10mM, EDTA 1mM) pH 8.0 and then added to the nanobody with a molar ratio ssDNA: protein of 10:1 (250:25  $\mu$ M: $\mu$ M). After 2 hours at room

temperature the modified nanobody was separated from reactants and reaction byproducts using a G-25 Illustra Microspin Columns (GE Healthcare Life Science).

## **SURFACE PLASMON RESONANCE**

- **Antibodies and nanobody**

Biacore T100 and Biacore 2000 Surface Plasmon Resonance (SPR) instrument were used at a constant temperature of 25°C. Two experimental designs were set up.

In the first one the recombinant ECD-Her2 protein (diluted in 10 mM Na acetate, pH 4.5) was immobilized over the Biacore CM5 gold chip surface (the dextran matrix immobilized on the gold surface is decorated with many COOH groups) via amine coupling reaction, according to the manufactures' instructions. A binding level of ~1300 RU was reached. HBS-EP+ buffer was flowed (5  $\mu$ L/min) as running buffer over the surface. Binding affinity tests of the Abs MGR2 and MGR3 and the VHH EM1 and their conjugate MGR2-F9, MGR3-F9 and EM1-F9 were performed injecting different concentrations of analytes in running buffer at a flow rate of 30  $\mu$ L/min for 3 minutes (association phase) and afterwards flushing with running buffer for 5 minutes (dissociation phase). For the regeneration of the surface 1 min pulses of a Gly-HCl pH 2.0 solution were used, followed by a stabilization time of 15 min [141].

In the second experimental design a bionitilated cF9 sequence (cF9-biotine, 2  $\mu$ M in PBS buffer) was immobilized over the Biacore SA gold chip surface. A continuous flow (5  $\mu$ L/min) of PBS buffer (running buffer) was maintained during all the experiments. The immobilization through streptavidin-biotin binding was stopped after reaching a binding level of ~1200 RU, corresponding to an amount of ssDNA on the surface that ensure an efficient attachment of the molecules in the following steps of the experiment; then the surface was rinsed with two 1 min pulses of 50 mM NaOH solution, in order to remove unbound cF9-biotine [142]. The hybridization was carried out by incubation with the conjugates at 100  $\mu$ M in TE buffer with 1M NaCl until reaching a binding level of ~ 1200 RU; binding affinity of the ECD-Her2 was evaluated injecting two different concentrations of the protein in running buffer at a flow rate of 30  $\mu$ L/min for 3 min (association phase) and afterwards flushing with running buffer for 10 min (dissociation phase). Since the dissociation phase allows a complete detachment of the protein no regeneration procedure is required.

Binding affinity parameters were determined using the BIAevaluation 3.1 software: SPR responses at the end of the association phase are plotted against analyte (A) concentration and fitted to a single site interaction mode ( $[RU] = RU_{max} - (1/(1 + K_D/[A]))$ ) to

extrapolate the dissociation constant  $K_D$ . This parameter describes the binding affinity and is the ratio  $k_{off}/k_{on}$ .

- **Aptamers**

To test aptamer affinity on surfaces, a Biacore X100 Surface Plasmon Resonance (GE Healthcare) instrument was used at a constant temperature of 25 °C. A continuous flow (5  $\mu\text{L}/\text{min}$ ) of PBS buffer (running buffer) was maintained during all the experiments. First, a biotinylated cF9 sequence (cF9-biotin, 2  $\mu\text{M}$  in PBS buffer) was immobilized over the Biacore SA gold chip surface. The immobilization through streptavidin-biotin binding was stopped after reaching a binding level of  $\sim 1200$  RU, corresponding to an amount of ssDNA on the surface that ensure an efficient attachment of the molecules in the following steps of the experiment; then the surface was rinsed with two 1 min pulses of 50 mM NaOH solution, in order to remove unbound cF9-biotin [142]. The hybridization was carried out by incubation with F9-HEGL-aTHR at 30  $\mu\text{M}$  in TE buffer with 1 M NaCl until reaching a binding level of  $\sim 500$  RU, to form an active layer suitable to detect a binding signal also with the lowest concentrations of analyte. The immobilization procedure was followed by a flow of running buffer for 2 h in order to remove aptamers non-specifically bound to the surface and to stabilize the baseline. After this procedure the signal remained constant without any baseline drifting. Binding affinity tests were performed injecting different dilutions of thrombin (0, 0.2, 0.8, 3.1, 12.5, 50, and 200 nM) in running buffer at a flow rate of 30  $\mu\text{L}/\text{min}$  for 3 min (association phase) and afterwards flushing with running buffer for 5 min (dissociation phase). For the regeneration of the surface 1 min pulses of a 50 mM NaOH solution were used, followed by a stabilization time of 5 min [143]. Binding affinity parameters were calculated using the BIAevaluation 3.1 software.

## **AFM MEASUREMENTS**

- **Ab/Nb-functionalized nanoarray**

Tip-assisted AFM-based nanolithography technique used to fabricate DNA nanoarrays and all high-resolution topographic measurements have been performed using an XE-100 (Park-Systems) with a custom liquid cell at room temperature. First, a biorepellent Self-Assembled Monolayer (SAM) of top oligo-ethylene glycol-terminated alkylthiols (TOEG<sub>6</sub>: HS-(CH<sub>2</sub>)<sub>11</sub>-(OCH<sub>2</sub>CH<sub>2</sub>)<sub>6</sub>-OH, Sigma Aldrich) was prepared on ultraflat stripped gold surfaces following a modified version of the Ulman procedure [144]. A gold sample was soaked in a 300  $\mu\text{M}$  solution of TOEG<sub>6</sub> in ethanol for about 24 hours. Then, it was rinsed

with distilled water and ethanol, dried with a gentle stream of nitrogen, and finally glued inside the AFM liquid cell.

Multiple Nanografting Assembled Monolayers of thiol modified ssDNA SH-cF9 (SH modification at 5' end) were prepared by serial AFM-based nanografting inside the TOEG<sub>6</sub> SAM [74,145,146]: an AFM tip with sufficient rigidity (MicroMasch NSC 19/no Al, spring constant 0.6 nN nm<sup>-1</sup>) was operated at high load (set point/force  $\approx$ 100 nN) on areas of 1  $\mu$ m x 1  $\mu$ m or 2  $\mu$ m x 2  $\mu$ m in order to locally displace the TOEG<sub>6</sub> SAMs and to facilitate the exchange with the thiolated ssDNA biomolecules (5  $\mu$ M in TE buffer 1 M NaCl) present in the liquid cell.

Antibody/nanobody conjugate immobilization was performed via DNA Directed Immobilization (DDI) [86,107], incubating the ssDNA SAM with Abs/VHH-F9 at 100 nM in TE buffer with 1M NaCl. ECD-Her2 binding was promoted through the incubation of the antibody/nanobody nanopatches with a solution containing recombinant protein at different concentrations in PBS buffer (binding curves determination and multiplexing measure) or in Biseko (detection in standardized human serum) with the same incubation time.

Topographic height variations of the nanopatches at each step of the experiment were measured with AFM in gentle contact mode in liquid using a softer AFM tip (MicroMasch CSC 38/no Al, spring constant 0.03 nN nm<sup>-1</sup>), in buffer solution (TE buffer, Tris 10 mM, EDTA 1 mM). In order to minimize perturbation applied force during measurement was the minimum stable value ( $\approx$ 0.1 nN). We already proved that at these conditions nanostructures can be imaged and their height referred to the SAMs carpet ( $\Delta h$ ) can be measured [146]. Results of the AFM topography analysis were expressed as mean  $\pm$  standard deviation (SD) obtained from measurements performed on at least four independent patches ( $n \geq 4$ ).

The fabrication parameters of the nanografting process were systematically tuned and consequentially the density of ssDNA molecules adsorbed in the nanopatch modified [1,8,34]. In particular it was possible to control the nanoscale DNA surface by modifying the number of scanning lines during nanografting over the area, a parameter described by the S/A ratio (where S is the scanned area and A is the area of the final patch) [113].

Regeneration conditions were tested to remove ECD-Her2 (50 nM) from MGR2-functionalized nanoarray: Glycine-HCL pH 1.5–3, NaOH pH 10, 5 M NaCl solutions.

- **Exosomes analysis**

Exosomes were adsorbed to freshly cleaved mica sheets, fixed with 4% paraformaldehyde, and analysed by MFP-3D Stand Alone AFM (Asylum Research) and Solver Pro (NT-MDT) Atomic Force Microscopes. For imaging in air conditions, we worked in dynamic mode conditions using silicon probes (spring constant 0.5-4 N/m, radius of curvature <10nm, Mikromasch). For imaging in liquid conditions, we worked in dynamic mode conditions using silicon nitride probes (spring constant 0.05-0.39 N/m, radius of curvature <10nm, Olympus). Topographic height and phase images were acquired at 128x128, 256x256 and 512x512 pixels with a scan rate typically of 1-2 Hz in air and 0.5-1 Hz in liquid. In order to extract mean height and width of exosomes, we used image processing and particle analysis macros of Igor Pro and Gwyddion softwares.

- **Aptamer nanoarray**

A tip-assisted AFM-based nanolithography technique has been used to fabricate DNA nanoarrays with high surface density ( $1-2 \times 10^{13}$  molecules/cm<sup>2</sup>): using Si cantilevers (NSC36B Mikromasch, spring constant: 0.6 N/m) multiple nanografting assembled monolayers (NAM) of thiol-modified single-stranded DNA (ssDNA), named cF9, were prepared by serial AFM-based nanografting inside a self-assembled monolayer (SAM) of a top oligo ethylene glycol terminated alkanethiol, TOEG ((1-mercaptopundec-11-yl)hexa(ethyleneglycol), HS-(CH<sub>2</sub>)<sub>11</sub>-(OCH<sub>2</sub>CH<sub>2</sub>)<sub>6</sub>-OH from Sigma Aldrich) on ultraflat gold surfaces following standard protocols reported earlier. The DNA patches were obtained promoting the replacement of the TOEG molecules with the oligonucleotides by the AFM tip scanning an area of 1 μm × 1 μm or less at high force (about 100 nN) in the presence of a solution of thiolated ssDNA sequences (5 μM in TE buffer 1 M NaCl) at a scan rate of 2 Hz. Several patches (6–8 for each experiment, to guarantee good statistics) of cF9 ssDNA were produced.

Aptamer immobilization was performed via DDI, incubating the ssDNA SAM with 1:1 mix of F9-HEGL-aTHR and F9 at 2 μM in TE buffer with 1 M NaCl in order to avoid steric hindrance by reducing the aptamer surface density, hence, preserving the activity.

Aptamer-thrombin binding was promoted through the incubation of aptamer nanopatches for one hour with a solution (volume of about 100 μL) containing thrombin at different concentrations (THR buffer: 20 mM Tris pH 7.4, 140 mM NaCl, 5 mM KCl, 1 mM MgCl<sub>2</sub>, 1 mM CaCl<sub>2</sub>); topographic height variations over the NAMs were measured with AFM in gentle contact with standard silicon cantilevers (CSC38 Mikromasch, spring

constant: 0.06 N/m) at a 1 Hz scan rate, applying a force of 0.1 nN to detect and quantify binding affinity.

## FLUORESCENCE IMAGING

- **Nanoarray**

Fluorescence measurements were performed both on direct and indirect “sandwich” configuration. Monoclonal IgG antibodies specific for ECD-Her2 (MGR2, Transtuzumab and Pertuzumab) were directly immobilized via DDI on the surface, incubating the ssDNA nanopatches with the immunoconjugate at 100 nM in TE buffer 1M NaCl. ECD-Her2 binding to immobilized antibodies was obtained incubating nanopatches with a solution containing ECD-Her2 at 100 pM (nanoarray validation) or 10 nM (“epitope mapping” studies).

With respect to direct measurements, EM1-GFP fusion construct (1  $\mu$ M) was incubated for 1 hour over the surface; indirect measurements were performed using a second Ab specific for ECD-Her2 at the saturating concentration of 500 nM and then the secondary fluorescent  $\alpha$ -mouse\_Alexa488 Ab (Termofisher Scientific) diluted 1:500 in PBS buffer and incubated over the surface for 30 minutes. After repeated washing steps with PBS buffer, the gold sample was mounted on a glass coverslip with Vectashield H-1400 mounting (Vector).

Fluorescent images were acquired on an inverted epifluorescence microscope (Nikon Eclipse TiU) using 20x (NA=0.45) and 40x (NA=0.70) air objectives and a dichroic filter for FITC (Nikon, Exc: 465-495 nm DM: 505 nm Em: 515-555 nm). 1600x1200 pixels images were collected using a color digital camera and controller (Nikon DS-Fi2 and Digital Sight DS-L2) at acquisition times ranging from 1 to 10 s.

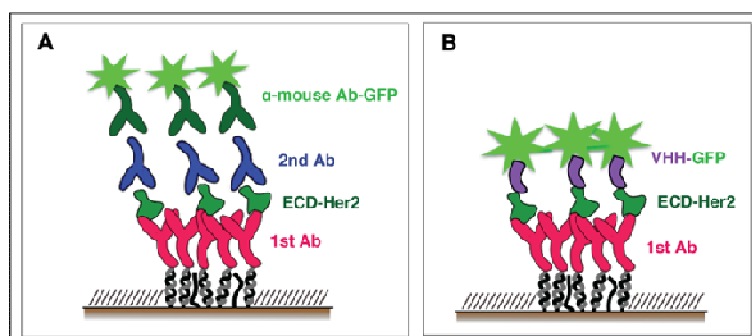


**Fig. 56** Schematic representation of the two different fluorescence assay: in the first one (A) different combinations of two Ab/Nb are exploited to build the “sandwich” of ECD-Her2 binding. The fluorescence signal is obtained with a secondary fluorescence  $\alpha$ -mouse Ab. In the other configuration (B) EM1 conjugated with GFP is exploited as second Ab of the “sandwich”.

- **Cells**

Cells were fixed in 4% paraformaldehyde (20 minutes at room temperature); to avoid aspecific binding cells were incubated for 30 minutes at room temperature with blocking buffer (PBS in the presence of 5% FBS) and 0.1% TritonX-100 (if permeabilization is required).

Her2 receptor (ECD and ICD), caveolin-1 and ADAM10 protease were labeled with saturating concentration of specific unlabeled primary antibodies for 60 minutes at room temperature in PBS. The dye-conjugated secondary Ab was then added. In order to label lipid rafts cells were incubated in the presence FITC-labeled subunit B of cholera toxin for 60 minutes at room temperature. Nuclei were labeled with DAPI (4',6-diamidino-2-phenylindole - 1.5 µg/mL) by means of incubation of 10 minutes. After each incubation step unbound antibodies were removed by washing twice with PBS.

Fluorescent images were acquired on an inverted epifluorescence microscope (Nikon Eclipse TiU) using 20x (NA=0.45) and 60x (NA=0.70) air objectives and a dichroic filter FITC (Nikon, Exc: 465-495 nm DM: 505 nm Em: 515-555 nm), TxRed (Nikon, Exc: 540-580 nm DM: 595 nm Em: 600-660 nm) and UV-2A (Nikon, Exc: 330-380 nm DM: 400 nm Em: 420-up nm). 1024x1024 pixels images were collected using a color digital camera and controller (ORCA Flash4.0 e software HCImage 4.3.1.30 - Hamamatsu) at acquisition times ranging from 20 ms to 10 s.

Stimulated Emission Depletion (STED) microscopy is a confocal super-resolution imaging technique. STED super-resolution is obtained by overlaying an excitation laser and a depletion laser to subtract fluorescence in specific regions of the sample while leaving a center focal spot active to emit fluorescence. For STED experiments KK114-, Alexa488-, Oregon Green488-conjugated secondary Abs were used; STED images were acquired with commercial STED instruments (Leica SP8 3X STED and Leica SP5 NIR-STED), using a white light laser tuned to 470 nm to excite the Alexa488 and Oregon Green488 fluorescence and 640 nm to excite the KK114. For STED images, Alexa488 and Oregon Green488 were used with the 592 nm depletion laser set to 95 % power with a time gating range of 1.5–6.0 ns, and KK114 was used with the 775 nm depletion laser set to 95 % power with a time gating range of 1.2–6.0 ns.

## **CELL CULTURE**

SKBR3, MCF7 and HEK293 cell lines were obtained from the American Type Culture Collection (ATCC) and, according to their specifications, were routinely grown in DEMEM



supplemented with 10% FBS and penicillin/streptomycin. Cells were maintained at 37 °C in a humidified atmosphere of 95% air and 5% CO<sub>2</sub>. For immunofluorescence experiments cells were grown on glass coverslips.

## **EXOSOMES EXTRACTION**

In order to isolate exosomes from culture medium, cells were grown in FBS free DEMEM supplement with 1% BSA and penicillin/streptomycin for 24-48 hours at 37 °C in a humidified atmosphere of 95% air and 5% CO<sub>2</sub>. Cell medium was then picked up and centrifuged first at 300 g and then at 2000 g for 10 minutes to eliminate cells and debris.

For exosomes isolation the size-exclusion qEV columns [133], composed by a resin with an approximately 75 nm pore, were used. After the wash of the column with PBS buffer, the medium sample was loaded on the top; more buffer was added to let the sample entered the column. Immediately the first 3.5 mL were collected as void volume; after the void volume the vesicle fraction of 1 mL was collected.

## **ELISA ASSAY**

The indirect ELISA assay was performed first by coating the antigen ECD-Her2 to PVC microtiter plate. The protein was diluted to a final concentration of 100 µg/mL in carbonate buffer (100 mM, pH 9.6) and 50 µL were used to coat the microplate wells overnight at 4 °C. Then the coating solution was removed and the plate washed three times with PBS. The coated wells were blocked with 1% BSA in PBS (blocking buffer) for 2 hours at room temperature. The plate was washed twice in PBS and serial dilutions (from 100 pM to 1 µM) of primary antibody were added. The plate was washed three times with PBS after 4 hours incubation at 4 °C and finally the Horse Radish Peroxidase (HRP)-conjugated secondary antibody (Sigma) diluted 1:2000 in blocking buffer was added. After the incubation (1 hour at 4 °C) binding detection was assessed by adding the substrate 3,3',5,5'-tetramethylbenzidine (TMB, Pierce). The reaction was stopped with a solution of HCl 1 M after 15 min of incubation at room temperature and optical density was read at 450 nm.

## **STATISTICAL ANALYSIS**

- The Limit of Blank (LoB) is the highest measured test result likely to be observed (typically at 95% certainty) for a sample containing no analyte. Values above LoB are not consistent with the absence of analyte; hence LoB frequently replaces the analytical sensitivity of a method. It is calculated as follow:

$$\text{LoB} = \text{Mean}_{\text{blank}} + 1.645 * (\text{SD}_{\text{blank}})$$

- The Confidence Level is the percentage of all possible samples that can be expected to include the true population parameter. For example, supposing all possible samples were selected from the same population and a confidence interval was computed for each sample, a 95% (or 0.95) confidence level implies that 95% of the confidence intervals would include the true population parameter. It is calculated estimating the population mean, the standard deviation and the multiplier (t-value), using a t-table in which the degree of freedom is based on the sample size, n. A normal random variable X is transformed into a z-score via the following equation:

$$z = (X - \text{mean}) / \text{SD}$$

The z-score is then converted into a confidence level using a z-score table.

## APPENDIX

### **Other AFM-based nanoarrays applications: Mismatch detection in DNA monolayers**<sup>3</sup>

Controlled nanoscale DNA patterning and DNA-based nanoarray can offer a broad set of possible applications that allow, by means of DNA hybridization, to detect specific disease biomarkers. So far different methodologies have been developed in order to increase the selectivity and the sensitivity of DNA/RNA expression profiling, oligonucleotides mismatches detection, microRNA (miRNA) detection.

In this direction we present here two platforms based on different sensing strategies, to detect mismatched and/or perfectly matched complementary DNA strands hybridization into ssDNA oligonucleotide monolayers.

Most current technologies for genotyping and sequencing are based on DNA hybridization, exploiting the high grade of selectivity due to the unique properties of DNA base pairing. Although the understanding of the behavior of nucleic acids on a solid surface has made huge progress from the seminal work of Southern [147] due to the rapid development of DNA microarray and DNA microarray-based techniques [82,148], there are still open questions and bottlenecks limiting the selectivity and the sensitivity of devices that are based on the hybridization of DNA [149]. One example is the detection of single nucleotide polymorphism (SNP) [150]. Single-base variations in a DNA/RNA sequence afflict 1 out of 1000 base pairs in the genome causing small differences in individuals belonging to the same species. This can lead to diseases [151,152,153] or drastically affect the response to pharmacological treatments [154]. SNPs are particularly relevant for applications in the field of pharmacogenomics and population genetics, as a diagnostic tool towards a personalized approach to diseases [155]. However, state-of-the-art devices still are not fully able to identify a single-base mismatch nor to unequivocally distinguish fully and partially matching sequences during hybridization [156,157].

The most common strategies for mismatch detection can be divided in three different categories: hybridization-based detection, detection based on thermal denaturation and protein-mediated detection [150]. For each strategy, different readout systems and experimental designs have been reported, which include fluorescence [158], surface plasmon

---

<sup>3</sup> "Mismatch detection in DNA monolayers by Atomic Force Microscopy and Electrochemical Impedance Spectroscopy" M. D. Nkoua Ngavouka, P. Capaldo, E. Ambrosetti, G. Scoles, L. Casalis, P. Parisse. Beilstein J Nanotechnol. 2016; 7: 220–227.

resonance [159,160], electrochemical [161,162], atomic force microscopy [163,164], colorimetric assays [165], Raman spectroscopy [166]. However, all these state-of-the-art technologies are limited in multiplexing implementation, mutation discrimination and/or sample throughput. Therefore the field is still open for an optimization of strategies to overcome the current limitations [167].

We present here two platforms, which are based on different sensing strategies, to detect mismatched and/or perfectly matched hybridization of complementary DNA strands into ssDNA oligonucleotide monolayers. The first platform exploits atomic force microscopy-based nanolithography (nanografting) to create ssDNA nanoarrays on gold surfaces and then AFM topography measurements to monitor the variation of the height of the nanostructures after loading the complementary/mismatched strands in the liquid cell. In the last years we optimized this nanomechanical approach, which is based in the different rigidity of ss- and dsDNA [81,102,109], enabling the ultrasensitive detection of biomarkers [101]. The second strategy exploits the change in capacitance during the hybridization process, measured at the interface between a ssDNA-functionalized gold electrode and the solution in an electrochemical cell. In a previous work we demonstrated the ability to follow the hybridization of perfectly matched sequences in real time through electrochemical impedance spectroscopy (EIS) measurements on extended ssDNA self-assembled monolayers (SAMs) [168]. Here we successfully tested EIS for the detection of mismatched sequences. From the analysis of hybridization kinetics we distinguished the presence of single or multiple mismatches and their relative position.

Both nanoarrays and EIS devices hold the premises for parallelization, multiplexing and low-volume analysis, making them amenable for point-of-care diagnostics of SNPs. Moreover a comparative analysis between the two techniques allows for a deep understanding of hybridization processes in the presence of single and multiple mismatches.

## **Results and Discussion** □

### **Atomic force microscopy-based assay**

In Figure 1 we report a schematic representation of the AFM- based assay. We immobilize by means of nanografting on a gold surface two ssDNA sequences, differing by one base (reported as a red mark), and carefully measure the height of the DNA nanostructures with respect to the surrounding biorepellent self-assembled monolayer, this last serving as a constant reference for the height measurements ( $h_{\text{ssDNA}}$ , Figure A1a). Then we hybridize with a sequence that is perfectly complementary to one of the two sequences. We expect the

perfect matched (PM) sequence and the one-base mismatched (MM) sequence hybridization to produce a similar increase in height, which follows the change in the nanomechanical properties from ssDNA to dsDNA configuration ( $h_{\text{dsDNA}}$ , Figure A1b). We then perform a thermal treatment to selectively de-hybridize only the MM sequences, as we can measure from the different height response of the two grafted ssDNA structures ( $h_{\text{after treatment}}$ , Figure A1c). Since the non-perfectly matching sequence will have a reduced melting temperature with respect to the perfectly matched (PM) sequence ( $T_{\text{m}}(\text{MM}) < T_{\text{m}}(\text{PM})$ ), its de-hybridization will be favored upon annealing to a temperature ( $T_{\text{ann}}$ ) close or slightly higher than the melting temperature of the perfect matched sequence ( $T_{\text{m}}(\text{MM}) < T_{\text{m}}(\text{PM}) \leq T_{\text{ann}}$ ). We have used our AFM-based nanomechanical approach to distinguish single mismatched DNA base pairs of single nucleotide polymorphisms (SNPs), in particular a T–G mismatch.

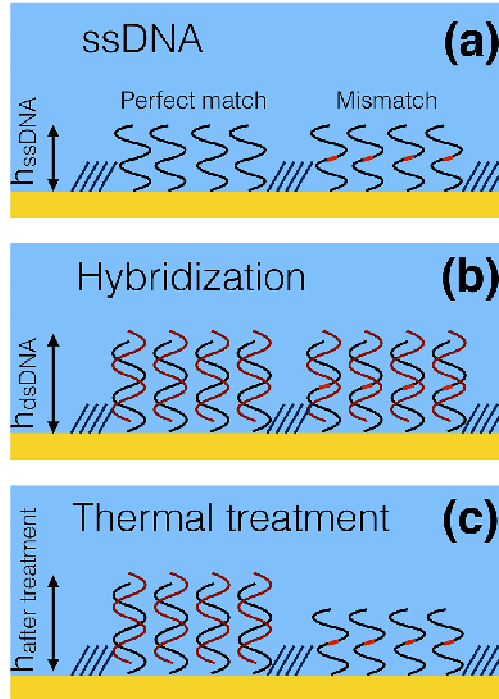


**Figure A1:** Schematics of the atomic force microscopy-based assay. We graft two sets of ssDNA nanostructures, whose sequences differ by one single base, highlighted by a red dot (panel a, b,c). By means of careful AFM topographic measurements, we record the height variation over the ssDNA nanostructures, ( $h_{\text{ssDNA}}$ , panel a) upon hybridization with a strand fully matching only the left grafted strand ( $h_{\text{dsDNA}}$  panel b), upon thermal treatment, ( $h_{\text{after treatment}}$  panel c), evidencing the different de-hybridization behaviour of perfectly matched sequences vs mismatched sequences.

In particular, we chose to immobilize on the surface two 25 bases-long ssDNA sequences, HS-SNP-C and HS-SNP-T (see Table 1) differing from one cytosine vs one thymine. We produced by nanografting patches of each of the two ssDNA sequences into  $1 \mu\text{m}^2$  areas in the biorepellent TOEG6 SAM, using the same grafting parameters (Figure A2a).

sequence name	sequence
HS-SNP-C	HS-(CH <sub>2</sub> ) <sub>6</sub> -5'-tgataatcattacaaaactgaaata-3'
HS-SNP-T	HS-(CH <sub>2</sub> ) <sub>6</sub> -5'-tgataatcattataaaaactgaaata-3'
SNP-coC	5'-tatttcagttttgtaatgattatca-3'
SNP-coT	5'-tatttcagttttataatgattatca-3'
HS_ssDNA	HS-(CH <sub>2</sub> ) <sub>6</sub> -5'-caaaacagcagcaatccaaagatcagacaccccgattacaaatgc-3'
cDNA_3MM	5'-tcatttgaatcgggtgtcggatccttggattgctgctgtttg-3'
cDNA_PM	5'-gcatttgaatcgggtgtctgatcttggattgctgctgtttg-3'
cDNA_2MM	5'-gcatttgaatcgggtgtcggatccttggattgctgctgtttg-3'
cDNA_DOWN	5'-tcttggattgctgctgtttg-3'
cDNA_UP	5'-gcatttgaatcgggtgtctga-3'

**Table 1:** List of the sequences used for the AFM and EIS experiments. The position of the mismatches is typeset in bold.

After grafting, the sample was incubated with the sequence SNP-coC fully matching one strand and matching the second one but for one base, originating a T/G polymorphism. In Figure A2b we report the AFM topographic image after incubation with SNP-coC targets for 1 h. The height variation ( $\Delta b = b - b_{\text{ssDNA}}$ ) after the hybridization step is very similar for the two different sequences (Figure A2d), evidencing the impossibility to clearly distinguish the presence of the mismatched base only by means of height measurements. We therefore designed a melting experiment: we kept the sample in TE buffer, pH 9, for 1 h at 60 °C, a temperature slightly higher than the melting temperature of the PM sequence ( $T_m^{\text{PM}} = 57$  °C,  $T_m^{\text{MM}} = 53$  °C). In Figure A2c we report the AFM topographic image after the thermal treatment and in Figure A2d the relative height changes. We can observe a sensible height decrease in the HS-SNP-T probe only, matching almost completely the initial ssDNA value. This is the sign of a complete de-hybridization of the mismatched sequence, whereas the perfect match probe is only slightly perturbed by this thermal treatment.

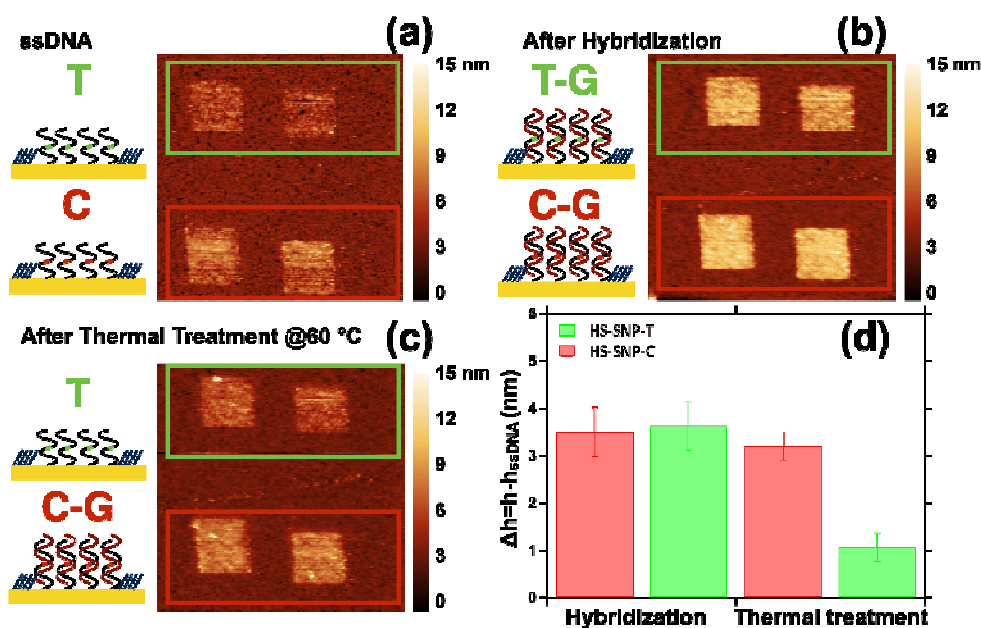


**Figure A2:** Schematic view and AFM topographic images of HS-SNP-C and HS-SNP-T nanografted patches (a) before and (b) after incubation with SNP-C for 1 h and (c) thermal treatment. (d) Histogram of the height variation with respect to the ssDNA patches ( $\Delta h = h - h_{ssDNA}$ ) after the hybridization with SNP-C-Co sequence and after the thermal treatment (1 h at 60 °C).

These successful preliminary experiments demonstrate that our system has the ability to detect mismatches after precise annealing steps, as the ones used in current melting-based SNPs assays [169,170]. The novelty of our assay resides in the possibility of reducing the dimensions of the spots (below  $1 \mu\text{m}^2$ ) and to work multiplexing in small volumes. The use of locked nucleic acids or enzyme-based strategies [167] might improve sensitivity further possibly circumventing the annealing step.

### Electrochemical impedance spectroscopy- based assay

Despite the high sensitivity, the AFM assay does not allow, at the moment, for a real-time investigation of binding events. In order to overcome such limitations, we tested in parallel another device developed in our laboratory [168], based on electrochemical impedance spectroscopy (EIS) [171]. The device exploits the capacitive effects at the interface between an electrode and an electrolytic solution. When a potential is applied to the gold electrode the free ions in solution will rearrange close to the surface creating the so-called double layer capacitance ( $C_{DL}$ ) [172,173]. In presence of a molecular layer between the solution and the electrode, an additional capacitance in series has to be taken in account. In our case, similarly to the AFM experiments, we functionalized the electrode with a low density ssDNA monolayer that serves as a probe for hybridization studies. In Figure A3 we report a scheme of the device as a series of two capacitances, one due to the charged DNA strands,  $C_{ssDNA}$

and the other ( $C_{DL}$ ) to the pure ionic solution [174]. The measurements of the total differential capacitance will be dominated by the smaller capacitance and, since  $C_{ssDNA}$  (densities of about  $10 \mu\text{F}/\text{cm}^2$ )  $<$   $C_{DL}$  (densities of about  $40 \mu\text{F}/\text{cm}^2$ ) [168], will give us a reasonable estimation of the  $C_{ssDNA}$ . In the approximation of parallel plate capacitance we can write  $C_{ssDNA}$  as  $\epsilon \cdot \epsilon_0 (A/d)$ , where  $A$  is the area of the electrode,  $d$  the thickness of the ssDNA layer, and  $\epsilon_0$  and  $\epsilon$  are the dielectric constant of vacuum and ssDNA layer, respectively. When we insert a complementary strand in the electrochemical cell, the molecular recognition between the two strands will cause a change in the capacitance at the interface, due to a combination of height changes, displacement of water molecules upon binding of new strands, and rearrangement of charge density, bringing to a new value for the capacitance,  $C_{dsDNA}$  [175]. Our device can follow the variation of capacitance in real time, allowing for the study of the kinetic of hybridization. Indeed, the eventual presence of a mismatch should change the kinetic of the binding, as already reported by pioneering work of Georgiadis's group [78,176]. Therefore, following in real time the variation of the capacitance we expect to distinguish the presence of mismatched sequences.

We functionalized the electrode with the HS-SNP-T probe and measured the capacitance at the electrode (red dots in Figure A3).

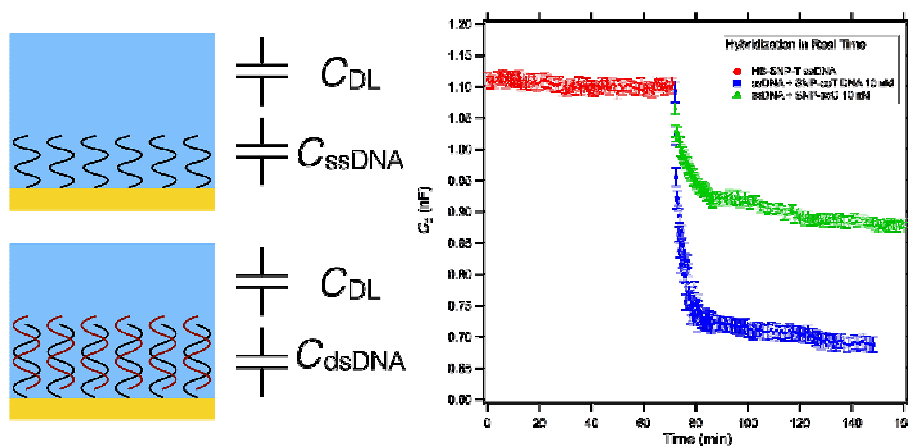


**Figure A3:** Schematic representation of the electrode/electrolyte interface. The first layer in contact with the gold electrode is the ssDNA self-assembled monolayer, modelled as a capacitance  $C_{ssDNA}$ . Then we have the ions present in solution that arrange in response to the gold and DNA charges forming the so-called double layer capacitance  $C_{DL}$ , in series with  $C_{ssDNA}$ . When hybridization occurs, the binding of the complementary strand will produce a change in capacitance due to height changes, substitution of water molecules in the biological layer, and changes in the electrical charge density. The capacitance, extracted from the impedance measured in our electrochemical setup, is plotted versus time for the ssDNA-functionalized electrode (red curve) and for the mismatched (green) and perfectly matching (blue) complementary sequences.



The value of  $C_{ssDNA}$  is shown to be constant over an hour of continuous measurements, as already demonstrated by Ianeselli *et al.* [168]. After addition of the perfectly matching sequence SNP-coT (blue squares) in the electrochemical cell, we observed a fast decrease of the capacitance, followed by a subsequent slow decay that reaches a plateau at a value of capacitance 36% less than the initial value, as a sign of the occurred hybridization. When we insert on the regenerated electrode with the HS-SNP-T probe the mismatched sequence SNP-coC (green triangles) we observe a slower decay of the capacitance tending to a plateau much closer to the initial  $C_{ssDNA}$  value than the perfectly matched one (21% variation), confirming a different kinetic behavior and a less efficient hybridization. Our results are in good agreement with previous reports of Georgiadis based on SPR measurements [176]. We can observe here that the EIS measurements allow for distinguishing the mismatched and perfectly matched sequences by observing a different kinetic behavior and a different capacitance plateau, whereas AFM was not able to directly detect a height difference. Indeed, the changes of capacitance at the functionalized electrode are the results of a combination of changes of height in the molecular case and rearrangement of charge density. The distortions on the DNA structure due to the mismatched bases can modify the charge distribution inside the molecular layer [177], causing a change in the capacitance that is readable in the EIS measurement, even if does not significantly affect the height of the layer after the hybridization.

We further tested our device exposing a 44 bases ssDNA (HS\_ssDNA\_44) probe to five different sequences: a perfect match (cDNA\_44\_PM), a double mismatch (cDNA\_44\_2MM), a triple mismatch (cDNA\_44\_3MM), and two 22 bases sequences complementary to the bottom half (cDNA\_44\_DOWN) and top half (cDNA\_44\_UP) part of the ssDNA\_44 sequence, respectively.

In Figure A4a we report the study of the kinetics of DNA hybridization in the presence of 2 MM (green triangles) and 3 MM (black markers) mismatches compared with the PM (blue squares) sequence. We can clearly distinguish the behavior of the three differently matching sequences. As expected we measured a slower kinetics and a lower plateau value going from the PM (36% variation) to 2 MM (17% variation) and finally to 3 MM (10% variation).

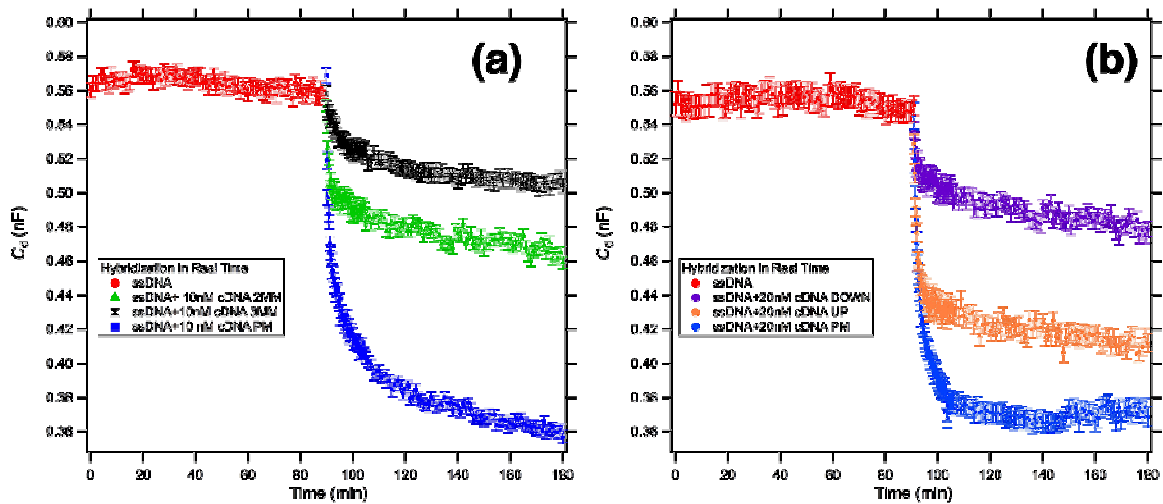


**Figure A4:** Differential capacitance measurements of the kinetics of DNA hybridization in presence of multiple mismatches (a) and in presence of partially complementary sequences (b). The red signal represents the differential capacitance of a low-density 44 bases ssDNA SAM functionalized WE measured in 100 mM KCl. (a) In blue we report the hybridization with the fully matching sequence, in green the hybridization with a sequence with 2 MMs, and in black the hybridization with a sequence with 3 MM. (b) In blue we report the hybridization with the fully matching sequence, in orange the hybridization with a 22mer sequence complementary with the upper part (far from the gold surface) of the target and in purple the hybridization with a 22mer sequence complementary with the lower part (close to the gold surface) of the target.

Analogously, we observe in Figure A4b the evolution of the differential capacitance in presence of two 22 bases-long sequences complementary to the bottom half (cDNA\_44\_DOWN) and top half (cDNA\_44\_UP) part of the ssDNA\_44 sequence, respectively. The curves follow more or less the same trend: an initial fast decay and then a slow decay to an asymptotic value representative of the efficiency of the hybridization. The kinetics and the asymptotic value are, respectively, slower and lower for the two half sequences with respect to the PM. Notably, the kinetics and efficiency of hybridization is much lower for the down matching sequence than for the up matching sequence. The 44 bases probe brush can in fact hinder the hybridization of the bottom part, while the upper part is made more available for the target sequence. Noteworthy, we observe a sensible variation between up and down hybridization in the presence of as low as 20 nM target concentration. The increase in sensitivity with respect to previous results reported by Georgiadis group [176] can be attributed to the applied electric field during the EIS real time hybridization measurements. Such electric field can indeed favor the hybridization process, as already reported by [178], accelerating the kinetics and improving the efficiency of the hybridization.

## Conclusion

We proposed here two different sensing strategies based on the use of ssDNA monolayers tethered to gold substrates, for the detection of mismatches in DNA oligonucleotides. Both the strategies are label-free and are sensitive enough to detect point mutations. In Table 2 we report a comparison between the performance of our two approaches (nano-mechanical and electro-chemical) and current label-free surface-based biosensing strategies, according to recent literature. As we can see from the table, SPR strategies seem to be the most promising in terms of limit of detection. However, in these devices the surface area is larger, limiting multiplexing and small volume operations [159,160].

By contrast, the nano-mechanical approach on DNA nanoarrays although hampered by the time consuming processes of annealing and AFM height measurements (in line with benchmark of AFM-based assays reported in literature [156,163,164]), allows for a straightforward multiplexing. Ultimate sensitivity has been demonstrated for these arrays (100 pM, [179]), making them overall amenable to less invasive diagnostic analysis with a sensible reduction of the volume of the analyte till single cell [101].

Finally, our electrochemical measurements combine high sensitivity with real-time analysis, allowing for an accurate study of the kinetics and of the efficiency of the hybridization in mismatched targets. In our case, we were able to clearly distinguish the presence of single, or multiple mismatches and also the position with respect to the gold surface of the missing base-pairs. Due to the relatively simple geometry, the device could be easily further miniaturized and integrated in multiplexed arrays through microfluidic systems, allowing for point-of-care diagnostics. Our results demonstrated that nano-mechanical and EIS strategies are state of the art for the detection of SNP, confirming the relevance of immobilized DNA on solid supports in life science studies, including single cell RNA characterization, gene expression profile and genetic variability. Moreover, the complementarity of the two techniques (one more sensitive to the morphological and mechanical changes of the DNA layer, the other more sensitive to its charge density) let us conclude that the structural deformations related to a single mismatch have a strong influence on the charge distribution only, leaving the molecular structure not significantly affected.

## Materials and Methods

### Fabrication and measurement processes of AFM-based assays

Gold-coated substrates were immersed in 300  $\mu\text{M}$  of top oligo(ethylene glycol)-terminated alkylthiols (TOEG6:  $\text{HS}-(\text{CH}_2)_{11}-(\text{OCH}_2\text{CH}_2)_6-\text{OH}$ ) ethanol solutions, overnight, to allow

for the adsorption and assembly of a full monolayer with bio-repellent characteristics [112]. The samples were then removed from the solution, rinsed with ethanol and water to remove loosely bound molecules and placed in a customised liquid cell for the AFM experiments.

All AFM experiments were carried out on a XE-100 Park Instruments with a customised liquid cell. Si cantilevers (NSC36B Mikromasch, spring constant: 0.6 N/m) were used for the nanografting experiments. Briefly, the AFM tip is scanned at high load (approx. 100 nN) over the TOEG6 SAM, operating in a buffer solution (10 mM Tris-HCl, 1 mM EDTA, (hereafter TE), 1 M NaCl, pH 7.1) containing 5  $\mu$ M thiolated ssDNA oligonucleotides. The applied load is sufficient to displace the TOEG6 molecules from the gold surface, which are subsequently locally substituted by the thiolated ssDNA molecules, creating ssDNA patches embedded in the surrounding TOEG6 carpet. Exchanging the buffer and the thiolated ssDNA probes, it is possible to sequentially immobilize different sequences on the same substrate. The parameters for nanografting have been properly chosen to obtain a surface density of probes optimal for the detection of target hybridization, following previous works of our group [81,102,109]. After the immobilization the ssDNA patches are measured through AFM topographic imaging in soft contact with standard silicon cantilevers (CSC38 Mikromasch, spring constant: 0.06 N/m) at 1 Hz scan rate, applying a force of 0.1 nN. Hybridization was monitored after the addition of the required target solutions (1  $\mu$ M target in TE buffer 1 M NaCl) into the AFM liquid cell for 1 h. All DNA sequences used in the present work are listed in Table 1.

### **Fabrication and measurement processes for EIS-based assay**

Detailed fabrication processes and layout of the electrochemical impedance spectroscopy experiments have been reported by Ianeselli and co-workers [168]. Briefly, the setup consists of a glass slide with lithographically fabricated working (WE) and counter (CE) gold electrodes. The two electrodes are covered with insulating resist leaving exposed to the solution only the active part, to avoid spurious effects. To confine the drop of solution and to carefully position the reference electrode (a classical millimetre-sized Ag/AgCl pellet electrode) we placed around the electrodes a silicone circular cell (6 mm in diameter, 4 mm in height). The WE and CE electrodes were functionalized with thiolated ssDNA molecules using a well-established procedure for DNA SAMs on gold [79,81]. Initially the electrodes were wetted for 10 min with a drop of a high-ionic-strength buffer, TE 1 M NaCl, containing 1  $\mu$ M thiolated ssDNA. In this way a low-density ssDNA SAM (about  $2 \times 10^{12}$  to  $3 \times 10^{12}$  molecules/cm<sup>2</sup>) was obtained [79]. After DNA-functionalization the devices were

rinsed with the buffer solution used for the measurements, 100 mM KCl, and the capacitance at the electrode/electrolyte interface was measured. In the hybridization step the cell is filled with a drop of the same hybridizing buffer solution, 100 mM KCl, containing the complementary or partially complementary DNA strand at different concentrations.

The electrochemical current  $I_{\text{rms}}$  is monitored between WE and CE with a Heka PG340 USB potentiostat upon application of a 10 mV AC voltage at 100, 200, 250 and 400 Hz. In this regime of frequencies the total impedance is dominated by the capacitance at the electrode/electrolyte interface, allowing for the extraction of the differential capacitance simply from a linear fit of  $I_{\text{rms}}$ . The functionalized electrodes can be regenerated after the hybridization process by means of a thermal treatment in TE buffer (pH 9) for 1 h in oven at a temperature 10 °C higher than the melting temperature of the used DNA sequence. The differential capacitance after the regeneration treatment maintains its original value within the error bars.

## Bibliography

- 1- International Agency for Research on Cancer (IARC) and World Health Organization (WHO). GLOBOCAN 2012: Estimated cancer incidence, mortality and prevalence worldwide in 2012. [http://globocan.iarc.fr/Pages/fact\\_sheets\\_cancer.aspx](http://globocan.iarc.fr/Pages/fact_sheets_cancer.aspx), 2016.
- 2- Bray F, Ren JS, Masuyer E, Ferlay J. Global estimates of cancer prevalence for 27 sites in the adult population in 2008. *Int J Cancer*. 2013; 132:1133-1145.
- 3- Reis-Filho JS, Weigelt B, Fumagalli D, Sotiriou C. Molecular profiling: moving away from tumor philately. *Sci Transl Med*. 2010; 2:47ps43.
- 4- Sotiriou C, Pusztai L. Gene-expression signatures in breast cancer. *N Engl J Med*. 2009; 360:790-800.
- 5- Kreso A, Dick, J. E. Evolution of the Cancer Stem Cell Model. *Cell Stem Cell*. 2014; 14: 275-291.
- 6- Sims AH, Howell A, Howell SJ, Clarke RB. Origins of breast cancer subtypes and therapeutic implications. *Nat Clin Pract Oncol*. 2007; 4(9):516-25.
- 7- Malhotra GK, Zhao X, Band H, Band V. Histological, molecular and functional subtypes of breast cancers. *Cancer Biology and Therapy*. 2010; 10(10):955-960.
- 8- Breast cancer intrinsic subtype classification, clinical use and future trends. Dai et al. *Am J Cancer Res* 2015;5(10):2929-2943
- 9- Sørlie T, Perou CM, Tibshirani R, Aas T, Geisler S, Johnsen H, Hastie T, Eisen MB, van de Rijn M, Jeffrey SS, Thorsen T, Quist H, Matese JC, Brown PO, Botstein D, Lonning PE, Borresen-Dale AL. Gene expression patterns of breast carcinomas distinguish tumor subclasses with clinical implications. *Proc Natl Acad Sci U S A*. 2001; 98:10869–10874.
- 10- Perou CM, Sorlie T, Eisen MB, van de Rijn M, Jeffrey SS, Rees CA, Pollack JR, Ross DT, Johnsen H, Akslen LA, Fluge O, Pergamenschikov A, Williams C, Zhu SX, Lonning PE, Borresen-Dale AL, Brown PO and Botstein D. Molecular portraits of human breast tumours. *Nature*. 2000; 406: 747-752.
- 11- Lewis Phillips GD, *et al*. Targeting HER2-Positive Breast Cancer with Trastuzumab-DM1, an Antibody–Cytotoxic Drug Conjugate. *Cancer Res*. 2008; 68(22):9280-90.
- 12- Sotiriou C, Neo SY, McShane LM, Korn EL, Long PM, Jazaeri A, Martiat P, Fox SB, Harris AL and Liu ET. Breast cancer classification and prognosis based on gene expression profiles from a population-based study. *Proc Natl Acad Sci U S A*. 2003; 100: 10393-10398.
- 13- Barnes PJ, Boutilier R, Chiasson D, Rayson D. Metaplastic breast carcinoma: clinical-pathologic characteristics and HER2/neu expression. *Breast Cancer Research and Treatment*. 2005; 91(2):173–178.
- 14- Petrucelli N, Daly MB, Feldman GL. Hereditary breast and ovarian cancer due to mutations in BRCA1 and BRCA2. *Genetics in Medicine*. 2010; 12:245–259.
- 15- Hagemann IS. Molecular Testing in Breast Cancer. *Arch Pathol Lab Med*. 2016; 140: 815-824.
- 16- Berse B, Lynch JA. Molecular diagnostic testing in breast cancer. *Semin Oncol Nurs*. 2015; 31(2):108-21.
- 17- Guttery DS, Blighe K, Page K, Marchese SD, Hills A, Coombes RC, Stebbing J, Shaw JA. Hide and seek: tell-tale signs of breast cancer lurking in the blood. *Cancer Metastasis Rev*. 2013; 32(1-2):289-302.
- 18- Brock G, Castellanos-Rizaldos E, Hu L, Coticchia C, Skog J. Liquid biopsy for cancer screening, patient stratification and monitoring. *Transl Cancer Res*. 2015; 4(3):280-290.
- 19- Huang ZH, Li LH, Hua D. Quantitative analysis of plasma circulating DNA at diagnosis and

- during follow-up of breast cancer patients. *Cancer Letters*. 2006; 243(1):64–70.
- 20- Allard WJ, Matera J, Miller MC, *et al.* Tumor cells circulate in the peripheral blood of all major carcinomas but not in healthy subjects or patients with nonmalignant diseases. *Clin Cancer Res*. 2004; 10:6897-904.
  - 21- Ratajczak J, Wysoczynski M, Hayek F, *et al.* Membrane-derived microvesicles: important and underappreciated mediators of cell-to-cell communication. *Leukemia*. 2006; 20:1487-95.
  - 22- Valadi H, Ekström K, Bossios A, *et al.* Exosome-mediated transfer of mRNAs and microRNAs is a novel mechanism of genetic exchange between cells. *Nat Cell Biol*. 2007; 9:654-9.
  - 23- Harris DA, Patel SH, Gucek M, Hendrix A, Westbroek W, Taraska JW, Cao J. Exosomes Released from Breast Cancer Carcinomas Stimulate Cell Movement. *PLoS ONE*. 2015; 10(3):e0117495.
  - 24- Koga K, Matsumoto K, Akiyoshi T, Kubo M, Yamanaka N, Tasaki A, Nakashima H, Nakamura M, Kuroki S, Tanaka M, Katano M. Purification, characterization and biological significance of tumor-derived exosomes. *Anticancer Res*. 2005; 25(6A):3703-7.
  - 25- Carney WP, Bernhardt D, Jasani B. Circulating HER2 Extracellular Domain: A Specific and Quantitative Biomarker of Prognostic Value in all Breast Cancer Patients? *Biomarkers in Cancer*. 2013; 5:31-39.
  - 26- Rubin I, Yarden Y. The basic biology of HER2. *Ann Oncol*. 2001; 12(S1):S3-8.
  - 27- Yarden Y. Biology of HER2 and its importance in breast cancer. *Oncology*. 2001; 61(S2):1-13.
  - 28- Gutierrez C, Schiff R. HER 2: Biology, Detection, and Clinical Implications. *Arch Pathol Lab Med*. 2011; 135(1):55–62.
  - 29- Iqbal N. Iqbal N. Human Epidermal Growth Factor Receptor 2 (HER2) in Cancers: Overexpression and Therapeutic Implications. *Molecular Biology International*. 2014; Article ID 852748, 9 pages.
  - 30- Tsé C, Gauchez AS, Jacot W, Lamy PJ. HER2 shedding and serum HER2 extracellular domain: Biology and clinical utility in breast cancer. *Cancer Treatment Review*. 2012; 38(2):133-142.
  - 31- Pupa SM, Menard S, Morelli D, Pozzi B, De Palo G, Colnaghi MI. The extracellular domain of the c-erbB-2 oncoprotein is released from tumor cells by proteolytic cleavage. *Oncogene*. 1993; 8(11):2917–2923.
  - 32- Aurilio G, Nolè F, *et al.* Serum HER2 extracellular domain levels and HER2 circulating tumor cell status in patients with metastatic breast cancer. *Future Oncology*. 2016; 12:2001-2008.
  - 33- Wang J, Willumsen N, Zheng O, Xue Y, Karsdal MA, Bay-Jensen AC. Bringing Cancer Serological Diagnosis to a New Level - Focusing on HER2, Protein Ectodomain Shedding and Neoepitope. *Technology Future Oncol*. 2013; 9(1):35-44.
  - 34- Lam L, McAndrew N, Yee M, Fu T, Tchou GJ, Zhang H. Challenges in the clinical utility of the serum test for HER2 ECD. *Biochim Biophys Acta*. 2012; 1826(1):199–208.
  - 35- Ali SM, Carney WP, Esteva FJ, Fournier M, Harris L, Köstler WJ, Lotz JP, Luftner D, Pichon MF, Lipton A; Serum HER-2/neu Study Group. Serum HER-2/neu and relative resistance to trastuzumab-based therapy in patients with metastatic breast cancer. *Cancer*. 2008; 113(6):1294-301.
  - 36- Loo LN, Capobianco JA, Wu W, Gao X, Shih WY, Shih WH, Pourrezaei K, Robinson MK, Adams GP. Highly sensitive detection of HER2 extracellular domain (ECD) in the serum of breast cancer patients by piezoelectric microcantilevers (PEMS). *Anal Chem*. 2011; 83(9):3392–3397.

- 37- Mahfoud OK, Rakovich TY, Prina-Mello A, Movia D, Alves F, Volkov Y. Detection of ErbB2: nanotechnological solutions for clinical diagnostics. *RSC Adv.* 2014; 4:3422-3442.
- 38- Molina MA, Codony-Servat J, Albanell J, Rojo F, Arribas J, Baselga J. Trastuzumab (Herceptin), a Humanized Anti-HER2 Receptor Monoclonal Antibody, Inhibits Basal and Activated HER2 Ectodomain Cleavage in Breast Cancer Cells. *Cancer Res.* 2001; 61(12):4744-9.
- 39- Desmedt C, Sperinde J, Piette F, *et al.* Quantitation of HER2 expression or HER2:HER2 dimers and differential survival in a cohort of metastatic breast cancer patients carefully selected for trastuzumab treatment primarily by FISH. *Diagn Mol Pathol.* 2009; 18(1):22–29.
- 40- Ali SM, Carney WP, Esteva FJ, Fournier M, Harris L, Köstler Wolfgang J, Lotz JP, Luftner D, Pichon MF, Lipton A. Serum HER-2/neu and relative resistance to trastuzumab-based therapy in patients with metastatic breast cancer. *Cancer* 2008; 113:1294–1301.
- 41- Franklin MC, Carey KD, Vajdos FF, Leahy DJ, de Vos AM, Sliwkowski MX. Insights into ErbB signaling from the structure of the ErbB2-pertuzumab complex. *Cancer Cell.* 2004; 5(4):317–328.
- 42- Wolff AC, Hammond ME, Schwartz JN, Hagerty KL, Allred DC, Cote RJ, Dowsett M, Fitzgibbons PL, Hanna WM, Langer A, McShane LM, Paik S, Pegram MD, Perez EA, Press MF, Rhodes A, Sturgeon C, Taube SE, Tubbs R, Vance GH, van de Vijver M, Wheeler TM, Hayes DF. American Society of Clinical Oncology/College of American Pathologists guideline recommendations for human epidermal growth factor receptor 2 testing in breast cancer. *Journal of clinical oncology.* 2007; 25:118–145.
- 43- Carney WP, Leitzel K, Ali S, Neumann R, Lipton A. HER-2/neu diagnostics in breast cancer. *Breast Cancer Res.* 2007; 9(3):207.
- 44- Kricka LJ. Human anti-animal antibody interferences in immunological assays. *Clinical chemistry.* 1999; 45:942–956.
- 45- Leach MF, Aubuchon JP. False reactivity in GTI Pak Plus ELISA kits due to the presence of antimouse antibody in patients' samples. *Immunohematology.* 2003; 19:112–116.
- 46- Carvajal-Hausdorf DE, Schalper KA, Puztai L, Psyrri A, Kalogeras KT, Kotoula V, Fountzilas G, Rimm DL. Measurement of Domain-Specific HER2 (ERBB2) Expression May Classify Benefit From Trastuzumab in Breast Cancer. *JNCI J Natl Cancer Inst.* 2015; 107:djv136.
- 47- Tse C, Lamy PJ. Clinical utility of serum human epidermal growth factor receptor 2 extracellular domain levels: stop the shilly-shally--it is time for a well-designed, large-scale prospective study. *Journal of clinical oncology.* 2009; 27:e286–287.
- 48- Ghedini GC, Ciravolo V, Tortoreto M, Giuffrè S, Bianchi F, Campiglio M, Mortarino M, Figini M, Coliva A, Carcangiu ML, Zambetti M, Piazza T, Ferrini S, Ménard S, Tagliabue E, Pupa SM. Shed HER2 extracellular domain in HER2-mediated tumor growth and in trastuzumab susceptibility. *J. Cell. Physiol.* 2010; 225:256–265.
- 49- Babina IS, Donatello S, Nabi IR, Hopkins AM. Lipid Rafts as Master Regulators of Breast Cancer Cell Function. 2011.
- 50- Edidin, M. The state of lipid rafts: from model membranes to cells. *Annu Rev Biophys Biomol Struct.* 2003; 32:257–83.
- 51- Simons K, Toomre D. Lipid rafts and signal transduction. *Nat Rev Mol Cell Biol.* 2000; 1:31–9.
- 52- Nagy P, Vereb G, Sebestyén Z, Horváth G, Lockett SJ, Damjanovich S, *et al.* Lipid rafts and the local density of ErbB proteins influence the biological role of homo- and heteroassociations of ErbB2. *J Cell Sci.* 2002; 115:4251–62.



- 53- Grossmann C, Husse B, Mildenerger S, Schreier B, Schuman K, Gekle M. Colocalization of mineralocorticoid and EGF receptor at the plasma membrane. *Biochim Biophys Acta - Mol Cell Res.* 2010; 1803:584–90.
- 54- Pickl M, Ries CH. Comparison of 3D and 2D tumor models reveals enhanced HER2 activation in 3D associated with an increased response to trastuzumab. *Oncogene.* 2009; 28:461–468.
- 55- Qian N, Ueno T, Kawaguchi-Sakita N, Kawashima M, Yoshida N, Mikami Y, Wakasa T, Shintaku M, Tsuyuki S, Inamoto T, Toi M. Prognostic significance of tumor/stromal caveolin-1 expression in breast cancer patients. *Cancer Science.* 2011; 102:1590–1596.
- 56- Senetta R, Stella G, Pozzi E, Sturli N, Massi D, Cassoni P. Caveolin-1 as a promoter of tumour spreading: when, how, where and why. *Journal of Cellular and Molecular Medicine.* 2013; 17(3):325-336.
- 57- Sanderson MP, Keller S, Alonso A, Riedle S, Dempsey PJ, Altevogt P. Generation of Novel, Secreted Epidermal Growth Factor Receptor (EGFR/ErbB1) Isoforms Via Metalloprotease-Dependent Ectodomain Shedding and Exosome Secretion. *Journal of cellular biochemistry.* 2008; 103(6):1783-1797.
- 58- Amorim M, Fernandes G, Oliveira P, Martins-de-Souza D, Dias-Neto E, Nunes D. The overexpression of a single oncogene (ERBB2/HER2) alters the proteomic landscape of extracellular vesicles. *Proteomics.* 2014; 14:1472–1479.
- 59- Klinker DJ, Kulkarni YM, Wu Y, Byrne-Hoffman C. Inferring alterations in cell-to-cell communication in HER2+ breast cancer using secretome profiling of three cell models. *Biotechnology and bioengineering.* 2014; 111(9):1853-1863.
- 60- Bhandare N, Narayana A Applications of Nanotechnology in Cancer: A Literature Review of Imaging and Treatment. *J Nucl Med Radiat Ther.* 2014; 5:195.
- 61- Nagahara LA, Lee JS, Molnar LK, Panaro NJ, Farrell D, *et al.* Strategic workshops on cancer nanotechnology. *Cancer Res.* 2010; 70:4265-4268.
- 62- Misra R, Acharya S, Sahoo SK. Cancer nanotechnology: application of nanotechnology in cancer therapy, *Drug Discovery Today.* 2010; 15:842-850.
- 63- Heath JR, Davis ME, Hood L. Nanomedicine Targets CANCER: Viewing each human body as a system of interacting molecular networks and targeting disruptions in the system with nanoscale technologies can transform how disease is understood, attacked and possibly prevented. *Scientific American.* 2009; 300(2):44-51.
- 64- Parvanian S, Mostafavi SM, Aghashiri M. Multifunctional nanoparticle developments in cancer diagnosis and treatment. *Sensing and Bio-Sensing Research.* Available online 11 August 2016, ISSN 2214-1804
- 65- Arlett JL, Myers EB, Roukes ML. Comparative advantages of mechanical biosensors. *Nature nanotechnology.* 2011; 6(4):10.1038/nnano.2011.44.
- 66- Hall DA, Ptacek J, Snyder M. Protein Microarray Technology. *Mechanisms of Ageing and Development.* 2007; 128(1):161–167.
- 67- Reymond Sutandy F, Qian J, Chen CS, Zhu H. Overview of Protein Microarrays. *Current Protocols in Protein Science / Editorial Board, John E. Coligan ... [et AL],* 2013).
- 68- Creighton CJ, Huang S. Reverse phase protein arrays in signaling pathways: a data integration perspective. *Drug Design, Development and Therapy.* 2015; 9:3519–3527.
- 69- Raigoza AF, Dugger JW, Webb LJ. Review: Recent Advances and Current Challenges in Scanning Probe Microscopy of Biomolecular Surfaces and Interfaces. *ACS Applied Materials & Interfaces.* 2013; 5(19):9249-9261.
- 70- Binnig G, Quate CF, Atomic force microscope. *Phys Rev Lett.* 1986; 56:930–933.

- 71- Santos NC, Castanho MRB. An overview of the biophysical applications of atomic force microscopy. *Biophys Chem.* 2004; 107:133–49.
- 72- Jalili N, Laxminarayana K. A review of atomic force microscopy imaging systems: application to molecular metrology and biological sciences. *Mechatronics.* 2004; 14:907-945.
- 73- Love C, Estroff LA, Kriebel JK, Nuzzo RG, Whitesides GM. Self-Assembled Monolayers of Thiolates on Metals as a Form of Nanotechnology. *J Chemical Reviews.* 2005; 105(4):1103-1170.
- 74- Liu M, Amro NA, Liu G. Nanografting for surface physical chemistry. *Annu Rev Phys Chem.* 2008; 59:367–386.
- 75- Mendes PM, Yeung CL, Preece JA. Bio-nanopatterning of surface. *Nanoscale Res Lett.* 2007; 2:373.
- 76- Yan L, Zhao XM, Whitesides GM. Patterning a Preformed, Reactive SAM Using Microcontact Printing. *J Am Chem Soc.* 1998; 120:6179-6180.
- 77- Peterlinz KA, Georgiadis RM, Herne TM, Tarlov MJJ. Observation of Hybridization and Dehybridization of Thiol-Tethered DNA Using Two-Color Surface Plasmon Resonance Spectroscopy. *Am. Chem. Soc.* 1997; 119(14): 3401–3402.
- 78- Peterson AW, Heaton RJ, Georgiadis RM. The effect of surface probe density on DNA hybridization. *Nucleic Acids Res.* 2001; 29(24):5163–5168.
- 79- A. Peterson, R. Heaton, and R. Georgiadis. The effect of surface probe density of DNA. Hybridization. *Nucleic Acids Research.* 2001; 29(24):5163–5168.
- 80- Ostuni E, Chapman RG, Holmlin RE, Takayama S; Whitesides GM. A survey of structure - property relationships of surfaces that resist the adsorption of protein. *Langmuir.* 2001; 17:5605–5620.
- 81- Mirmomtaz E, Castronovo M, Grunwald C, Bano F, Scaini D, Ensafi AA, Scoles G, Casalis L. Quantitative Study of the Effect of Coverage on the Hybridization Efficiency of Surface-Bound DNA Nanostructures. *Nano Letters.* 2008; 8(12):4134-4139.
- 82- Heller M. DNA microarray technology: devices, systems, and applications. *J Annu Rev Biomed Eng.* 2002; 4:129–153.
- 83- Liang J, Castronovo M, Scoles G. DNA as Invisible Ink for AFM Nanolithography. *Journal of the American Chemical Society.* 2012; 134(1):39-42.
- 84- Shiu SH, Borevits JO. The next generation of microarray research: applications in evolutionary and ecological genomics. *Heredity (Edinb).* 2008; 100(2):141-9.
- 85- Kingsmore SF. Multiplexed protein measurement: technologies and applications of protein and antibody arrays. *Nature Reviews. Drug Discovery.* 2006; 5(4):310–320.
- 86- Niemeyer CM, Boldt L, Ceyhan B, Blohm D. DNA-Directed immobilization: efficient, reversible, and site-selective surface binding of proteins by means of covalent DNA-streptavidin conjugates. *Annal Biochem.* 1999; 268(1):54-63.
- 87- Niemeyer CM, Sano T, Smith CL, Cantor CR. Oligonucleotide-directed self-assembly of proteins: semisynthetic DNA--streptavidin hybrid molecules as connectors for the generation of macroscopic arrays and the construction of supramolecular bioconjugates. *Nucleic Acids Res.* 1994; 22(25):5530- 5539.
- 88- Shin YS, Ahmad H, Shi Q, Kim H, Pascal TA, Fan R, Goddard WA 3rd, Heath JR. Chemistries for patterning robust DNA microbarcodes enable multiplex assays of cytoplasm proteins from single cancer cells. *ChemPhysChem.* 2010; 11(14):3063-3069.
- 89- Bailey RC, Kwong GA, Radu CG, Witte ON, Heath JR. DNA-Encoded Antibody Libraries: A Unified Platform for Multiplexed Cell Sorting and Detection of Genes and Proteins. *Journal of the American Chemical Society* 2007; 129(7):1959–1967.

- 90- Niemeyer CM. Semisynthetic DNA-protein conjugates for biosensing and nanofabrication. *Angew Chem Int Ed Engl.* 2010; 49(7):1200-1216.
- 91- Niemeyer CM. The developments of semisynthetic DNA-protein conjugates. *Trends Biotechnol.* 2002; 20(9):395-401.
- 92- Janeway CA Jr, Travers P, Walport M, *et al.* *Immunobiology: The Immune System in Health and Disease.* 5th edition. New York: Garland Science; 2001. The structure of a typical antibody molecule.
- 93- Goode J, Dillon G, Millner PA. The development and optimisation of nanobody based electrochemical immunosensors for IgG Sensors and Actuators. *B Chemical.* 2016; 234:478-484.
- 94- Desmyter A, Spinelli S, Roussel A, Cambillau C. Camelid nanobodies: killing two birds with one stone, *Current Opinion in Structural Biology.* 2015; 32:1-8.
- 95- De Marco A. Biotechnological applications of recombinant single-domain antibody fragments. *Microbial Cell Factories.* 2011; 10:44.
- 96- Aliprandi M, Sparacio E, Pivetta F, Ossolengo G, Maestro R, de Marco A. The Availability of a Recombinant Anti-SNAP Antibody in VHH Format Amplifies the Application Flexibility of SNAP-Tagged Proteins. *Journal of Biomedicine and Biotechnology.* 2010; Article ID 658954, 7 page.
- 97- Witt M, Walter JG, Stahl F. Aptamer Microarrays—Current Status and Future Prospects. *Microarrays.* 2015; 4:115-132.
- 98- Ni X, Castanares M, Mukherjee A, Lupold SE. Nucleic acid aptamers: clinical applications and promising new horizons. *Current Medicinal Chemistry.* 2011; 18(27):4206–4214.
- 99- Du W, Elemento O. Cancer systems biology: embracing complexity to develop better anticancer therapeutic strategies. *Oncogene.* 2015; 34:3215-3225.
- 100- De Palma M, Hanahan D. The biology of personalized cancer medicine: Facing individual complexities underlying hallmark capabilities. *Molecular Oncology.* 2012; 6(2):111-127.
- 101- Ganau M, *et al.* A DNA-based nano-immunoassay for the label-free detection of glial fibrillary acidic protein in multicell lysates. *Nanomed. Nanotech Biol Med.* 2015; 11:293–300.
- 102- Bosco A, Bano F, Parisse P, Casalis L, DeSimone A, Micheletti C. Hybridization in nanostructured DNA monolayers probed by AFM: theory versus □ experiment. *Nanoscale.* 2012; 4:1734.
- 103- Nkoua Ngavouka MD, Capaldo P, Ambrosetti E, Scoles G, Casalis L, Parisse P. Mismatch detection in DNA monolayers by Atomic Force Microscopy and Electrochemical Impedance Spectroscopy. *Beilstein J. Nanotechnol.* 2016; 7:220–227.
- 104- Centis F. *et al.* p185 HER2/neu epitope mapping with murine monoclonal antibodies. *Hybridoma* 1992; 11:267-276.
- 105- Tagliabue, E. *et al.* Selection of monoclonal antibodies which induce internalization and phosphorylation of p185HER2 and growth inhibition of cells with Her2/neu gene amplification. *Int. J. Cancer.* 1991; 47:933-937.
- 106- Kozlov IA, Melnyk PC, Stromborg KE, Chee MS, Barker DL, Zhao C, Efficient strategies for the conjugation of oligonucleotides to antibodies enabling highly sensitive protein detection, *Biopolymers* 2004; 73:621.
- 107- Bano F. *et al.* Toward multiprotein Nanoarrays using nanografting and DNA directed immobilization of proteins. *Nano Lett.* 2009; 9:2614–2618.

- 108- Liu M, Amro NA, Liu G. Nanografting for surface Physical Chemistry. *Annu. Rev. Phys. Chem.* 2008; 59:367-386.
- 109- Nkoua Ngavouka MD, Bosco, A, Casalis L, Parisse P. Determination of Average Internucleotide Distance in Variable Density ssDNA Nanobrushes in the Presence of Different Cations Species. *Macromolecules* 2014; 47:8748.
- 110- Prime K, Whitesides GM. Self-Assembled Organic Monolayers: Model Systems for Studying Adsorption of Proteins at Surfaces, *Science* 1991; 252:1164–1167.
- 111- Pale-Grosdemange C, Simon ES, Prime KL, Whitesides GM Formation of of self assembled monolayer by chemisorption of derivatives of oligo(ethylene glycol) of structure HS(CH<sub>2</sub>)<sub>11</sub>(OCH<sub>2</sub>CH<sub>2</sub>)<sub>m</sub>OH on gold. *J Am Chem Soc.* 1991; 113:12–20.
- 112- Solano I. *et al.* Spectroscopic Ellipsometry meets AFM nanolithography: about hydration of bio-inert oligo(ethylene glycol)-terminated Self Assembled Monolayers on gold. *Phys. Chem. Chem. Phys.* 2015; 17:28774.
- 113- Mirmomtaz E. *et al.* Quantitative study of the effect of coverage on the hybridization efficiency of surface-bound DNA nanostructures. *Nano Lett.* 2008; 8:4134–4139.
- 114- Copeland RA. *Enzymes: A Practical Introduction to Structure, Mechanism, and Data Analysis.* Copyright 2000 by Wiley-VCH
- 115- Zou T. *et al.* Nanobody-functionalized PEG-b-PCL polymersomes and their targeting study. *J. Biotechnol.* 2015; 214:147-155.
- 116- Monegal, A. *et al.* Immunological applications of single- domain llama recombinant antibodies isolated from a naive library. *Protein Eng. Des. Sel.* 2009; 22:273–280.
- 117- Djender, S. *et al.* Bacterial cytoplasm as an effective cell compartment for producing functional VHH-based affinity reagents and Camelidae IgG-like recombinant antibodies. *Microb. Cell Fact.* 2014; 13:140.
- 118- Soler MA, de Marco A, Fortuna S. Predicting the yields of engineered nanobodies by means of molecular dynamics simulations and docking. *Scientific Rep.* 2016; 6:34869.
- 119- Duffy MJ, McGowan PM, Harbeck N, Thomssen C, Schmitt M. uPA and PAI-1 as biomarkers in breast cancer: validated for clinical use in level-of-evidence-1 studies. *Breast Cancer Research.* 2014; 16(4):428.
- 120- Edwards D, Hoyer-Hansen G, Blasi F. *The Cancer Degradome: Proteases and Cancer Biology.* B.F. Sloane - Springer Science & Business Media. 2008. ISBN 978-0-387-69057-5
- 121- Bock LC, Griffin LC, Latham JA, Vermaas EH, Toole JJ. Selection of single-stranded DNA molecules that bind and inhibit human thrombin. *Nature* 1992; 355:564–566.
- 122- Padmanabhan K, Padmanabhan KP, Ferrara JD, Sadler JE, Tulinsky A. The structure of alpha-thrombin inhibited by a 15-mer single-stranded DNA aptamer. *J. Biol. Chem.* 1993; 268:17651–17654.
- 123- Padmanabhan K, Tulinsky A. An ambiguous structure of a DNA 15-mer thrombin complex. *Acta Cryst.* 1996; 52:D272–D282.
- 124- Charles PT, Stubbs VR, Soto CM, Martin BD, White BJ, Taitt CR. Reduction of non-specific protein adsorption using Poly(ethylene)glycol (PEG) modified polyacrylate hydrogels in immunoassays for staphylococcal enterotoxin b detection. *Sensors.* 2009; 9:645–655.
- 125- Arya SK, Solanki PR, Datta M, Malhotra BD. Recent advances in self-assembled monolayers based biomolecular electronic devices. *Biosens. Bioelectron.* 2009; 24:2810–2817.
- 126- Hulme EC, Trevethick A. Ligand binding assays at equilibrium: Validation and interpretation. *Br. J. Pharmacol.* 2010; 161:1219–1237.

- 127- Basic Theory of Affinity. Available online: [https://www.biocore.com/lifesciences/help/basic\\_theory\\_of\\_affinity/](https://www.biocore.com/lifesciences/help/basic_theory_of_affinity/) (Copyright © 2016 General Electric Company).
- 128- Perez EA, Press MF, Dueck AC. Immunohistochemistry and fluorescence in situ hybridization assessment of HER2 in clinical trials of adjuvant therapy for breast cancer. *Breast Cancer Res Treat.* 2013; 138:99–108.
- 129- Chen QQ, Chen XY, Jiang YY, Liu J. Identification of novel nuclear localization signal within the ErbB-2 protein. *Cell Res.* 2005; 15:504–510.
- 130- Wang SC, Lien HC, Xia W, *et al.* Binding at and transactivation of the COX-2 promoter by nuclear tyrosine kinase receptor ErbB-2. *Cancer Cell.* 2004; 6:251–61.
- 131- Kwon J. *et al.* RESOLFT nanoscopy with photoswitchable organic fluorophores. *Sci. Rep.* 2015; 5:17804.
- 132- Sagara Y, Mimori K, Yoshinaga K, Tanaka F, Nishida K, Ohno S, *et al.* Clinical significance of Caveolin-1, Caveolin-2 and HER2/neu mRNA expression in human breast cancer. *Br J Cancer.* 2004; 91:959–65.
- 133- Boing AN, *et al.* Single-step isolation of extracellular vesicles by size-exclusion chromatography. *Journal of Extracellular Vesicles.* 2014; 3:23430.
- 134- Andreu Z, Yáñez-Mó M. Tetraspanins in Extracellular Vesicle Formation and Function. *Frontiers in Immunology.* 2014; 5:442.
- 135- Bumgarner R. DNA microarrays: Types, Applications and their future. *Current protocols in molecular biology / edited by Frederick M Ausubel.* 2013.
- 136- Ryan D, Parviz BA, Linder V, Semetey V, Sia SK, Su J, Mrksich M, Whitesides GM. Patterning Multiple Aligned Self-Assembled Monolayers Using Light. *Langmuir.* 2004; 20:9080-9088
- 137- Lin H, Sun L, Crooks RM. Replication of a DNA Microarray. *J. Am. Chem. Soc.* 2005; 127:11210-11211.
- 138- Akbulut O, Yu AA, Stellacci F. Fabrication of biomolecular devices via supramolecular contact-based approaches. *Chem. Soc. Rev.* 2010; 39:30-37.
- 139- Yu AA, Savas TA, Scott Taylor G, Guiseppe-Elie A, Smith HI, Stellacci F. Supramolecular nanostamping: using DNA as movable type. *Nano Lett.* 2005; 5:1061-1064.
- 140- Markham NR, Zuker M. UNAFold: Software for nucleic acid folding and hybridization. In *Bioinformatics: Structure, Function and Applications—Methods in Molecular Biology*; Keith, J.M., Ed.; Humana Press: Totowa, NJ, USA, 2008; pp. 3–31.
- 141- Wikman M, Steffen AC, Gunneriusson E, Tolmachev V, Adams GP, Carlsson J, Ståhl S. Selection and characterization of HER2/neu-binding affibody ligands. *Protein Engineering, Design and Selection.* 2004; 17(5):455-462.
- 142- Zhang D. *et al.* Label-Free and high-sensitive detection of Salmonella using a Surface Plasmon Resonance DNA-based biosensor. *J. Biotech.* 2012; 160:123-128.
- 143- Pasternak A, Hernandez F, Rasmussen L, Vester B, Wengel J. Improved thrombin binding aptamer by incorporation of a single unlocked nucleic acid monomer. *Nucleic Acids Res.* 2011; 39:1155–1164.
- 144- Gupta O, Loos K, Kornjakov A, Spagnoli C, Cowman M, Ulman A. Facile route to ultraflat SAM-protected gold surfaces by “amphiphile splitting”. *Angew. Chem.* 2004; 43:520–523.
- 145- Xu S, Miller S, Laibinis PE, Liu G. Fabrication of nanometer scale patterns within self-assembled monolayers by nanografting. *Langmuir* 1999; 15:7244-7251.

146- Liu M, Amro NA, Chow CS, Liu GY. Production of Nanostructures of DNA on Surfaces. *Nano Lett.* 2002; 2:863–867.

-- Appendix references --

147- Maskos, U.; Southern, E. M. *Nucleic Acids Res.* 1992, 20, 1675–1678.

148- Hoheisel, J. D. *Nat. Rev. Genet.* 2006, 7, 200–210.

149- Harrison, A.; Binder, H.; Buhot, A.; Burden, C. J.; Carlon, E.; Gibas, C.; Gamble, L. J.; Halperin, A.; Hooyberghs, J.; Kreil, D. P.; Levicky, R.; Noble, P. A.; Ott, A.; Pettitt, B. M.; Tautz, D.; Pozhitkov, A. E. *Nucleic Acids Res.* 2013, 41, 2779–2796.

150- Knez, K.; Spasic, D.; Janssen, K. P. F.; Lammertyn, J. *Analyst* 2014, 139, 353.

151- Paynter, N. P.; Chasman, D. I.; Buring, J. E.; Shiffman, D.; Cook, N. R.; Ridker, P. M. *Ann. Intern. Med.* 2009, 150, 65–72.

152- Tuupanen, S.; Turunen, M.; Lehtonen, R.; Hallikas, O.; Vanharanta, S.; Kivioja, T.; Björklund, M.; Wei, G.; Yan, J.; Niittymäki, I.; Mecklin, J.-P.; Järvinen, H.; Ristimäki, A.; Di-Bernardo, M.; East, P.; Carvajal-Carmona, L.; Houlston, R. S.; Tomlinson, I.; Palin, K.; Ukkonen, E.; Karhu, A.; Taipale, J.; Aaltonen, L. A. *Nat. Genet.* 2009, 41, 885–890.

153- Zacharova, J.; Chiasson, J.-L.; Laakso, M.; STOP-NIDDM Study Group. *Diabetes* 2005, 54, 893–899.

154- Carr, D. F.; Alfirevic, A.; Pirmohamed, M. *Genes* 2014, 5, 430–443.

155- Lacy, E. R.; Cox, K. K.; Wilson, W. D.; Lee, M. *Nucleic Acids Res.* 2002, 30, 1834–1841

156- Han, W.-H.; Liao, J.-M.; Chen, K.-L.; Wu, S.-M.; Chiang, Y.-W.; Lo, S.-T.; Chen, C.-L.; Chiang, C.-M. *Anal. Chem.* 2010, 82, 2395–2400.

157- Shen, W.; Tian, Y.; Ran, T.; Gao, Z. *TrAC, Trends Anal. Chem.* 2015, 69, 1–13.

158- Kong, R.-M.; Zhang, X.-B.; Zhang, L.-L.; Huang, Y.; Lu, D.-Q.; Tan, W.; Shen, G. L.; Yu, R.-Q. *Anal. Chem.* 2011, 83, 14–17.

159- Milkani, E.; Morais, S.; Lambert, C. R.; Grant McGimpsey, W. *Biosens. Bioelectron.* 2010, 25, 1217–1220.

160- Knez, K.; Spasic, D.; Delpont, F.; Lammertyn, J. *Biosens. Bioelectron.* 2015, 67, 394–399.

161- Ji, H.; Yan, F.; Lei, J.; Ju, H. *Anal. Chem.* 2012, 84, 7166–7171.

162- Zhang, J.; Wu, X.; Chen, P.; Lin, N.; Chen, J.; Chen, G.; Fu, F. *Chem. Commun.* 2010, 46, 6986–6988.

163- Subramanian, H. K. K.; Chakraborty, B.; Sha, R.; Seeman, N. C. *Nano Lett.* 2011, 11, 910–913.

164- Zhang, Z.; Zeng, D.; Ma, H.; Feng, G.; Hu, J.; He, L.; Li, C.; Fan, C. *Small* 2010, 6, 1854–1858.

165- Dong, J.; Cui, X.; Deng, Y.; Tang, Z. *Biosens. Bioelectron.* 2012, 38, 258–263.

166- Hu, J.; Zhang, C.-y. *Anal. Chem.* 2010, 82, 8991–8997.

167- Chang, K.; Deng, S.; Chen, M. *Biosens. Bioelectron.* 2015, 66, 297–307.

168- Ianeselli, L.; Greci, G.; Callegari, C.; Tormen, M.; Casalis, L. *Biosens. Bioelectron.* 2014, 55, 1–6.

169- Crews, N.; Wittwer, C. T.; Montgomery, J.; Pryor, R.; Gale, B. *Anal. Chem.* 2009, 81, 2053–2058.

170- Knez, K.; Janssen, K. P. F.; Pollet, J.; Spasic, D.; Lammertyn, J. *Small* 2012, 8, 868–872.

171- Holford, T. R. J.; Davis, F.; Higson, S. P. J. *Biosens. Bioelectron.* 2012, 34, 12–24.

- 172- Kornyshev, A. A.; Qiao, R. J. *Phys. Chem. C* 2014, 118, 18285–18290.
- 173- Fedorov, M. V.; Kornyshev, A. A. *Chem. Rev.* 2014, 114, 2978–3036.
- 174- Guiducci, C.; Stagni, C.; Zuccheri, G.; Bogliolo, A.; Benini, L.; Samori, B.; Ricco, B. A Biosensor for Direct Detection of DNA Sequences Based on Capacitance Measurements. In *Proceeding of the 32nd European Solid-State Device Research Conference*, Sept 24–26, 2002; 2002; pp 479–482.
- 175- Carrara, S.; Cavallini, A.; Leblebici, Y.; DeMicheli, G.; Bhalla, V.; Valle, F.; Samori, B.; Benini, L.; Riccò, B.; Vikholm-Lundin, I. *Microelectron. J.* 2010, 41, 711–717
- 176- Peterson, A. W.; Wolf, L. K.; Georgiadis, R. M. *J. Am. Chem. Soc.* 2002, 124, 14601.
- 177- Rossetti, G.; Dans, P. D.; Gomez-Pinto, I.; Ivani, I.; Gonzalez, C.; Orozco, C. *Nucleic Acids Res.* 2015, 43, 4309–4321.
- 178- Wong, I. Y.; Melosh, N. A. *Biophys. J.* 2010, 98, 2954–2963
- 179- Nkoua Ngavouka, M. D. Conformational properties of variable density DNA nanobrushes. Ph.D. Thesis, University of Trieste, Trieste, Italy, 2015.